Charles University in Prague

Faculty of Mathematics and Physics

DOCTORAL THESIS

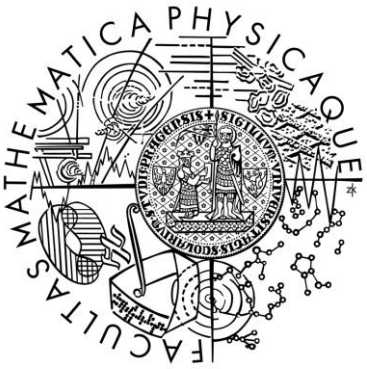

Jitka Stráská

Physical properties of ultrafine-grained magnesium based alloys prepared by various severe plastic deformation techniques

Department of Physics of Materials

Supervisor of the doctoral thesis: Doc. RNDr. Miloš Janeček, CSc.

Study programme: Physics of Condensed Matter and Materials Research
Specialization: Materials Research

Prague 2014

I would like to express my appreciation above all to my supervisor Assoc. Prof. Miloš Janeček. My sincere thanks are also extended to my colleagues from the Department of Physics of Materials Prof. Pavel Lukáč and Mgr. Josef Stráský for their consultations and other colleagues - Assoc. Prof. Jakub Čížek, Prof. Hyoung S. Kim, Prof. Jenö Gubicza, Prof. Stéphane Godet and Dr. Montserrat Galceran Mestres. My gratitude also goes to my family that supported me during all my studies. Finally, I would like to thank GAUK for financial support under the research project number 530712/2012.

I declare that I carried out this doctoral thesis independently, and only with the cited sources, literature and other professional sources.

I understand that my work relates to the rights and obligations under the Act No. 121/2000 Coll., the Copyright Act, as amended, in particular the fact that the Charles University in Prague has the right to conclude a license agreement on the use of this work as a school work pursuant to Section 60 paragraph 1 of the Copyright Act.

In Prague date..... Signature

Název práce: Fyzikální vlastnosti jemnozrnných hořčíkových slitin připravených různými technologiemi

Autor: Jitka Stráská

Katedra / Ústav: Katedra fyziky materiálů

Vedoucí doktorské práce: Doc. RNDr. Miloš Janeček, CSc.

Abstrakt:

Tato disertační práce je zaměřena na komplexní studium ultra-jemnozrnné hořčíkové slitiny AZ31 připravené dvěma různými metodami intenzivní plastické deformace: extruzí následovanou protlačováním lomeným kanálem (EX-ECAP) a torzí za vysokého tlaku (HPT). V úvodní části práce jsou detailně rozebrány různé metody intenzivní plastické deformace. V navazující části jsou shrnuty výsledky experimentů. Použitím širokého spektra experimentálních technik byla charakterizována především mikrostruktura, mechanické vlastnosti a struktura mřížových poruch materiálu. Byla zkoumána i strukturní stabilita ultra-jemnozrnné mikrostruktury za zvýšených teplot a za použití rovnic pro růst zrn a Arrheniovy rovnice byly spočteny aktivační energie pro růst zrn pro různé teplotní obory. Měřením hustoty dislokací byl nalezen teplotní interval zotavování a následného růstu zrn. Výsledky měření velikosti růstu zrn byly navíc použity pro ověření Hall-Petchovy rovnice. V poslední části práce je diskutována efektivita dvou zkoumaných metod intenzivní plastické deformace především pro zjemnění zrna. HPT se ukázala jako efektivnější metoda pro zjemnění zrna než EX-ECAP. Zmenšování velikosti zrna bylo navíc doprovázeno vyšší hustotou dislokací a větší mikrotvrdostí.

Klíčová slova: Ultra-jemnozrnné materiály; slitiny hořčíku; metody intenzivní plastické deformace; ekvivalentní vložená deformace; vývoj mikrostruktury.

Title: Physical properties of ultrafine-grained magnesium based alloys prepared by various severe plastic deformation techniques

Author: Jitka Stráská

Department / Institute: Department of Physics of Materials

Supervisor of the doctoral thesis: Doc. RNDr. Miloš Janeček, CSc.

Abstract:

The objective of the doctoral thesis is the complex investigation of ultrafine-grained magnesium alloy AZ31 prepared by two different severe plastic deformation techniques, in particular the hot extrusion followed by equal-channel angular pressing (EX-ECAP) and high pressure torsion (HPT). These severe plastic deformation methods, and as well as many others, are described in detail in the introductory theoretical section. Experimental results are summarized in the following experimental part of the thesis. Mechanical properties, lattice defect structure and especially microstructure were investigated using various experimental techniques. Thermal stability of ultrafine-grained microstructure of AZ31 after EX-ECAP was investigated and the activation energies for grain growth in different temperature ranges were calculated using kinetic equation for grain growth and Arrhenius equation. Results from the dislocation density measurements proved temperature ranges of the recovery and the following grain growth. Results from the grain size measurements verified the validity of well-known Hall-Petch equation. The efficiency of two investigated severe plastic deformation methods is also discussed in detail. HPT proved to be more effective method of grain refinement of AZ31 alloy resulting in significantly higher values of microhardness and dislocation densities.

Keywords: Ultrafine-grained (UFG) materials; magnesium alloys; severe plastic deformation (SPD) techniques; equivalent imposed strain; microstructure evolution.

Content

1 Introduction

1.1 Magnesium and its alloys

Magnesium is the sixth most abundant element in the earth´s crust, representing 2.7% of the earth´s crust [1]. Although magnesium is not found in its elemental form, magnesium compounds can be found worldwide. The most common compounds are magnesite, dolomite, carnallite and also sea water [2]. Magnesium is the third most abundant dissolved mineral in the seawater (1.1 kg/m^3).

Magnesium is also the lightest of all structural metals. It has a density of 1.74 g/cm^3, which is approximately one-fourth of the density of steel and two-thirds of that of aluminium [3–5]. Because of its low density and high specific mechanical properties, magnesium-based materials are widely employed by companies for weight-critical applications [6]. Other advantages of magnesium are good castability (suitable for high pressure die-casting) and good weldability under controlled atmosphere [4]. Limitations for a wider use of magnesium are caused by some disadvantages, e.g. low elastic modulus, limited strength and creep resistance at elevated temperatures and high chemical reactivity [4].

The first commercial production of magnesium commenced in the middle of the 19th century. Consequently, the first magnesium alloys were developed. Magnesium alloys were significantly used during the Second World War for aircraft components. However, there was no continuous development as in the case of aluminium alloys. The number of aluminium alloys is therefore much higher than the number of magnesium alloys. Due to the environmental policy and the rising fuel costs, the low density of magnesium alloys was attractive enough to re-focus on magnesium alloys as a constructional material. Some of the magnesium alloys are also biocompatible and applicable in medicine, e.g. temporary screws, wire fixation or biodegradable stents [7].

The addition of alloying elements in pure magnesium helps to prove its properties. Magnesium is chemically active metal and can react with other metallic alloying elements to form intermetallic compounds. The intermetallic phases can be observed in most of the magnesium alloys. These phases influence the microstructure and the mechanical properties of the alloy. Precipitation hardening and also the solid solution strengthening are the fundamental mechanisms to enhance the mechanical properties of the magnesium-based materials.

Aluminium, zinc, manganese, zirconium and rare earth metals (RE) are the most commonly used alloying elements in magnesium. Addition of aluminium results in the enhancement of strength and hardness. Zinc is usually used in

conjunction with aluminium to increase the strength without reducing ductility [6]. The increase in strength to comparable level is not achievable if only aluminium content is increased [8]. The addition of manganese, which is usually incorporated with other alloying elements like aluminium, enhances the saltwater corrosion resistance of Mg-Al and Mg-Al-Zn alloys. Zirconium is very useful for microstructure stabilization in fine-grained magnesium. However, it cannot be used with aluminium and manganese because of the formation of stable compounds with these alloying elements. Rare earth metals are used in high-tech magnesium alloys due to their high costs. Their addition causes the increase of high temperature strength, creep resistance and corrosion resistance [2].

The slip mechanism is the most frequent mode of plastic deformation. It occurs by mutual slipping of crystal planes following well-defined rules of crystallography, i.e. plastic deformation most likely occurs in the densest crystalline planes and, within these planes, in the directions with the largest atom density. The combination of slip planes and slip directions forms slip systems. The collective motion of large amount of dislocations on different slip systems produces a permanent shape change allowing the metal to accommodate imposed plastic strains [9].

Slip occurs when the shear stress acting in the slip direction on the slip plane reaches a certain critical value. Thus, the critical resolved shear stress (CRSS) is the measure of the shear stress, resolved along the slip plane and in the slip direction, which is required to activate dislocation glide. It was found that the value of the CRSS in a given material with the specified dislocation density and purity is constant [9].

Magnesium has hexagonal close packed (HCP) crystal lattice with parameters a = 0.320 nm, c = 0.520 nm and the axial ratio c/a = 1.624. The basal slip ({00.2} <11.0> system) is the easiest and dominant deformation mode in pure magnesium. Other important slip systems are non-basal systems: prismatic {10.0} <11.0>, pyramidal type I {10.1} <11.0> and pyramidal type II {11.2} <11.3> (see Fig. 1.1.). The only basal slip does not offer five independent slip systems which are required for uniform deformation according to von-Mises criterion [10]. Thus, the non-basal slip or deformation twinning provides the additional independent deformation mode.

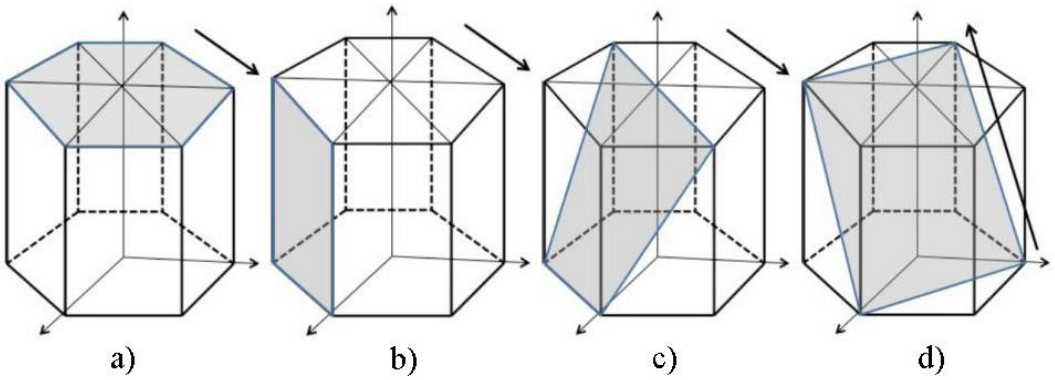

Figure 1.1: Slip systems in magnesium and its alloys: a) basal, b) prismatic, c) pyramidal type I, d) pyramidal type II. The arrows indicate the slip direction [11].

At elevated temperatures, the CRSS for prismatic and pyramidal slip systems reduce significantly and the twinning contribution becomes less crucial. Therefore, magnesium should be deformed at elevated temperatures to activate other slip systems in addition to the basal slip.

The ratio between the CRSS of the basal and non-basal slip can be also significantly changed by adding of alloying elements. This fact has been observed in AZ31 where the ratio between the CRSS for basal and prismatic slip varies in the range of 2-2.5 [12], while in pure Mg in the range 48-87 [13].

2 Theoretical background

2.1 Strengthening mechanisms in metallic materials

Macroscopic plastic deformation is caused by the movement of large numbers of dislocations. In order to enhance the strength or other mechanical properties of the metallic materials something which hinders the dislocation motion – obstacles – need to be introduced in the material [14]. The following four basic strengthening mechanisms in metals are known – work hardening (called also strain hardening), solid solution strengthening, dispersion or precipitation hardening and grain boundary strengthening.

Work hardening is caused by the dislocations which interact with each other and form stress fields in the lattice. Dislocation entanglements and dislocation jogs are usually created, too. All these obstacles can hinder dislocation motion and strengthen the material. Correlation between the dislocation density and yield strength could be expressed by the following relation [15]

$$\Delta\sigma_y = M\alpha Gb\sqrt{\rho_D}, \tag{2.1}$$

where M is the Taylor factor, α is a constant (usually equal to 0.1 - 0.5), G is the shear modulus, b is the Burgers vector and ρ_D is the dislocation density.

Solid solution strengthening is caused by the interaction of an alloying element with the dislocations which results in an increased glide resistance [9]. Alloying elements could form the interstitial or substitutional point defects depending on their atom sizes. The crystal structure of the solid solution remains the same as the structure of the basal metal, only the local stress fields are formed.

Dispersion hardening is caused by the particle – dislocation interactions. In this case, dislocations cannot cut or penetrate an incoherent particle and have to circumvent the particle by bowing out between the particles. This mechanism leads to dislocation loop creation and is referred to as the Orowan mechanism [9].

Precipitation hardening is caused by the phases with coherent or partially coherent phase boundaries. In this case, essentially all crystallographic planes and directions in the matrix continue into the precipitate with only a slight distortion. Dislocations may move through such a particle, cut it resulting in particle shear-off. However, the precipitate will exert forces on the dislocation which have to be overcome. This mechanism is referred to as Friedel mechanism [9].

Grain boundary strengthening is another type of strengthening mechanism, which is absolutely essential in the case of ultrafine-grained polycrystalline

materials. Grain boundaries cannot be overcome by dislocations because the Burgers vector has to be a translation vector of the crystal which – except for very special cases – does not hold for the next neighbour grain due to its different orientation. Hence, in the next neighbour crystal (grain) the slip directions are differently oriented and usually not parallel to each other. Thus, the dislocations pile up at the grain boundaries. These pile-up dislocations exert a back stress on subsequent dislocations which is opposite to the applied shear stress. The succeeding dislocations take up those positions which balance the applied shear stress and the back stress. Since the back stress increases with the increasing number of piled-up dislocations, the spacing between successive dislocations increases with the increasing distance from the pile-up tip [9].

The length of the pile-up in the grains, however, is geometrically limited. When we assume other geometrically preconditions and the activation of dislocation sources in neighbour grains due to the pile-ups in the original grain [16], we can derive the well-known relation between the strength and the grain size d of the polycrystalline material: Hall-Petch equation [17, 18]

$$\sigma_y = \sigma_0 + k_y d^{-\frac{1}{2}}, \tag{2.2}$$

where σ_y represents the yield stress of the material, σ_0 is the friction stress and k_y is a material constant. The Hall-Petch relation - the basis of the strengthening by grain refinement - is very important for the development of materials where the strength increase cannot be obtained by changing the chemical composition.

The Hall-Petch relation is applicable only in the limited range of grain sizes (approximately from 20 nm to tens of microns). In nanocrystalline materials with grain sizes usually smaller than 10 – 30 nm, a softening mechanism was observed [19]. This fact is known as the inverse Hall-Petch behaviour [20]. The Hall-Petch relationship is based on the dislocation activity in grains. However, nanocrystalline materials contain grains which are small enough to provide the dislocation activity at grain boundaries rather than in grains [21]. Hence, the larger fraction of atoms at grain boundaries causes the softening in the nanocrystalline materials with extremely small grains.

2.2 Ultrafine-grained materials produced by SPD methods

Ultrafine-grained (UFG) materials are characterized by small grain sizes in the range $0.1 - 1\ \mu m$ and, consequently, by a high fraction of intercrystalline boundaries. Consequently, grain boundaries in these materials play an important role and may significantly change the properties of UFG materials in comparison with their coarse-grained counterparts. UFG materials have also homogeneous and equiaxed microstructure with a majority of the grain boundaries having high angles of misorientation [22]. Some of the UFG materials contain also the non-equilibrium grain boundaries with high extrinsic dislocation and vacancy densities [23].

Severe plastic deformation (SPD) methods are very useful procedures how to prepare ultrafine-grained (UFG) materials. SPD procedures are used to impose very high strains in materials leading to exceptional grain refinement without any significant change in the overall dimensions of the samples. High hydrostatic pressures are applied during the SPD processes which introduce high densities of lattice defects (e.g. dislocations or vacancies) [24].

The formation of ultrafine-grained microstructure during SPD is not fully understood. Lapovok et al. believe that the microstructure is correlated with the recrystallization in-situ [25], the others interpret the microstructure as a cell dislocation structure [26, 27]. The sizes of dislocation cells decrease with increasing strain imposed by SPD. The dislocation cell structure is subsequently transformed into UFG structure. However, the satisfying consistent model describing UFG structure evolution is still not developed.

Two basic approaches for the fabrication of bulk UFG materials are used nowadays. They are designated as the 'bottom-up' and the 'top-down' approach [28].

The 'bottom-up' approach is based on the production of UFG powders and their consolidation. Ball milling [29], cryomilling [30], inert gas condensation [31] or the electrodeposition [32] are several examples of the techniques applying this 'bottom-up' approach. Production of UFG or nanocrystalline materials is the main advantage of this approach. Nevertheless, some degree of residual porosity in the material and potential contamination is the significant disadvantage of this approach.

The 'top-down' approach is in fact the inverse process to the 'bottom-up' approach. In this case, a coarse-grained bulk material is processed by some technique introducing high strains into the material resulting in the microstructure refinement. Almost no porosity and contamination is observed in materials processed by these techniques. However, the achieved grain sizes are usually larger than in materials prepared by the 'bottom-up' approach. Forging, rolling and extrusion are

the examples of the well-known conventional methods based on the 'top-down' approach which have been used in metallic materials for centuries. But these techniques are not sufficient enough to produce UFG materials. These procedures cannot introduce high imposed strain into the material without reduction of the workpiece cross-section. Hence, the above mentioned SPD methods are much better and suitable techniques for UFG bulk materials production.

The first SPD procedures were used in ancient China where the legendary Bai-Lian steel swords were produced [33]. Subsequently, this skill was spread to India and Syria where the ultra-high carbon Wootz steel and the world-famous Damascus steel was produced [34, 35].

The first real scientific approach to SPD processed was introduced by the Nobel prize winner P. W. Bridgman in the 1940s and 1950s [36]. Since that time, a lot of more or less useful SPD procedures were developed and investigated. The most frequently used techniques of SPD are: equal-channel angular pressing (ECAP) [37], high-pressure torsion (HPT) [38], accumulative roll-bonding (ARB) [39], friction stir processing (FSP) [40, 41], repetitive corrugation and straightening (RCS) [42, 43], multi-directional forging [44], twist extrusion [45] or cyclic-extrusion–compression (CEC) method [46, 47]. Some of these techniques will be described in detail in the following section.

2.2.1 Equal-channel angular pressing (ECAP)

The equal-channel angular pressing (ECAP), in Russia also known as equal-channel angular extrusion (ECAE), is one of the mostly developed and also commercially used SPD procedures. ECAP was invented by Segal et al. in 1970s and 1980s in the former Soviet Union [48, 49]. Since its invention ECAP became well-known and world-widely used technique. This SPD method was first successfully applied to produce UFG structure in a large variety of pure metals, e.g. UFG magnesium [50] , aluminium [51], copper [52] , nickel [53], titanium [54] or steels [55], and multi-phase or composite materials too [56]. Nowadays, ECAP is a commonly-used SPD method applicable in many branches of industry.

The main advantage of ECAP technique is the same cross-sectional dimensions of the specimens before and after pressing. This fact allows repetitive pressing and the accumulation of strain in the specimen. Furthermore, the ECAP is a quite simple process commonly used world-wide.

However, the ECAP method has also some constraints, e.g. specimen dimensions are limited. Usually, the billet´s length and diameter vary between 5 and 15 cm and 5 and 20 mm, respectively. In addition, the ends of processed billets

usually contain heterogeneous microstructure and must be discarded. Moreover, the material production costs by ECAP are not negligible. Some of the limitations, in particular the limited length of the material may be solved by another design of ECAP allowing continuous pressing – so called conform ECAP [57] whose principle will be described below. Despite all these disadvantages ECAP is very popular and mostly used technique of SPD.

The ECAP die consists of two channels with the same cross-section. Generally, the ECAP die is characterized by two angles: Φ, which is formed by these two channels and the angle Ψ which indicates the outer arc of curvature at the intersection of the two channels. The conventional mostly used ECAP die with the angle Φ equal to 90° is shown schematically in Fig. 2.1 and the general ECAP die with the illustration of the both angles is shown in Fig. 2.2.

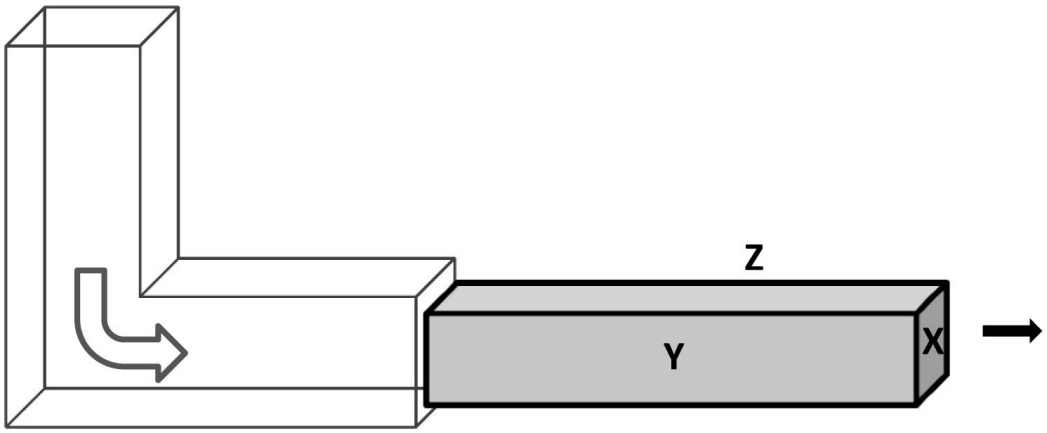

Figure 2.1: Schematic illustration of a conventional ECAP facility, *X* denotes the transverse plane, *Y* flow plane and *Z* the longitudinal plane.

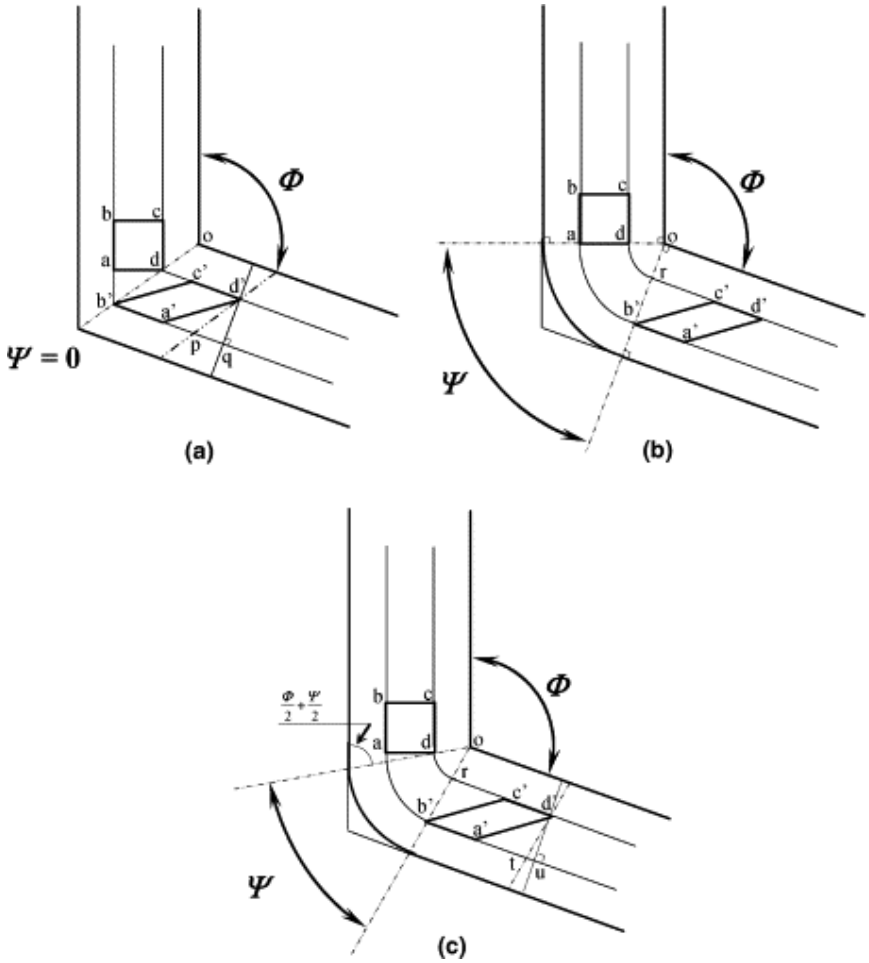

Figure 2.2: The scheme of pressing of the rectangular sample with the square cross-section through the ECAP die a) with Ψ = 0 and b) Ψ ≠ 0 [58].

The specimen pressed through the ECAP die is deformed by a simple shear in the intersection point of the channels and the imposed strain after *N* passes could be expressed [58]

$$\epsilon_N = \frac{N}{\sqrt{3}}\left[2cotg\left(\frac{\Phi}{2}+\frac{\Psi}{2}\right)+\Psi cosec\left(\frac{\Phi}{2}+\frac{\Psi}{2}\right)\right]. \qquad (2.3)$$

The equivalent strain imposed in the material during ECAP depends on both angles Φ and Ψ. However, the angle Ψ plays only a minor role in determining the strain imposed on the sample in comparison with the angle Φ [59]. The equivalent strain ε after one pass in the commonly used conventional ECAP die with Φ = 90° is close to 1 (100 %), cf. Fig. 2.3.

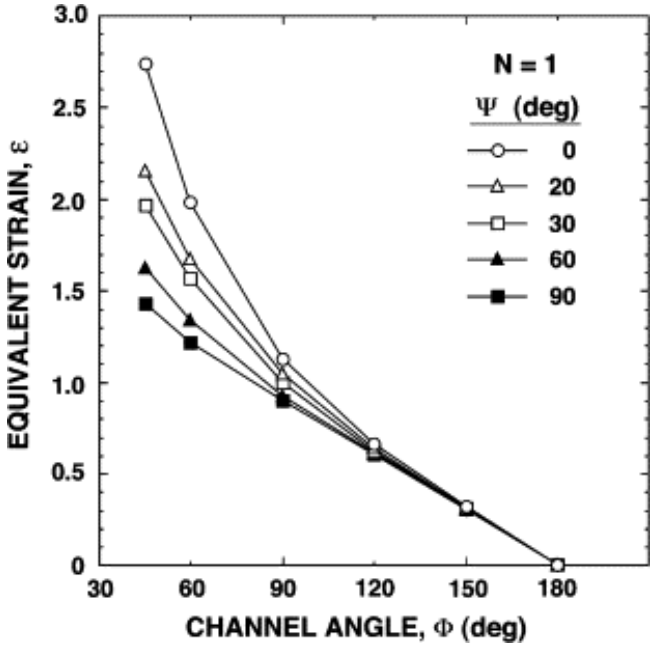

Figure 2.3: The equivalent strain ε after one pass of ECAP as a function of the angles Φ and Ψ [60].

The same cross-section of the entrance and exit channels allows repetitive pressing of the specimen which leads to the accumulation of the equivalent imposed strain and the production of UFG materials. On the other hand, the higher number of ECAP passes could cause cracking or other material defects. Thus, all pressing parameters (number of passes, deformation temperature and speed, applied pressure etc.) have to be optimized to achieve best results.

The most common ECAP die design consists of channels with the square cross-section. This form allows various specimen rotations between the individual ECAP passes which are known as routes [61]. Pressing through different routes activates different slip systems in the consecutive passes [62] and leads to different microstructures. Four different processing routes, schematically shown in Fig. 2.4 are commonly used [63]. In route *A* the specimen is pressed without rotation between the subsequent passes, in route B_A the specimen is rotated by 90° in alternate directions, while in route B_C the specimen is rotated by 90° in the same direction and in route *C* the specimen is rotated by 180° between the consecutive passes.

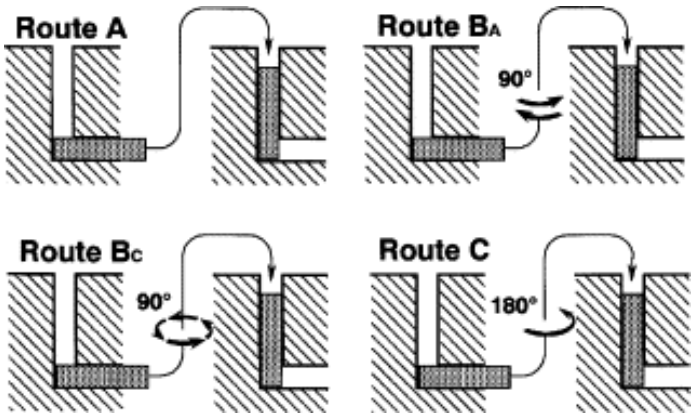

Figure 2.4: The four basic pressing routes in the ECAP die with square cross-sectional channels [63].

Different slip systems are activated during ECAP when various routes are employed (see Fig. 2.5). *X*, *Y* and *Z* planes are the orthogonal planes shown in Fig. 2.1 and the numbers 1-4 correspond to the number of ECAP passes [64]. In routes *C* and B_C, the shearing planes are the same in each pass while the shear direction is opposite. Thus, the equivalent strain is compensated after every even number of passes. On the other hand, the slip systems in routes *A* and B_A are different and the strain is accumulated during consecutive passes. However, it is not apparent which route is optimal for producing UFG materials. Recent investigations in this field are mostly (but not only) done in specimens processed by B_C route. Langdon claims that the route B_C leads to the most rapid development of the equiaxed microstructure on all three orthogonal planes of the specimen [37].

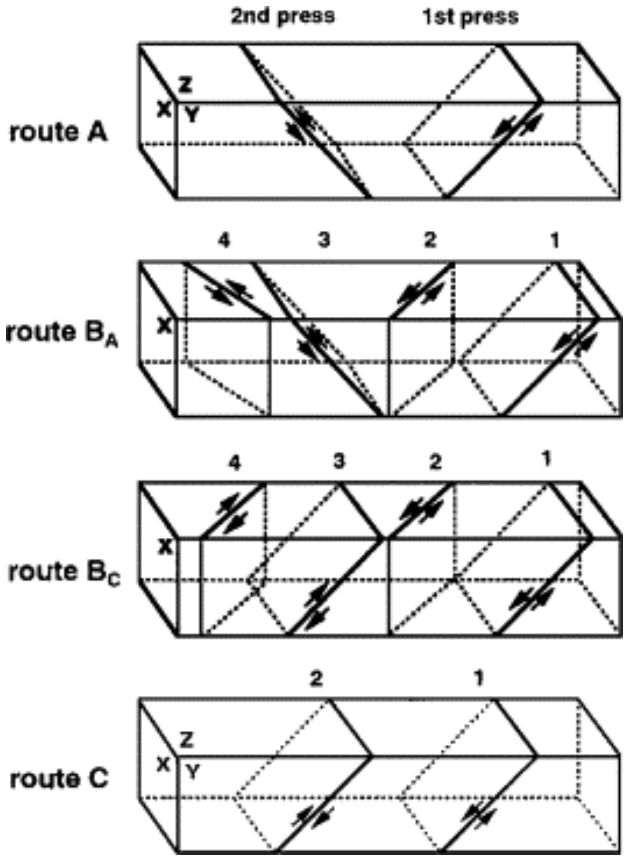

Figure 2.5: The slip systems viewed on the *X*, *Y* and *Z* planes for consecutive passes using processing routes *A*, B_A, B_C and *C* [65].

Several factors influence the workability and the microstructural characteristics of billets processed by ECAP. The first group of factors is associated directly with the ECAP die, namely the values of angles Φ and/or the outer arc of curvature Ψ between intersecting channels. The second group of factors are the experimental factors related to the processing regimes where some control may be exercised by the experimentalist including, e.g. the speed of pressing, the temperature of the pressing operation and the presence or absence of any back-pressure [59]. These two sets of experimental factors will be discussed in the following paragraphs.

The channel angle Φ is one of the most important ECAP parameter as it determines the strain imposed during pressing (see Eq. (2.3) and Fig. 2.3). The influence of the channel angle Φ was studied for example on pure aluminium using a series of ECAP dies with the different values of Φ (90° - 157.5) [66]. Several samples with the same calculated imposed strain were produced in different dies, whereas the number of passes increased with increasing value of channel angle. Nakashima et al. [66] showed that the microstructure becomes less regular and that the higher fraction of low angle grain boundaries is formed with increasing channel

angle Φ. These results demonstrate that, at least for pure aluminium, the total cumulative strain is not the important factor in determining the microstructure in ECAP but rather it is important to ensure that a very high strain is imposed on each separate pass. This means in practice that the ideal ECAP die needs to have a channel angle close to 90°. Moreover, it implies that similar microstructures cannot be attained with other techniques, as in conventional extrusion using multiple passes, where small incremental strains are imposed in each separate pass [59]. ECAP dies with the channel angle smaller than 90° are commonly not used because significantly higher pressure is necessary to produce specimens without cracks.

The pressing temperature is another crucial parameter in ECAP influencing significantly the microstructure of the processed materials. Extensive investigations were made in this regard and two important trends were observed (e.g. [67] and [68]). The first one is an increase in the equilibrium grain size with increasing pressing temperature as shown in Fig. 2.6. The second significant trend is a decrease of high-angle grain boundary fraction and crack density with increasing deformation temperature. It means that the pressing temperature needs to be optimized to achieve UFG material with high fraction of high-angle grain boundaries (HAGBs) and with low crack density.

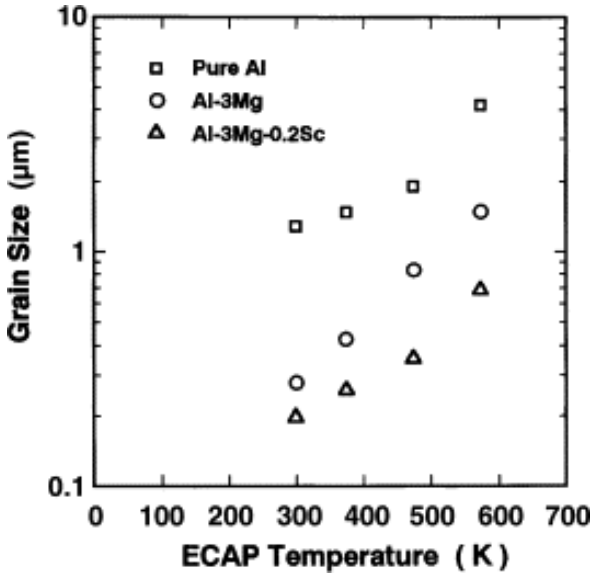

Figure 2.6: The average grain size after ECAP as a function of the pressing temperature for pure aluminium and two different aluminium alloys [67].

The pressing speed is another significant parameter from the second group of factors. The influence of pressing speed (in the range 10^{-2} – 10 mm.s^{-1}) on microstructure was investigated for example by Berbon et al. [69]. The authors did not observe any significant influence on the average grain sizes or yield stress of the processed material (see Fig. 2.7). However, they demonstrated that more equilibrated

microstructure is produced by lower pressing speeds. On the other hand, lower pressing speed leads to the extended exposure time of the material at the processing temperature, which may cause recrystallization or grain growth at higher pressing temperatures.

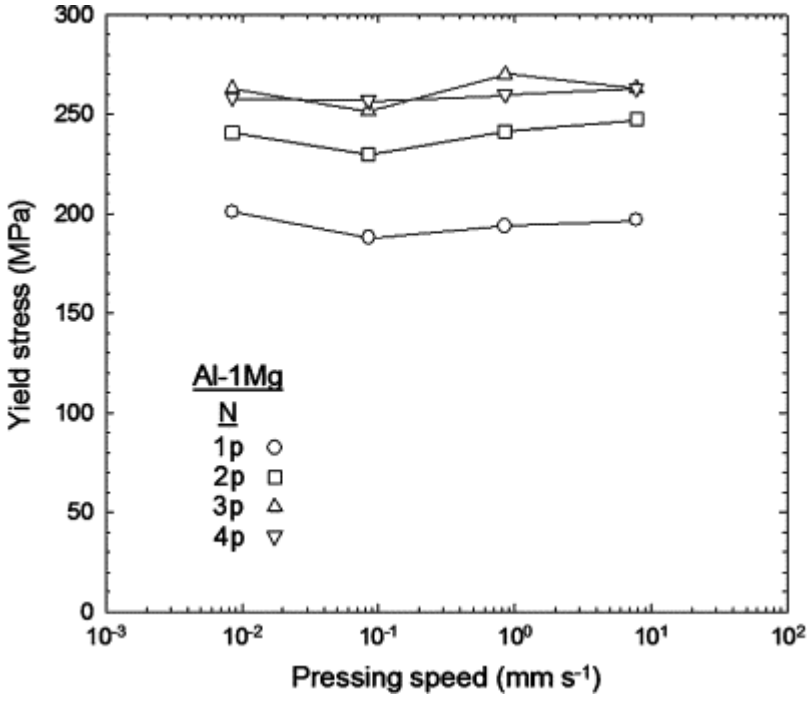

Figure 2.7: Variation of the yield stress with the pressing speed for an Al–1%Mg alloy after ECAP through 1, 2, 3 and 4 passes (room temperature, strain rate of 1.0×10^{-1} s^{-1}) [69].

The last important parameter from this group is the back-pressure. In the back-pressure ECAP die, the pressure is applied in the exit channel in the opposite direction to the movement of the pressed billet, see Fig. 2.8. The use of back-pressure leads to a significant improvement in the workability of processed billets which allows to increase the number of passes and to reduce crack formation [70]. Xu et al. also showed that the use of back-pressure reduces the average grain size of the commercial AZ31 alloy [71].

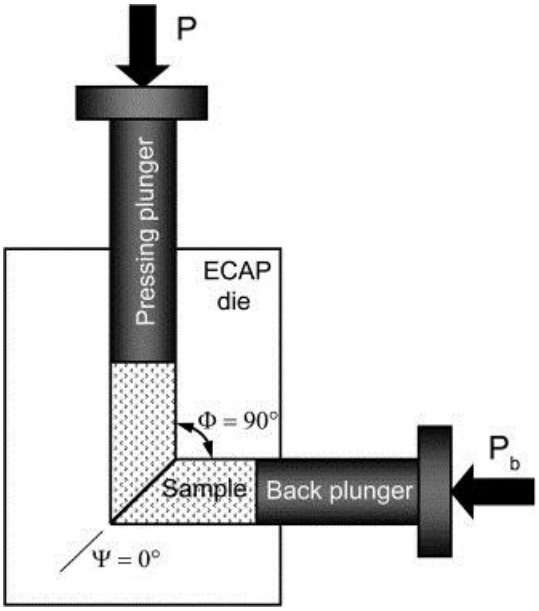

Figure 2.8: Schematic illustration of the experimental facility showing a back pressure, P_b, in a conventional ECAP die [72].

As mentioned above, the conventional ECAP has some limitations, e.g. specimen dimensions. Especially restricted sample length is not suitable for practical applications. A discontinuous process of repetitive sequence of equal-channel angular pressing, removing and reinserting of a short samples to achieve higher imposed strain is not useful for industrial production of ECAPed materials. Conform ECAP provides a solution – the process becomes continuous. The principle of this method is schematically shown in Fig. 2.9. The device consists of a rotating inner shaft and an outer stationary die. The specimen enters the die, rotates with the shaft and moves into a groove having a rectangular cross-section. When the material is pressed from the internal to exit channel it is turned through an angle Φ. In this case, when the channel angle Φ is equal to 90° the equivalent strain ε is equal to ~ 1 after one pass of conform ECAP [73]. Nowadays, specimens of the length of meters from different materials are commonly produced by ECAP-conform [57, 73].

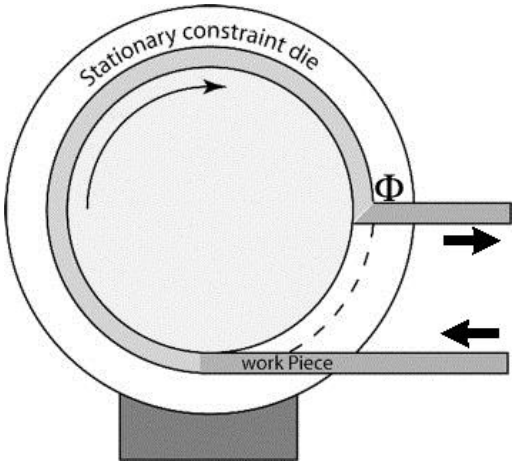

Figure 2.9: Schematic illustration of conform ECAP die [59].

2.2.2 High pressure torsion (HPT)

High pressure torsion (HPT) is another well-known severe plastic deformation technique. In this method, the mechanical properties of a material are improved by a high pressure and concurrent torsional straining [38]. HPT was for the first time applied to metals in Russia in 1980s [74]. The experimental setup of HPT is schematically illustrated in Fig. 2.10.

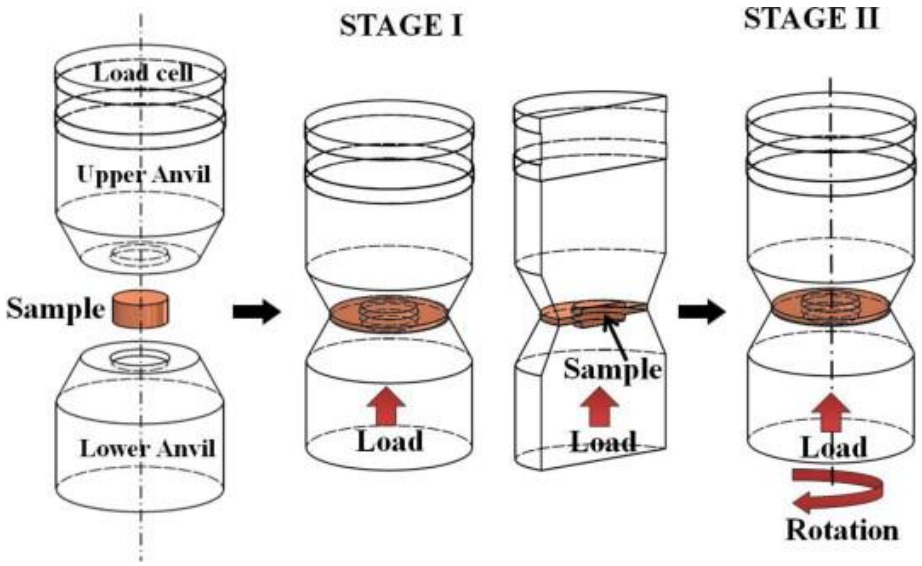

Figure 2.10: Schematic of the HPT device showing set-up, compression stage (stage I), and compression-torsion stage (stage II) [75].

The typical size of the disk-shaped sample varies from 10 to 20 mm in diameter and about 1 mm in thickness. A disk sample is placed between two anvils where it is subjected to a compressive pressure of several GPa. Simultaneously, the lower anvil rotates and the torsional strain is imposed to the sample.

The total strain imposed by HPT in the sample can be calculated by different approaches. The first widely used approach (Hencky/Eichinger) can be expressed by logarithmic relation [76]

$$\epsilon = ln\left(\frac{2\pi N r h_0}{h^2}\right), \tag{2.4}$$

where N is the number of rotations, r represents the radius of the sample and h_0 and h its initial and final thickness, respectively. The second possible approach (von Mises) using a model of simple torsion could be expressed by the following linear relation [77]

$$\epsilon = \frac{\gamma}{\sqrt{3}} = \frac{r\theta}{\sqrt{3}h} = \frac{2\pi N r}{\sqrt{3}h}, \tag{2.5}$$

where γ is the shear strain and θ is the rotation angle.

However, the real strain generated in the workpiece during HPT may be different depending mainly on the die geometry and other factors. No unambiguous conclusion was adopted whether the Hencky or von Mises strain describes better the total strain imposed by HPT. Therefore, a local deformation analysis using the finite element method (FEM) should be carried out to investigate plastic deformation during HPT. Several papers [78–80] have analysed the plastic deformation during HPT using the FEM and reported a change in thickness of the specimen, elastic recovery, the effect of the friction coefficient, mean stress, torque etc. Lee et al. employed FEM analysis coupled with a constitutive model based on a dislocation cell evolution mechanism of plastic deformation in order to understand local deformation of a workpiece during HPT [77]. The calculated results are shown in Fig. 2.11.

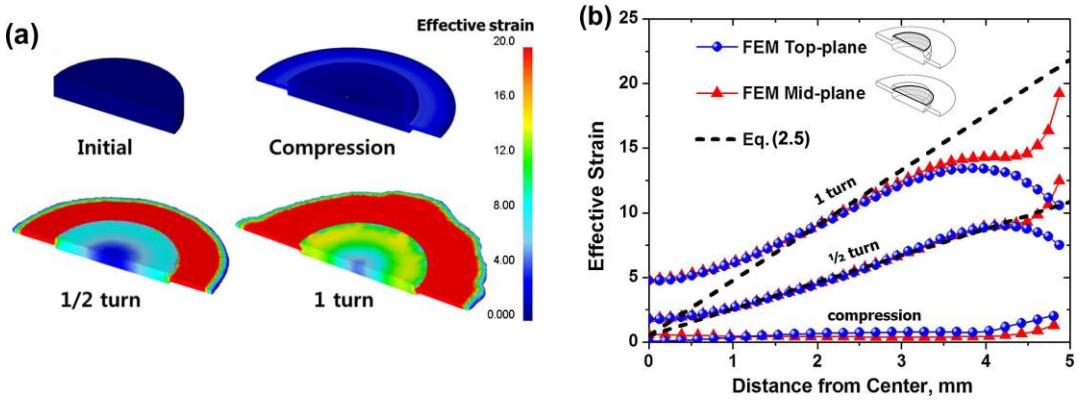

Figure 2.11: Finite element method (FEM) simulation of effective strain imposed by HPT: a) Deformed geometries at the initial stage, after compression, after 1/2 turn and after 1 turn with effective strain distributions; b) Path plots of the effective strain on the top plane and mid-plane after compression, 1/2 turn and 1 turn, comparing the theoretical von Mises strain (Eq. 2.5) and the results from FEM simulations [77].

The strain imposed on the material during HPT was shown to lead to an exceptional level of microstructural refinement, accompanied by a substantial improvement of room temperature strength. With the possibility of reaching average grain sizes around or smaller than 100 nm in a variety of materials [81–83], HPT surpasses the limits of grain refinement during ECAP. Also Iwahashi et al. showed that HPT is more effective method than ECAP in producing extremely small grain sizes [84].

An important disadvantage of HPT processing is that the imposed strain varies across the sample and the strain is zero at the disk centre. As a consequence, it is reasonable to anticipate that the microstructure refinement produced by HPT will be extremely inhomogeneous. This generally leads to a rather pronounced inhomogeneity in the microstructural refinement and the consequent changes in the mechanical properties of the material, especially if lower pressure is applied [85]. Nevertheless, the experimental data available to date suggest that there is a potential for achieving a gradual evolution into a reasonably homogeneous microstructure in many materials with increasing torsional strain.

In practice there are two distinct types of HPT processing as illustrated schematically in Fig. 2.12. These types are termed unconstrained and constrained HPT, respectively [86].

In the unconstrained HPT, the specimen is placed on the lower anvil and it is then subjected to an applied pressure and torsional straining as illustrated in

Fig. 2.12a. Under these conditions, the material is free to flow outwards under the applied pressure and only a minor back-pressure is introduced into the system due to the frictional forces acting between the sample and the anvil [38].

On the other hand, in the constrained HPT, as shown in Fig. 2.12b, there is a groove machined in the lower anvil cf. Fig. 2.12b and the disk is initially put in it. Due to this design by application of pressure there is no outward flow of material during the torsional straining. The true constrained HPT is in fact conducted in the presence of an effective back-pressure. However, it is generally difficult to achieve an idealized constrained condition and experiments are often conducted under a quasi-constrained condition as shown in Fig. 2.12c where there is at least some limited outward flow between the upper and lower anvils [38].

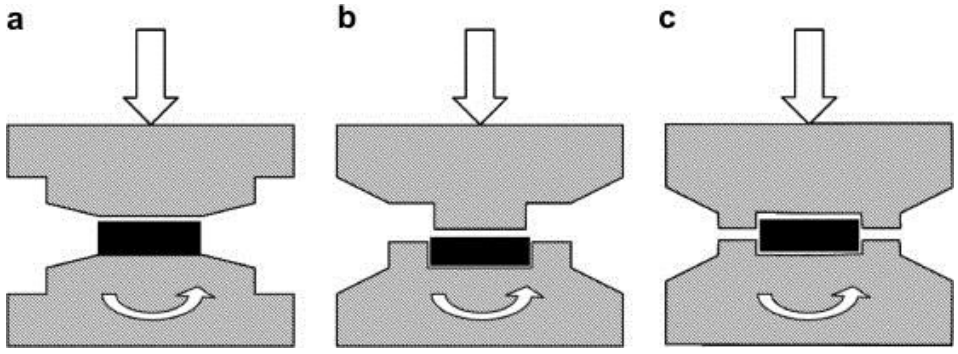

Figure 2.12: Schematic illustration of HPT for a) unconstrained and b) and c) constrained conditions [86].

The first results of microhardness variations throughout the whole surface an HPT disk were reported in high-purity Ni [85]. The averaged data, known as microhardness profiles, i.e. the variations of HV with the distance from the disk centre are plotted in Fig. 2.13. Fig. 2.13 (a) gives the variation of microhardness across two disks processed under different applied pressures – the value of microhardness increases with increasing applied pressure. Fig. 2.13 (b) shows the average microhardness measured in the central and peripheral parts of the disks – microhardness in the peripheral part of the sample increases very fast with increasing applied pressure.

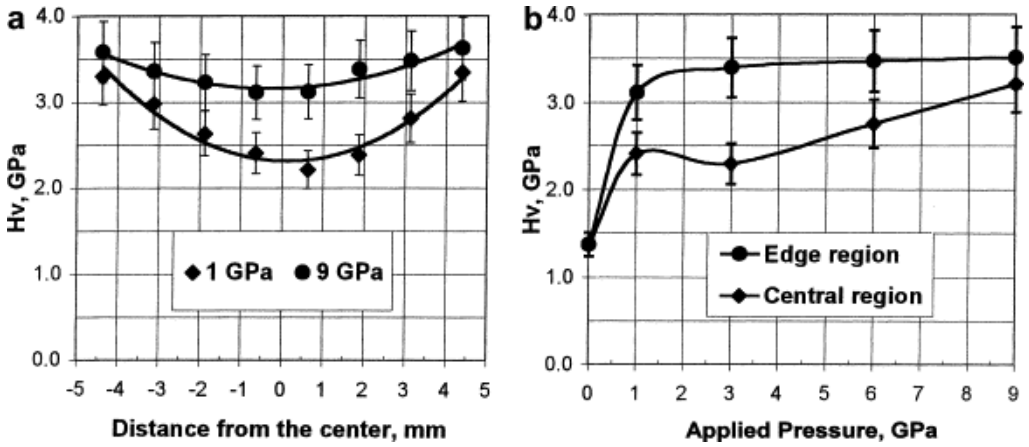

Figure 2.13: a) Microhardness profiles of Ni processed by HPT at two different applied pressures and b) the average microhardness at the central and edge regions as a function of the applied pressure (room temperature, 5 turns) [85].

Fig. 2.14 shows the typical microhardness variations across the diameters of disks at low total strains in HPT for materials with slow or fast rate of recovery [87]. HPT of materials with slower recovery rates tend to exhibit lower microhardness values in the centre of the disk. On the contrary, materials with high recovery rates have been shown to have lower microhardness near the periphery of the disk and not in its centre [38]. Zhilyaev and several other authors showed that the strain inhomogeneity is reduced by increasing number of HPT rotations [88–90]. On the other hand, this apparent disadvantage of inhomogeneity is also eliminated when ring samples are used [91].

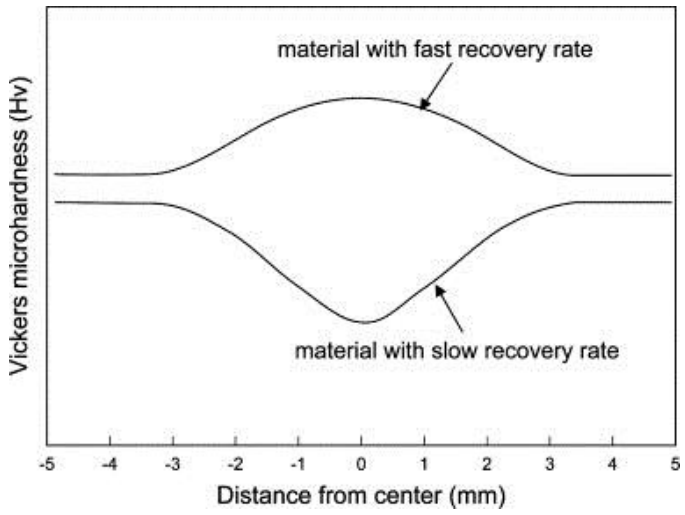

Figure 2.14: Schematic illustration of the variation of the Vickers microhardness across the disk at low total strains in HPT for materials having either slow or fast rates of recovery [87].

Nevertheless, HPT has another substantial limitation which is the small size of the processed specimens. Unlike ECAP, which can be relatively easily adapted for use with larger samples [92], the effort to scale up HPT has not yet been very successful. Because of this limitation, material achieved by this method is used mostly in modern micro-size specialized industrial branches, e.g. micro-electro-mechanical systems [38].

Some progress has been made, with the extension of the HPT to cylindrical samples, but it was found that such an experimental arrangement leads to strong microstructural inhomogeneities in the vertical sections of the cylinders [93]. Another variation of the method reported only recently is a hollow cone HPT which can process hollow cone-shaped samples used for projectiles, valves, nozzles, drill heads or many other engineering parts that require superior mechanical properties [94].

2.2.3 Accumulative roll-bonding (ARB)

Accumulative roll-bonding (ARB) is another technique for producing UFG materials. ARB was invented by a Japanese group of researchers in 1990s [39], and successfully applied, during the subsequent years, to a wide variety of materials including Al, Cu, Ni, IF steel and others [95]. The principle of this method is schematically illustrated in Fig. 2.15. In the first step, the strip of a material is rolled to 50 percent reduction of thickness. Subsequently, the strip is cut in two halves and one strip is placed on the top of the second one. Finally, these two strips of material are joined together by rolling. This cycle can be repeated again and again and the strain is accumulated in the material with almost no change in its dimensions. The equivalent plastic strain imposed by ARB can be expressed [39]

$$\epsilon = \left[\frac{2}{\sqrt{3}} ln(2)\right] N = 0.80N, \tag{2.6}$$

where N is the number of cycles.

In order to ensure sufficient bonding of the individual layers, degreasing and wire-brushing is necessary before the stacking of the sheets. The quality of the bonding also improves with increasing rolling temperature, which at the same time reduces the rolling force. But temperature cannot exceed the recrystallization temperature leading to grain coarsening. Nevertheless, ARB has already been successfully applied to many materials at room temperature [95].

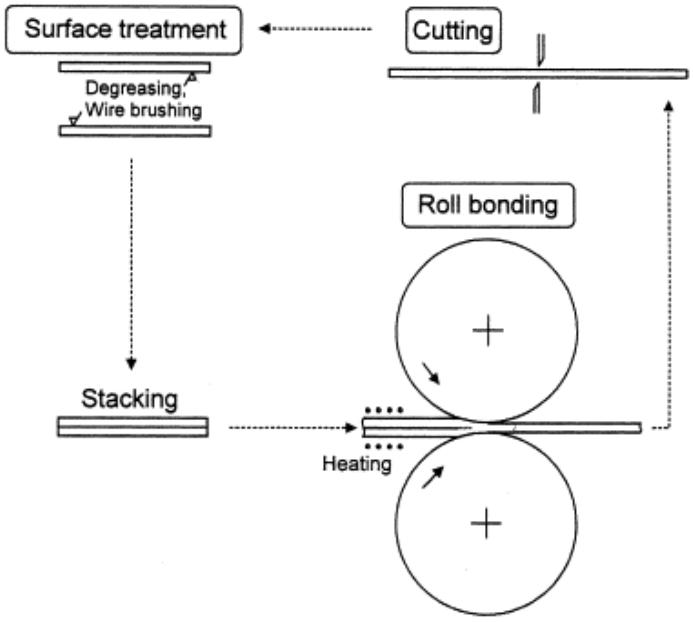

Figure 2.15: Schematic illustration of the accumulative roll-bonding (ARB) process [39].

The microstructure of the material produced by ARB is not equiaxed but comprises a high fraction of HAGBs. The limitation of this technique is the crack formation near sheet edges especially at higher cycles [96]. On the other hand, the advantage of ARB is that a conventional rolling mill can be used for material processing. Therefore, ARB is a suitable and useful technique for industrial production.

2.2.4 Twist Extrusion

Twist extrusion (TE), a promising SPD technique for grain refinement down to ultrafine/nanocrystalline microstructures, was introduced as an attempt to provide large plastic deformation conditions similar to those in HPT while allowing large workpiece dimensions for industrial applications [97].

Fig. 2.16 schematically illustrates the TE process. The die channel comprises three zones: inlet, twist, and outlet. The cross sections of the die and workpiece can be square, rectangular or round-corner rectangular. The twist channel is formed by sweeping the inlet profile along a helix line, resulting in a ‘twist angle’ between the inlet and outlet. A workpiece billet inserted into the inlet zone undergoes extrusion in the twist zone when forward and backward pressures are applied by a

punch via ‘dummy’ blocks. Ideally, the workpiece retains its initial geometry after the TE process, which allows repetition of the process and accumulation of large plastic deformation in the workpiece material [98].

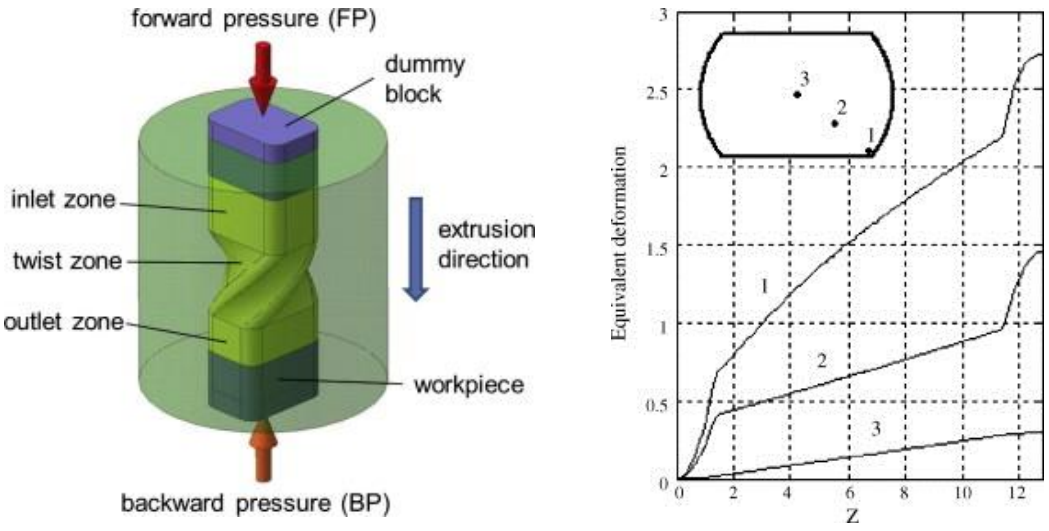

a) **b)**

Figure 2.16: a) Schematic of the twist extrusion process [97], b) equivalent strain versus coordinate along the extrusion axis (Z) for representative points of the specimen cross-section, where $\beta = 55°$, $\alpha = 70°$ [99].

2.2.5 Friction stir processing (FSP)

Friction stir processing (FSP), schematically shown in Fig. 2.17, uses the same techniques and equipment as friction stir welding. It selectively modifies the microstructure in specific areas providing locally improved mechanical properties [100, 101]. During FSP, a non-consumable tool comprising a shoulder and pin rubs against the work material and produces enormous frictional heat. The heat, combined with deformation by the stirring action of tool pin and pressure due to tool shoulder, produces a defect-free, dynamically recrystallized fine-grained microstructure.

The main parameter controlling the process is the rotation rate/traverse speed ratio. The temperatures reached in the material during FSP are relatively high – e.g. Darras et al. [102] processed commercial AZ31 magnesium alloy at the temperatures between 420 and 580 °C, which is 0.70 – 0.90 of the melting point of AZ31 magnesium alloy; therefore no melting has taken place during the process. Friction stir processing has been used in aluminium-based alloys for improving their mechanical properties [100, 101] and inducing superplasticity through grain refinement [103, 104].

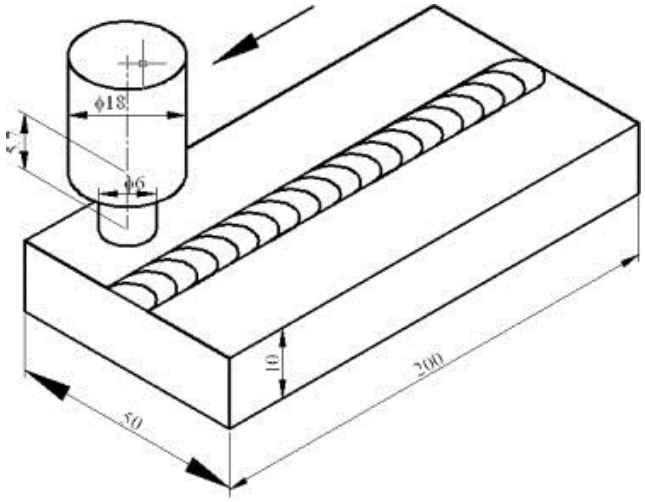

Figure 2.17: Friction stir processing set-up and cylindrical threaded profile tool [105].

The average grain sizes achieved by FSP are usually several microns [102, 106]. However, Chang et al. [107] combined FSP with rapid heat sink with liquid nitrogen and prepare UFG AZ31 alloy. With just one single FSP pass under effective cooling, the mean grain sizes of the obtained specimens were refined to an ultrafine scale (100–300 nm). Two passes of FSP led even to the average grain size of 85 nm in the AZ31 alloy [108].

2.2.6 Repetitive corrugation and straightening (RCS)

Repetitive corrugation and straightening (RCS), developed in the Los Alamos National Laboratory, is another useful SPD technique. RCS cannot only create bulk nanostructured materials free of contamination and porosity, but it can be also easily adapted to large-scale industrial production [43]. In the RCS process, a work-piece is repetitively bent and straightened without significantly changing the cross-section geometry of the work-piece, during which large plastic strains are imparted into the materials leading to the refinement of the microstructure [23]. The discontinuous and continuous process of RCS is schematically shown in Fig. 2.18 (a) and (b).

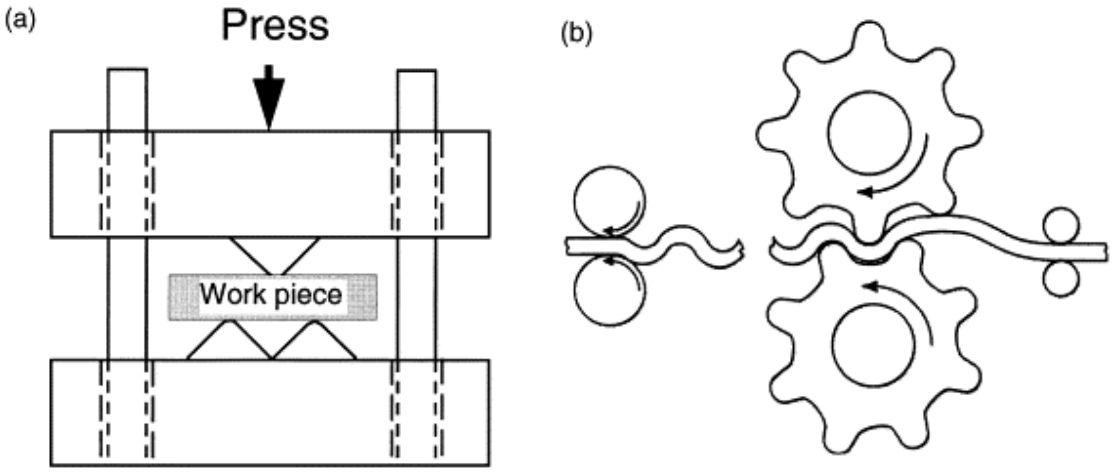

Figure 2.18: a) Die set up for discontinuous RCS process, b) set up for continuous RCS process that can be easily adapted to large-scale industrial production [23].

3 Aims of the thesis

In the previous two chapters, the motivation for the research in the field of magnesium-based ultrafine-grained (UFG) materials produced by severe plastic deformation (SPD) and their possible applications were discussed at a general level. An investigation of various properties (and especially the microstructure) of extremely deformed UFG magnesium materials is very difficult and requires modern experimental methods and special sample preparation techniques. Hence, the research focused on UFG magnesium alloys is limited and the numbers of papers about these materials are relatively low as compared to materials with cubic structure. The following are the specific aims of the present investigation, presented in a narrower scientific context.

The principal aim of the present work is to study the influence of the strain imposed by SPD on various characteristics of the processed commercial magnesium alloy AZ31. The alloy is prepared by two different SPD techniques: EX-ECAP (hot extrusion followed by equal-channel angular pressing) and HPT (high pressure torsion). The investigation could be divided into the following five branches:

- Calculation of the strain imposed in the material by two different SPD techniques.
- Investigation of microstructure using standard and enhanced microscopic techniques: scanning and transmission electron microscopy – SEM and TEM, electron backscatter diffraction - EBSD, and new sophisticated microscopic method - automated crystallographic orientation mapping in a TEM known as ACOM-TEM.
- Lattice defect structure investigated by positron annihilation spectroscopy (PAS) and X-ray diffraction (XRD) makes the research wider and more complex. Especially the dislocation density is very important parameter influencing mechanical and other properties.
- Mechanical properties, crucial problem for nearly all practical applications, are studied by microhardness measurements. Standard tensile tests cannot be applied in our case due to the limited number of processed specimens and their small sizes.
- Another part of investigation is focused on microstructure stability at elevated temperature. Microstructure stability could be extremely important for practical applications of components made of UFG commercial magnesium alloy AZ31.

4 Experimental procedures

4.1 Experimental material

The commercial magnesium alloy AZ31 with 3 wt. % of Al, 0.8 wt. % of Zn and 0.2 wt. % of Mn was used in this investigation. An equilibrium phase diagram of the binary system AlMg is shown in Fig. 4.1. The right part of the diagram is relevant for our investigation as the alloy AZ31 contains 96 percent of magnesium. Phase δ is a substitutional solid solution of aluminium in magnesium. Phase γ is the equilibrium phase of $Mg_{17}Al_{12}$. The part of the diagram labelled as γ + δ contains mechanical mixture of γ and δ phases.

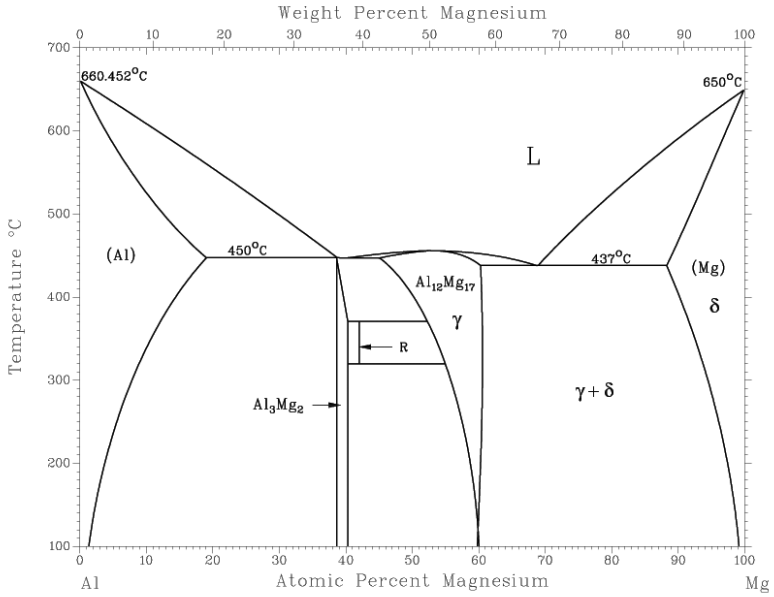

Figure 4.1: A phase diagram of a binary system AlMg [109].

Two most popular techniques of SPD were employed for material processing, namely the equal-channel angular pressing preceded by hot extrusion (EX-ECAP) and high pressure torsion (HPT).

Prior to ECAP, the specimens were extruded at 350 °C with an extrusion ratio of 22. The ECAP die was equipped with an ejector that allows ejecting the sample out of the die immediately after its pressing by a plunger from the feed-in channel to the exit channel. ECAP pressing was performed at 180 °C following route B_c, i.e. rotating the sample 90° between the individual passes, with the velocity of 50 mm/min and molybdenum disulphide grease was used as a lubricant. The angle Φ

between two intersecting channels and the corner angle Ψ were 90° and 0°, respectively. Both channels have a square cross section of 10 mm × 10 mm. A series of specimens after N=1, 2, 4, 8 and 12 passes was processed by ECAP. The as-extruded specimen was also included in the investigation as the reference material (marked N=0).

Prior to HPT, the material was homogenized at 390 °C for 12 hours. After homogenization the disk specimens of the diameter of 19 mm and the thickness of 1-2 mm were cut from the billet. These specimens were processed by quasi-constrained high pressure torsion (HPT) at room temperature for N = ¼, ½, 1, 5 and 15 rotations. The experimental setup is schematically illustrated in Fig. 2.10. In addition to samples subjected to various number N of HPT rotations, a sample which was pressed only between the anvils (STAGE I in Fig. 2.10) but not subjected to any HPT rotation (N = 0) was investigated as well.

The upper anvil is fixed with a load cell mounted on its top allowing measuring the hydrostatic pressure which is applied to the specimen during straining. The lower anvil with a sample placed in the groove is first lifted to its final position pressing the specimen to the symmetrical groove in the upper anvil. The upper and lower anvils of the die had depressions of 20 mm diameter and 0.25 mm thickness. The lateral wall was set at the angle of 5° to the vertical. In the compression stage, the speed of the top anvil was 0.1 mm/s until a pressure of 2.5 GPa was developed on the workpiece. In the torsion stage, the lower anvil was rotated at 0.1 rad/s up to a full turn with a constant pressure of 2.5 GPa. The friction between the die and the workpiece was set to satisfy the sticking condition, since the roughness of the die surface was high enough to prevent slippage between the workpiece and the die. All these procedures and preparations of the investigated material were also described in our paper [110].

4.2 Microhardness measurements

The basic principle of Vickers hardness test is to assess the employed material ability to resist plastic deformation. The diamond indenter in the form of a square-based pyramid with the top angle equal to 136° is loaded and applied to a flat surface of the sample.

An indentation left in the specimen after the test has a surface area A, which can be determined by the formula

$$A = \frac{d^2}{2sin(136°/2)}, \tag{4.1}$$

which can be approximated to give

$$A \approx \frac{d^2}{1.8544}, \tag{4.2}$$

where *d* is the average length of the diagonal left by the indenter.

The unit of Vickers hardness is represented by Vickers Pyramid Number (*HV*). The *HV* number is determined by the ratio

$$HV = \frac{F}{A} \approx \frac{1.8544F}{d^2}, \tag{4.3}$$

where *F* is the force applied to the indenter in kilograms-force and *A* is the surface area of the indentation in square millimetres. The principle of Vickers hardness measurements was also described in my diploma thesis [7].

4.3 Positron annihilation spectroscopy (PAS)

Positron annihilation spectroscopy (PAS) is a non-destructive spectroscopy method to study the defect density in solid materials. The PAS method is based on the fact that a positron which meets an electron annihilates. Gamma photons are emitted as a result of the positron-electron annihilation in the investigated material and are detected by the PAS detector. If the positron moves in the area of high electron density, the probability to meet an electron is high and its lifetime is short. The probability *N(t)* that a positron is still alive at a given time *t* could be expressed

$$N(t) = e^{-\lambda t}, \tag{4.4}$$

where λ is a positron annihilation rate and *N(0)* = 1. Free positron lifetime τ is defined as

$$\tau = \frac{1}{\lambda}. \tag{4.5}$$

Positron lifetime spectrum is defined as

$$-\frac{N(t)}{dt} = \lambda e^{-\lambda t}. \tag{4.6}$$

Positron lifetime spectrum is measured in a positron-lifetime spectrometer. The spectrometer consists of a radioactive source and a start and a stop detector. Positron is emitted by the source and propagates in the sample. In a defect free lattice, positron is delocalized and may be described by a wave function. If some lattice defect exists in the solid, it behaves like a potential well. In this case the wave function is localized in the vicinity of the defect, the positron is trapped there and its lifetime is therefore longer. As a consequence, positron lifetime correlates with the density of individual lattice defects [7].

In order to attain uniquely the determined free positron lifetimes the source of positrons has to be weak and the detector dead time very short. A $^{22}Na_2CO_3$ positron source (~ 1.5 MBq) deposited on a 2 μm thick mylar foil was used in positron lifetime measurements at the Department of Low Temperature Physics of the Charles University in Prague. The source was always sandwiched between two identical samples of the studied alloy. The source contribution consists of two components with lifetimes of 368 ps (intensity 8 %) and 1.5 ns (intensity 1 %) which come from positrons annihilated in the source spot and in the covering Mylar foil, respectively. Positron lifetime measurements were carried out using a fast–fast spectrometer [111] with a time resolution of 150 ps (FWHM ^{22}Na). At least 10^7 positron annihilation events were accumulated in each positron lifetime spectrum which was subsequently decomposed into individual exponential components by a maximum likelihood procedure [112]. By decomposition of positron lifetime spectra, information about individual defect density in the investigated material may be obtained. The defects types may be determined from the lifetimes τ_i while the defect densities are proportional to PAS intensities I_i.

4.4 X-ray Diffraction (XRD)

The X-ray line profiles were measured by a high-resolution rotating anode diffractometer (Nonius, FR 591) using Cu $K\alpha_1$ radiation (λ = 0.15406 nm) at the Department of Materials Physics at Eötvös Loránd University in Budapest. Two-dimensional imaging plates detected the Debye–Scherrer diffraction rings. The line profiles were obtained as a function of the diffraction angle by integrating the two-dimensional intensity distribution along the rings at discrete angle values. The line profiles were evaluated by the convolutional multiple whole profile (CMWP) fitting analysis [113]. In this procedure, the diffraction pattern is fitted by the sum of a background spline and the convolution of the instrumental pattern and the theoretical line profiles related to the crystallite size, dislocations, and twin faults. Seventeen peaks of Mg were used in the fitting procedure. The theoretical profile functions used in this fitting procedure were calculated on the basis of a model of the

microstructure, where the crystallites have spherical shape and log-normal size distribution.

The area-weighted mean crystallite size ($\langle x \rangle_{area}$), the dislocation density (ρ_D), the dislocation arrangement parameter (M), and parameters q_1 and q_2 depending on the population of the different slip systems were determined by the line profile analysis. The area-weighted mean crystallite size was calculated from the median and the variance, m and σ, of the log-normal size distribution as $\langle x \rangle_{area} = m\, exp(2.5\sigma^2)$ [113]. The relative fractions of different dislocation slip systems were determined by comparing the theoretical dislocation contrast factors with the experimental values using the procedure described in [114].

In hexagonal materials there are eleven dislocation slip systems [115]. The dislocation contrast factor C_{hkl} characterizes the effect of a dislocation type on the broadening of X-ray peak with the indices *hkl*. For hexagonal polycrystalline materials the average contrast factors $\bar{C}_{hkl}$ can be written in the following form [116]

$$\bar{C}_{hkl} = \bar{C}_{hk0}(1 + q_1 z + q_2 z^2)\,, \tag{4.7}$$

where q_1 and q_2 are two parameters depending on the anisotropic elastic constants of the crystal and the type of dislocation slip system. The value $z = \frac{2}{3}\left(\frac{l}{ga}\right)^2$, where a is the lattice constant in the basal plane and g is the magnitude of the diffraction vector. $\bar{C}_{hk0}$ is the average dislocation contrast factor for reflections *hk0*. The theoretical values of $\bar{C}_{hk0}$, q_1 and q_2 for the eleven possible slip systems in the most common hexagonal materials have been calculated according to [116], and are listed also in [116].

Each of the eleven slip systems has different theoretical values of $\bar{C}_{hk0}$, q_1 and q_2 parameters, therefore the evaluation of the experimental values of q_1 and q_2 enables the determination of the prevailing dislocation slip systems in the specimen. The eleven dislocation slip systems can be classified into three groups based on their Burgers vectors: (<a> type), (<c> type) and (<c+a> type). There are 4, 2 and 5 slip systems in the <a>, <c> and <c+a> Burgers vector groups, respectively. A computer program was elaborated in order to determine the distribution of dislocations among the different slip systems from the measured values of q_1^m and q_2^m [115]. In this procedure those dislocation populations are determined which yield the same *hkl* dependence of line broadening as obtained from the experiment. In the case of dislocations the mean-square-strain, which determines the peak breadth, can be expressed as [117]

$$\langle \varepsilon_{g,L}^2 \rangle \cong \frac{\rho \bar{C}_{hkl} b^2}{4\pi} f(\eta), \tag{4.8}$$

where

$$\eta = \frac{1}{2} exp\left(-\frac{1}{4}\right) \frac{L}{R_e^*}, \tag{4.9}$$

and ρ, b and R_e^* are the density, the modulus of Burgers vector and the effective outer cut-off radius of dislocations, respectively. The function $f(\eta)$ is referred to as Wilkens function and given in [118]. Eq. (4.8) shows that the variation of line broadening with the orientation of diffraction vector is determined by $\bar{C}_{hkl}$. Setting the experimental value of $\bar{C}_{hkl} b^2$ equals to the theoretical value calculated by averaging for the eleven slip systems, the following equation is obtained

$$\begin{gathered} \bar{C}_{hk0}^m (1 + q_1^m z + q_2^m z^2) b_m^2 = \\ \sum_{i=1}^{11} f_i \bar{C}_{hk0}^i \left(1 + q_1^i z + q_2^i z^2\right) b_i^2, \end{gathered} \tag{4.10}$$

where letter m indicates the values obtained from the measured profile, i denotes the theoretical values calculated for the i^{th} slip system and f_i is the fraction of dislocations in the i^{th} slip system. The polynomials in the two sides of Eq. (4.10) give the same values, if the coefficients of the terms with the same degrees are equal. This condition yields the following equations

$$\begin{gathered} q_1^m = \frac{\sum_{i=1}^{11} f_i \bar{C}_{hk0}^i b_i^2 q_1^i}{\sum_{i=1}^{11} f_i \bar{C}_{hk0}^i b_i^2}, \\ q_2^m = \frac{\sum_{i=1}^{11} f_i \bar{C}_{hk0}^i b_i^2 q_2^i}{\sum_{i=1}^{11} f_i \bar{C}_{hk0}^i b_i^2}, \\ \sum_{i=1}^{11} f_i = 1. \end{gathered} \tag{4.11}$$

There is no equation for $\bar{C}_{hk0}^m$ since it is not an independent parameter in the evaluation of line profiles as $\bar{C}_{hk0}^m$ is multiplied with the dislocation density in Eq. (4.8). The eleven values of f_i cannot be determined from the three formulas in Eq. (4.11), therefore additional restrictions are made for f_i. It is assumed that in each Burgers vector group the non-zero fractions are equal. This assumption reduces the number of variables to three, which are denoted by f_a, f_c and f_{c+a}.

The computer program written for the evaluation of Burgers vector population in hexagonal materials (referred to as *Hexburger* [115]) first selects some slip systems from <*a*> dislocation group and for these slip systems the weights are

f_a. For other slip systems in this group the weights are zero. This procedure is also carried out for <c> and <$c+a$> Burgers vector groups where the non-zero weights are f_c and f_{c+a}, respectively.

Inserting the theoretical values of $\bar{C}^i_{hk0}$, b_i, q^i_1 and q^i_2 into Eq. (4.11), the values of f_a, f_c and f_{c+a} are determined. If these fractions have positive values the program stores them as one of the possible solutions. The number of the possible selections from the dislocation slip systems equals $(2^4-1)(2^2-1)(2^5-1) = 1395$. Finally, the positive solutions for the weights can be averaged for each slip system, leading to the fractions of the eleven dislocation types.

The fractions of the three Burgers vector groups, h_a, h_c and h_{c+a}, are obtained by the summation of the fractions of the related slip systems. It should be noted that the *Hexburger* software gives directly the solutions for h_a, h_c and h_{c+a} in a file for each selection of slip systems. Then, f_a, f_c and f_{c+a} can be determined by dividing h_a, h_c and h_{c+a} with the number of slip systems with non-zero weights in <a>, <c> and <$c+a$> Burgers vector groups, respectively. In practice, the line profile evaluation directly yields $\rho b^2 \bar{C}^m_{hk0}$, ${q_1}^m$ and ${q_2}^m$. In the CMWP fitting procedure a preliminary value for $b^2\bar{C}^m_{hk0}$ is assumed and the evaluation gives a first approximation for ρ, since its value depends on $b^2\bar{C}^m_{hk0}$. Then, the Burgers vector population should be determined by the above described method. It results in the determination of the precise value of $b^2\bar{C}^m_{hk0}$. Finally, this parameter is used for obtaining the exact value of the dislocation density.

4.5 Electron backscatter diffraction (EBSD)

Electron backscatter diffraction (EBSD) is a microstructural crystallographic technique for the determination of crystallographic orientation. Texture, grain size and distribution, the misorientation and shape of individual grains, the types of grain boundaries and many other microstructural features may be obtained from EBSD results.

The principle of the EBSD method is that the accelerated high energy electrons interact with the atomic lattice of the crystalline material and form so called Kikuchi lines on the screen. The measurement is done automatically with a defined step. The formation of Kikuchi lines is caused by inelastic electron scattering. The inelastically scattered electron wave length is slightly longer than the wave length of elastically scattered electrons and the inelastic scattered electron intensity decreases with increasing scattering angle. In certain crystal orientations some planes satisfy the Bragg condition (with diffraction angle θ) and the inelastically scattered electrons are Bragg diffracted. These electrons are called Kikuchi electrons. Kikuchi electrons

move along conical surfaces whose top angle is equal ($\pi - 2\theta$) and the axis of diffraction planes is the normal line. Two hyperbolas are formed by the intersection of the conical surfaces and a screen. The hyperbolas seem like straight lines in the central part of diffractogram and the distance between lines corresponds to the angle 2θ [7].

The scanning electron microscope (SEM) FEI Quanta 200 FX equipped with EDAX EBSD camera and OIM software was utilized for EBSD observations. A field emission gun (FEG) of a Schottky type was used as a source of electrons in the microscope. Beam voltage in the range from 500 V to 30 kV is applicable. The acceleration voltage employed was 10 kV.

The samples for EBSD investigation were first mechanically grinded on watered abrasive papers of grade 800, 1200, 2400 and 4000, respectively. Then the specimens were mechanically polished with diamond suspensions for water-sensitive materials of grade 3, 1 and ¼ μm, respectively. The final ion-polishing using a Gatan PIPS device was used to remove the surface layer influenced by polishing.

4.6 Transmission Electron Microscopy (TEM)

Transmission electron microscopy (TEM) is a technique that studies the local microstructure of the material using a beam of high energy electrons. The specimens for TEM have to be very thin (~ 100 nm depending on the acceleration voltage). An image is formed from the interaction of the electrons transmitted through the specimen and focused on a fluorescent screen or CCD camera.

The sample preparation consists of two steps - mechanical thinning and polishing. The type of polishing depends on the physical and chemical properties of the material.

In case of UFG AZ31 alloy, the specimens were first cut from the billet in plane *X* (perpendicular to the extrusion direction) into slices of the thickness of cca 1 mm. The slices were mechanically grinded from both sides to the thickness of 100 μm. The 3 mm diameter disks were cut out of the thin slices and dimpled from one side to the thickness cca 30 μm using the Gatan dimple grinder. This dimpling technique reduces electrolytic or ion polishing times and ensures that the ultra-thin area is done in the central part of the foil.

Ion polishing is used for materials which cannot be polished electrolytically. Ion polishing is a method for removing very fine quantities of the material. It uses an inert gas (argon) to generate a plasma stream that is emitted to the thinned area of the sample and removes the individual layers of the material. Acceleration energies vary

usually from 2 to 4 keV. Ion beam always enters the sample. The penetration depth depends on the angle between a direction of the ion beam and the sample surface. The optimum conditions found were following: the acceleration voltage of 4 kV, the angle of incidence of 4° and room temperature. In the final stage the acceleration voltage was reduced to 2 kV and the angle of incidence to 2°. The specimen preparation for TEM is finished when a small hole is formed in the foil and the surrounding area is thin enough to allow high energy electrons to pass through the specimen [7].

The microstructure observations were made with the TEM JEOL 2000FX at Charles University in Prague. The applied accelerated voltage was 200 kV.

4.7 ACOM-TEM

Automated crystallographic orientation mapping in a TEM (ACOM-TEM) is an effective technique for mapping phase and crystal orientation and an alternative to well-known EBSD attachment in scanning electron microscope (SEM) based on the Kikuchi lines. ACOM-TEM was first introduced by Schwarzer et al. [119] in 1994. This method of microstructural characterization represents a powerful tool especially for UFG or nano-grained materials. Its basic principle is similar to EBDS mapping - a selected area is scanned and the electron diffraction patterns are collected using an external CCD camera. Off-line, every diffraction pattern is compared to the pre-calculated template and the best match is selected. The main difference with respect to EBSD is that point diffraction patterns are analysed instead of Kikuchi lines. This type of ACOM-TEM device was developed in Grenoble by Dr. E. Rauch et al. [120, 121].

The experimental measurements were carried out using a TEM Philips CM200 equipped with a LaB_6 gun at 200 kV at Université Libre de Bruxelles in Belgium. For the data treatment, TSL OIM Analysis 5 was used.

5 Experimental results

5.1 Characterization of ECAPed AZ31 alloy

5.1.1 Microhardness

The microhardness of all samples was measured on all three reference planes (*X*, *Y* and *Z*, designated in Fig. 2.1). The indentor was applied minimally ten times in each test. The indentations were located in a central part of the sample in a line perpendicular to the specimen edge. The microhardness values were calculated from the indentation parameters using the software Lucia Hardness and the results are shown in Fig. 5.1.

In Fig. 5.1 we can see that the microhardness is markedly higher already after the first ECAP pass. The microhardness increases only slightly up to the fourth pass and then declines up to the twelfth pass. No statistically significant differences of microhardness in individual planes were found, only the microhardness of *Y* plane after 4 passes is slightly higher. These results were also published in our paper [110].

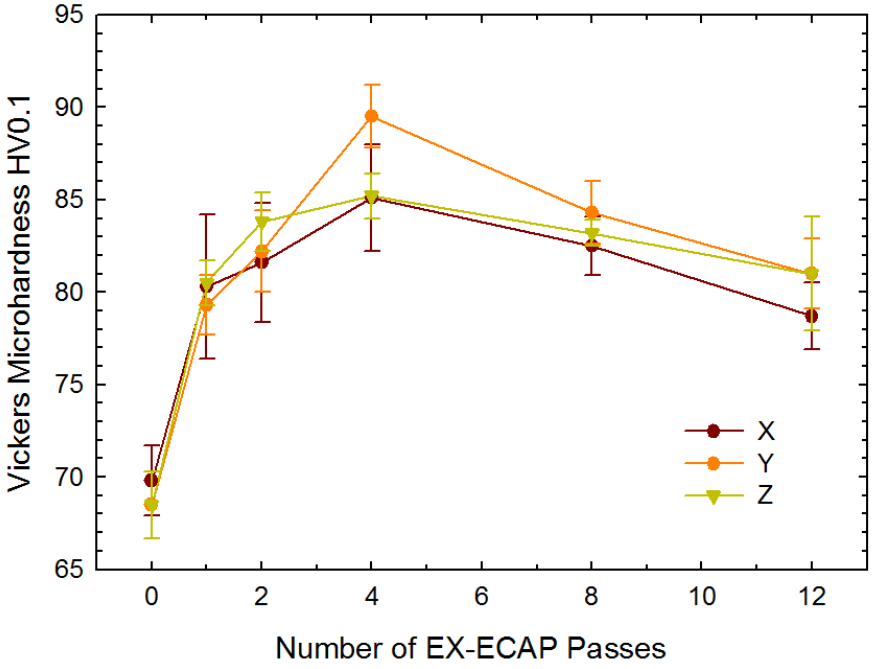

Figure 5.1: Microhardness of all three reference planes of the AZ31 specimens processed by extrusion and various numbers of ECAP passes.

5.1.2 Dislocation density studied by PAS

Positron lifetime spectra of all samples after hot extrusion and ECAP (EX-ECAP) can be well fitted by two exponential components. The shorter component with the lifetime τ_1, which is lower than the bulk positron lifetime in Mg τ_B = 225 ps [122], represents a contribution of free positrons not trapped at defects. The longer component with lifetime $\tau_2 \approx 260$ ps arises from positrons trapped at dislocations [123]. All these results were published in our paper [118].

The development of positron lifetimes τ_1, τ_2 with increasing number of ECAP passes is plotted in Fig. 5.2 (a), while Fig. 5.2 (b) shows the dependence of the intensity I_2 of positron trapped at dislocations on the number of ECAP passes. The dislocation component with appreciable intensity of 20 % was detected already in the extruded alloy, i.e., prior to the ECAP processing. This testifies that dislocations were introduced into the alloy by plastic deformation during extrusion. The lifetime τ_2 of positrons trapped at dislocations remains approximately constant during ECAP processing confirming that the nature of positron traps does not change. The intensity I_2 of positrons trapped at dislocations first increases with increasing number of ECAP passes and becomes maximal in the specimen subjected to 2 passes. Further ECAP processing (more than 2 passes) causes a gradual decrease of I_2. Note that similar behaviour of the intensity of dislocation component during ECAP processing was observed in other Mg alloys (AZ80, ZK60) [124].

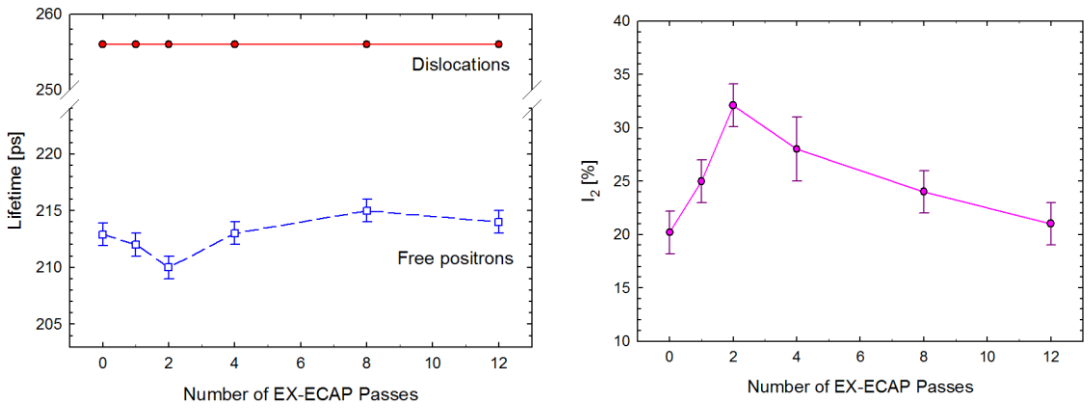

a) **b)**

Figure 5.2: Results of positron lifetime measurements for AZ31 alloy subjected to various number of EX-ECAP passes. a) Lifetimes τ_1 (squares) and τ_2 (circles) of the free positron and the dislocation component. b) Intensity I_2 of the components arising from positrons trapped at dislocations.

The dislocation density ρ_D can be calculated from positron lifetime data using the two-state simple trapping model (STM) [125]

$$\rho_D = \frac{1}{\nu_D} I_2 \left(\frac{1}{\tau_1} - \frac{1}{\tau_2} \right), \tag{5.1}$$

where ν_D is the specific positron trapping rate to dislocation which in the majority of metals falls into the range of 10^{-5}–10^{-4} m^2s^{-1} [126]. Here we used $\nu_D = 1 \times 10^{-5}$ m^2s^{-1} since Mg exhibits low electron density in interatomic regions which makes the positron binding energy to open volume defects lower than in dense metals and, thereby, ν_D is expected to be close to the lower limit of the aforementioned interval. Note that in the frame of the two-state trapping model the quantity

$$\tau_f = \left(\frac{I_1}{\tau_1} + \frac{I_2}{\tau_2} \right)^{-1} \tag{5.2}$$

equals to the bulk positron lifetime in the defect-free material. This relation was found to hold in all the specimens studied. This testifies that the alloys deformed by ECAP contain indeed a single type of defects and that dislocations are distributed relatively homogeneously in the specimens.

The mean dislocation density ρ_D calculated from Eq. (5.1) is plotted in Fig. 5.3 as a function of the number of ECAP passes. One can see in Fig. 5.3 that ρ_D first increases during ECAP processing and reaches its maximum in the sample subjected to 2 ECAP passes. However, further ECAP processing leads to a gradual decrease of dislocation density indicating a recovery of dislocation structure connected with development of UFG structure. Most probably rearrangement of dislocations and mutual annihilation of dislocations with opposite sign takes place during further ECAP processing. Finally in the sample subjected to 12 ECAP passes ρ_D decreased to the similar value as in the extruded sample prior to ECAP processing.

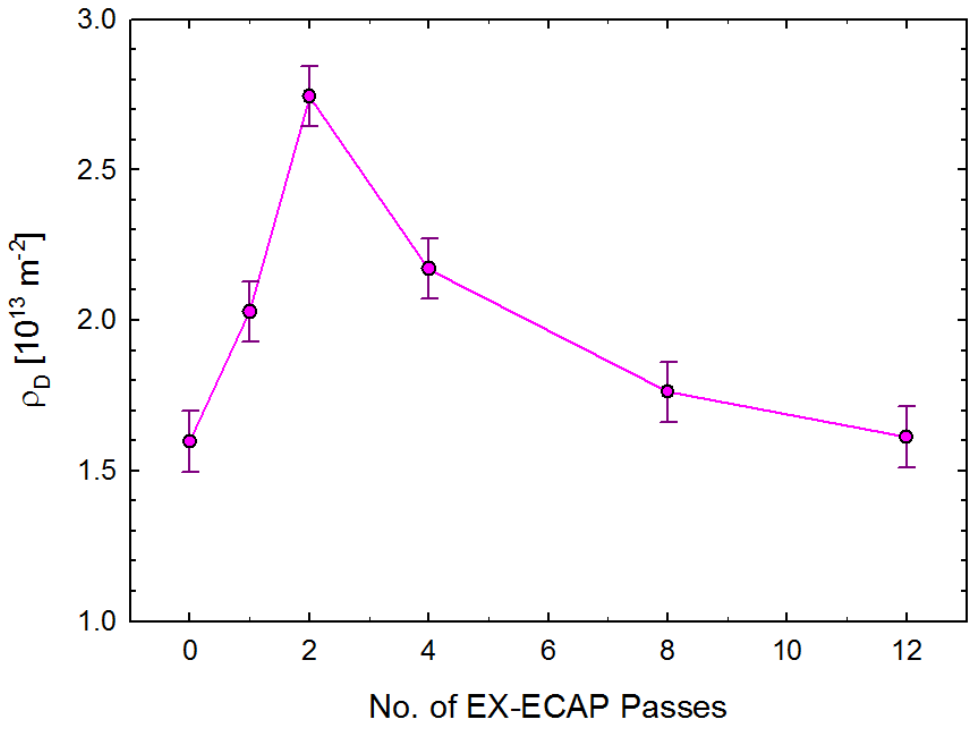

Figure 5.3: Dislocation density ρ_D in AZ31 alloy subjected to various number of EX-ECAP passes.

5.1.3 Investigation by XRD line profile analysis

In Fig. 5.4, as an example, the CMWP fitting for AZ31 alloy processed by 4 passes of ECAP is shown. Open circles and the solid line represent the measured data and the fitted curves, respectively. The area-weighted mean crystallite size $\langle x \rangle_{area}$, the density ρ_D and the character of dislocations as well as the twin boundary frequency β were determined by the line profile analysis. The twin boundary frequency is defined as the relative fraction of twin boundaries among the lattice planes acting as habit planes in twinning. In HCP materials twinning usually occurs on {10.1}, {10.2}, {11.1}, and {11.2} planes, therefore in the line profile analysis all of these twin families were considered.

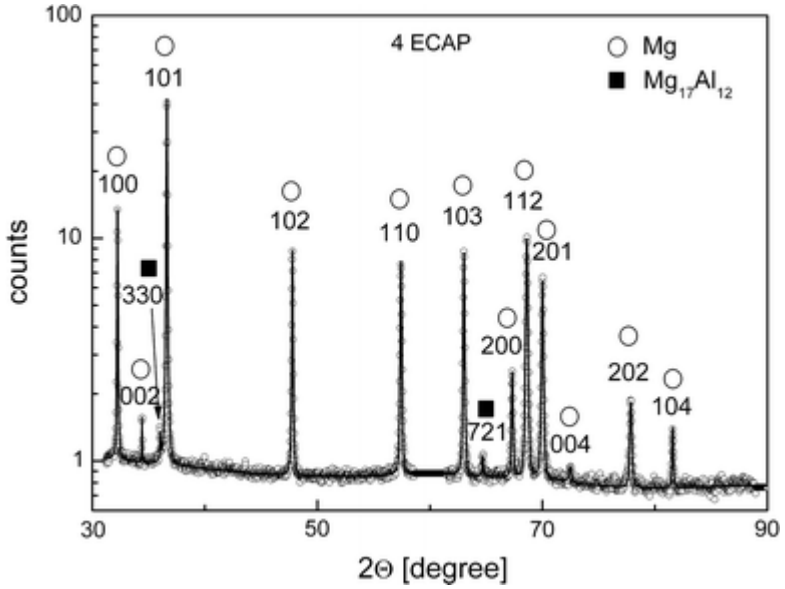

Figure 5.4: CMWP fitting of the X-ray diffraction pattern in logarithmic intensity scale for AZ31 alloy processed by 4 passes of ECAP. The open circles and the solid line represent the measured and the fitted data, respectively. The indices of reflections for the Mg matrix and the $Mg_{17}Al_{12}$ phase are also indicated.

The X-ray diffractograms revealed the existence of $Mg_{17}Al_{12}$ phase in addition to the Mg matrix. The amount of $Mg_{17}Al_{12}$ in the samples is characterized by its relative intensity in the diffractograms, i.e., the ratio of the integrated intensities of all $Mg_{17}Al_{12}$ and Mg peaks in the two theta range from 30 to 115 degrees. The values of the relative intensity (I_{rel}) are shown in Tab. 5.1. It is revealed that the amount of $Mg_{17}Al_{12}$ phase significantly increased with increasing number of ECAP passes. Most probably, before ECAP the majority of alloying elements were in solid solution and the ECAP processing at 180 °C caused the formation of $Mg_{17}Al_{12}$ precipitates.

Sample	I_{rel} [%]	$\langle x \rangle_{area}$ [nm]	ρ_D [10^{14} m^{-2}]	Fraction of screw dislocations [%]
Extruded	0	470 ± 80	0.9 ± 0.1	13 ± 13
1 ECAP	0.14 ± 0.03	173 ± 16	1.4 ± 0.1	60 ± 10
2 ECAP	0.14 ± 0.03	146 ± 15	1.7 ± 0.2	71 ± 5
4 ECAP	0.7 ± 0.1	134 ± 15	1.3 ± 0.1	47 ± 10
8 ECAP	2.6 ± 0.3	120 ± 13	1.1 ± 0.1	42 ± 17

Table 5.1: The total integrated intensity of the X-ray diffraction peaks of $Mg_{17}Al_{12}$ phase relative to the intensity for the Mg matrix (I_{rel}), the area-weigthed mean crystallite size ($\langle x \rangle_{area}$), the dislocation density (ρ_D) and the relative fraction of screw dislocations in the Mg matrix.

Considerable twinning was not observed in any of the specimens. The practically zero value of the twin boundary frequency does not mean definitely the lack of twinning as the lowest detection limit of twin boundary frequency is about 0.05 % in the present experiments that corresponds to an average twin boundary spacing of about 400 nm. If the mean twin boundary spacing is higher than this value, line profile analysis gives practically zero value for twin boundary frequency. The low level of twinning is most probably caused by the relatively small size of crystallites formed during ECAP as in HCP metals the reduction of grain size is usually accompanied by the decrease of twinning activity [127, 128].

The values of the crystallite size and the dislocation density are listed in Tab. 5.1. The crystallite size decreased up to 2 passes of ECAP then it remained unchanged within the experimental error. The dislocation density increased up to 2 passes then it decreased slightly when the number of ECAP passes increased. After 2 passes the reduction of the dislocation density along with the large increment of the amount of $Mg_{17}Al_{12}$ precipitates suggests that the alloying elements (Al and Zn) have stronger pinning effect on dislocations when they are solved in the matrix than in the form of precipitates. It is noted that the crystallite size determined by X-ray line profile analysis is smaller by a factor of about 4 than the grain size obtained by TEM. This phenomenon is well-known in the literature of SPD-processed metallic materials and can be attributed to the fact that the crystallites are equivalent to the coherently scattering domains. As the coherency of X-rays breaks even if they are scattered from volumes having quite small misorientations (1–2°), the crystallite size corresponds rather to the subgrain size in the severely deformed microstructures.

The dislocations in the different slip systems were evaluated for their edge/screw character. In this procedure, first the slip systems populated by dislocations were determined from the experimental dislocation contrast factors (q_1 and q_2) using the procedure described in [114]. In this method, the two experimental contrast factors were made equal to the weighted averages of the theoretical contrast factors for the eleven possible slip systems where the weights were one or zero for the populated or non-populated slip systems, respectively. Since the measured q values had experimental errors, their comparison with the theoretical contrast factors was carried out by introducing tolerances [114]. The evaluation procedure gave one or more sets of the eleven weights consisting of zero and one values as possible solutions. Finally, the values obtained for the screw dislocation slip systems in all solutions were summed up and divided by the sum of the values determined for all the slip systems. This number was used for the characterisation of the relative fraction of screw dislocations. Tab. 5.1 shows that the relative fraction of screw dislocations increased up to 2 passes then it decreased between 2 and 4 passes and remained unchanged between 4 and 8 passes. The Burgers-vector analysis of dislocations revealed that the majority of screw dislocations that disappeared for

higher number of ECAP passes had Burgers-vectors of $\langle c \rangle$ and $\langle c + a \rangle$ types. The strong decrease of the fraction of $\langle c \rangle$ and $\langle c + a \rangle$ screw dislocations for higher number of ECAP passes can be explained by their high self-energy due to the large Burgers-vector and the easy occurrence of their cross-slip. Annihilation of the dislocations can be caused also by the double cross-slip.

5.1.4 Microstructure

Microstructure and texture of the AZ31 after EX-ECAP was studied using EBSD and published in our paper [129]. The microstructure becomes more homogeneous with increasing number of ECAP passes and reaches the average value of grain size about 1 μm after 4 EX-ECAP passes. The process of homogenization (from bimodal to homogeneous microstructure) is quantitatively summarized in Tab. 5.2.

No. of EX-ECAP Passes	Area fraction of grains > 10 μm (from EBSD map)
Extruded	17.9 %
1	18.1 %
2	7.9 %
4	2.8 %
8	None
12	None

Table 5.2: Area fraction of large grains as a function of number of ECAP passes.

Additional detailed observations using TEM broadened this research. The samples for TEM observations were cut perpendicular to the pressing direction from the EX-ECAPed billet and prepared by mechanical grinding, dimpling and ion polishing. The microstructure of extruded samples is bimodal – consists of large grains of 50–100 μm mixed with relatively fine grains of 2–5 μm. Fig. 5.5 shows the area with smaller grains of the average size of few μm. Typical twins are clearly seen in several grains. The (00.1) basal texture of individual grains in extruded magnesium alloy observed in EBSD measurements was confirmed by the electron diffraction analysis. The contrast of individual grains on this micrograph with typical low-angle grain boundaries confirmed the analysis of diffraction patterns. The area of larger grains had a typical heavily deformed structure with high density of tangled dislocations.

Figure 5.5: Transmission electron micrograph of extruded AZ31 alloy.

Fig. 5.6 presents the microstructure of the specimen after 1 EX-ECAP pass. The bimodal character of the microstructure did not change after the first ECAP pass; the average grain size is only slightly smaller in comparison with the extruded material, see Fig. 5.6 (a). However, one significant difference between these two micrographs is observed - the character of grain boundaries. One can see many HAGBs with typical thickness fringe band contrast confirming their almost equilibrium state in this micrograph. On the other hand, several grain boundaries remained in a non-equilibrium state with diffuse fuzzy contrast and many dislocations lying in a grain boundary plane were also observed. Several areas with high density of tangled dislocations with no or only exceptional signs of substructure formation were found in this specimen, see Fig. 5.6 (b).

Subsequent TEM observation confirmed that the microstructure of EX-ECAPed samples changed only partly with increasing number of ECAP passes – fine grains were refined only slightly while the large grain zones were refined significantly. Typical microstructure of the sample processed by 2 EX-ECAP passes is shown in Fig. 5.7.

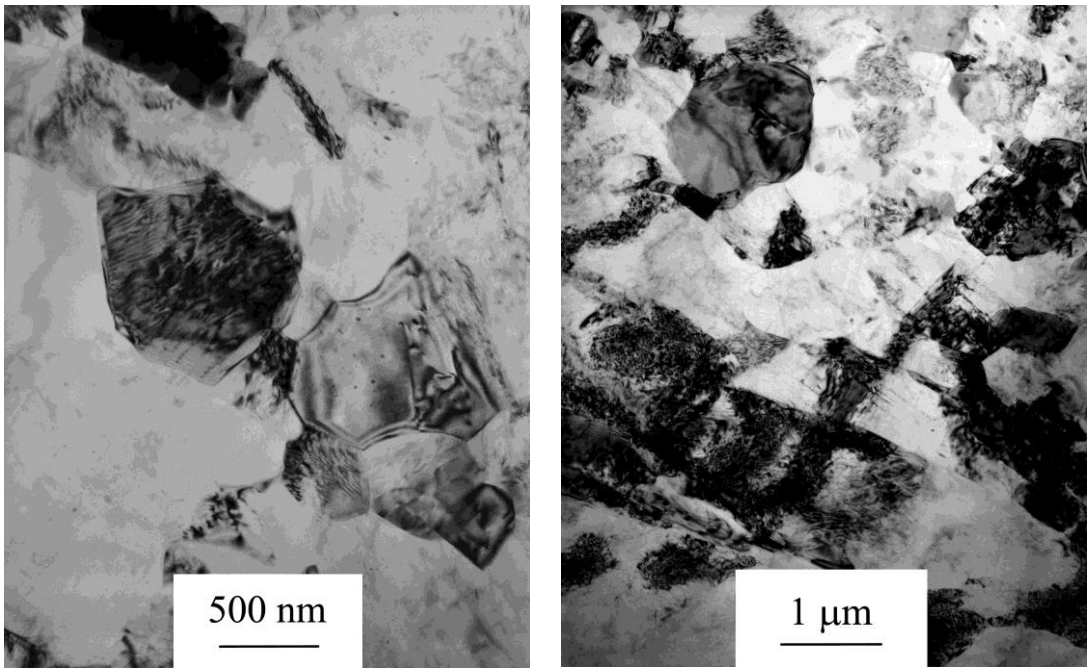

a) **b)**

Figure 5.6: Transmission electron micrographs of AZ31 alloy after extrusion and 1 pass of ECAP.

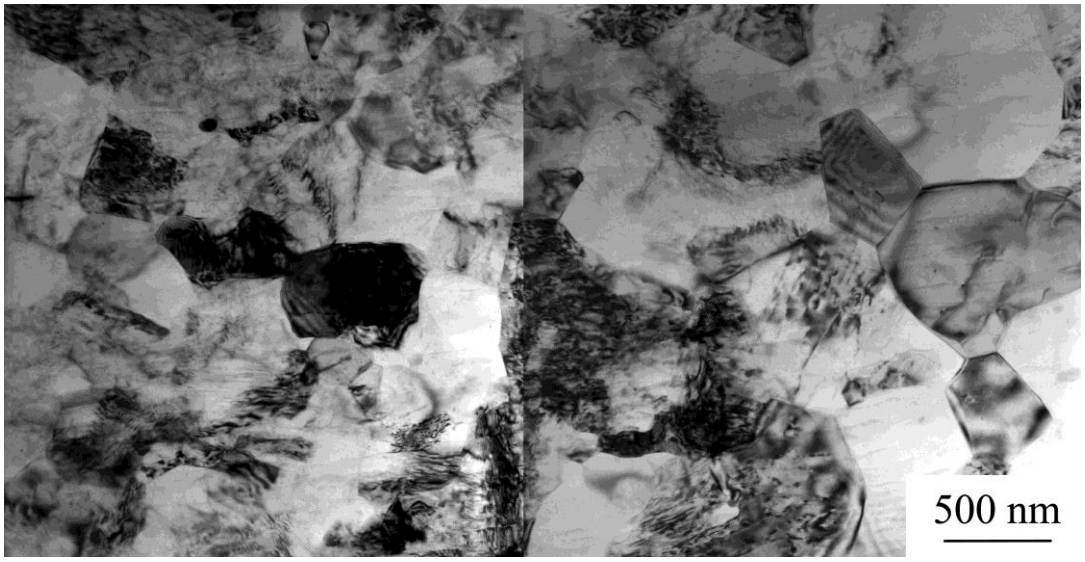

Figure 5.7: Transmission electron micrograph of AZ31 alloy after extrusion and 2 passes of ECAP.

Only fine grains of the average grain size in the submicrometer range were observed in the micrographs of the specimens after 8 and 12 ECAP passes. Fig. 5.8 (a) presents the typical microstructure of the sample after 8 passes. One can see that the grains in this micrograph are equiaxed and the grain size is approximately 800 nm. This EX-ECAPed material has significantly lower density of dislocations and equilibrium grains boundaries. A few newly recrystallized very small grains with no dislocations and sharp equilibrium boundaries were also found in the microstructure after 8 and 12 passes of EX-ECAP (cf. Fig. 5.8 (b)).

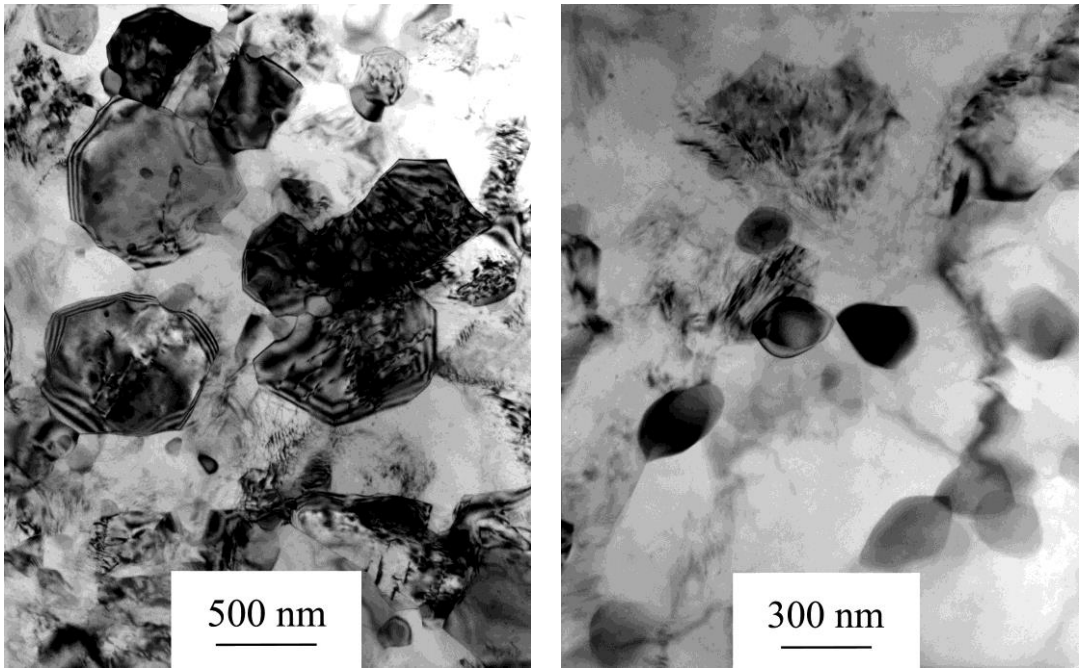

a) **b)**

Figure 5.8: Transmission electron micrograph of the AZ31 alloy (a) after 8 passes of EX-ECAP, (b) newly recrystallized small grains after 12 passes of EX-ECAP.

5.1.5 Thermal stability

5.1.5.1 Microhardness

The investigation of thermal stability was published in our recent paper [130]. Series of specimens for thermal stability investigation were prepared by isochronal annealing at the temperatures 150 – 500 °C for 1 hour followed by water-quench. The samples after extrusion and 4 passes of ECAP were chosen as suitable material because of their UFG and homogeneous microstructure with relatively high dislocation density (cf. our previous research [129]).

The results of Vickers microhardness HV0.1 measurement (at least 15 indents were made in each sample) are displayed in Fig. 5.9. The first data point in the figure (HV0.1 = 86) corresponds to the initial severely deformed specimen. Microhardness values after annealing at 150 and 170 °C do not differ significantly. However, the microhardness declines abruptly in the range of 170 - 230 °C and then continuously to 500 °C.

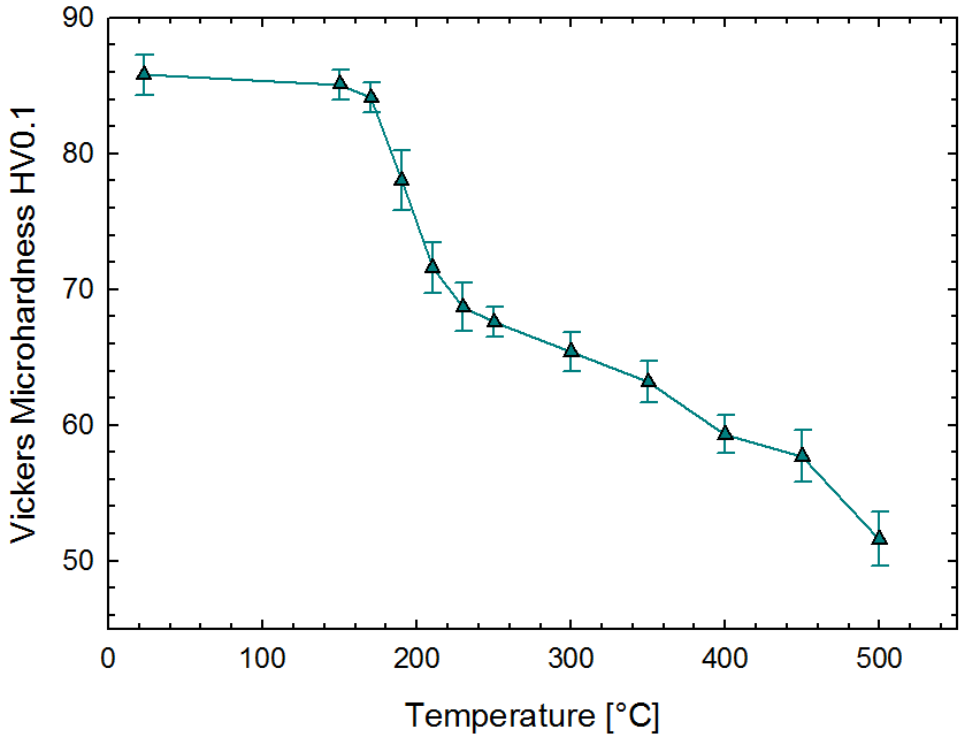

Figure 5.9: Microhardness of the AZ31 specimens processed by extrusion and 4 passes of ECAP after 1 hour of isochronal annealing.

5.1.5.2 Microstructure

The microstructure was investigated using EBSD. The microstructure and grain size distribution of the specimen in the initial non-annealed condition (after extrusion and 4 passes of ECAP are shown in Fig. 5.10 (a) and (b), respectively. The microstructure is homogeneous comprising very fine grains of the average size of 0.9 µm. The microstructure and grain sizes of the samples after 1 hour of isochronal annealing at 150 and 170 °C (not shown here) are very similar to the non-annealed specimen.

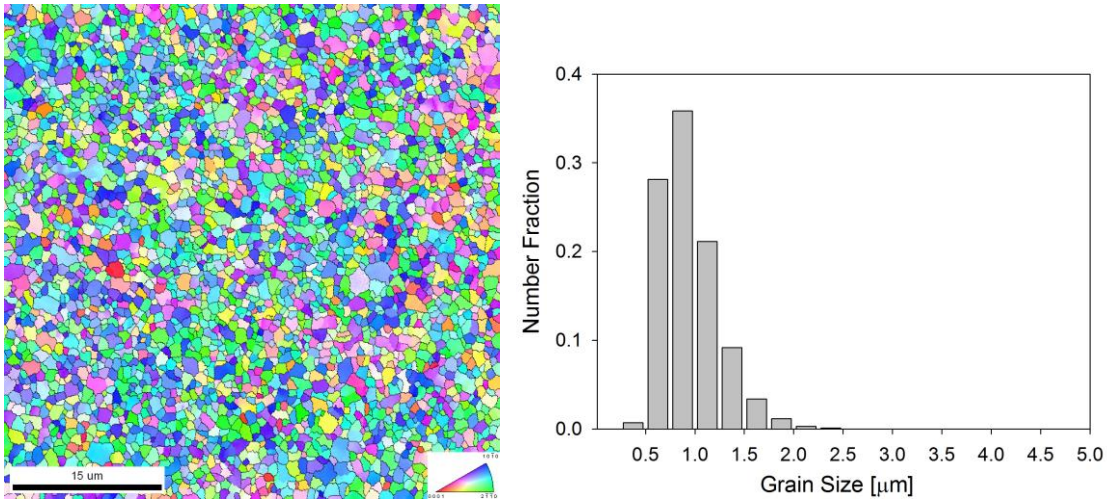

a) **b)**

Figure 5.10: Microstructure of the AZ31 sample after extrusion and 4 passes of ECAP, (a) inverse pole figure and (b) grain size distribution.

Inhomogeneous grain growth is observed at higher annealing temperatures (Fig. 5.11 – 5.17). Some grains start to grow at temperatures of 190 and 210 °C (the microstructure of the sample after annealing at 210 °C is very similar to that of 190 °C, and is not shown here). The fraction of coarse grains increases with increasing annealing temperature. At a temperature of 250 °C, some areas with original fine grains are still observed. However, the small grains are continuously disappearing at higher annealing temperatures and nearly no small grains are observed after annealing at 400 °C (see Fig. 5.15). Please note that magnification of the Fig. 5.14 (a) and 5.15 (a) is two times smaller than the magnification of the previous inverse pole figures; simultaneously, four times bigger area of the sample (100 × 100 μm) is depicted in Figs. 5.14 (a) and 5.15 (a). Microstructure of the specimens annealed at 450 and 500 °C was observed by light microscope - see Figs. 5.16 (a) and 5.17 (a), respectively.

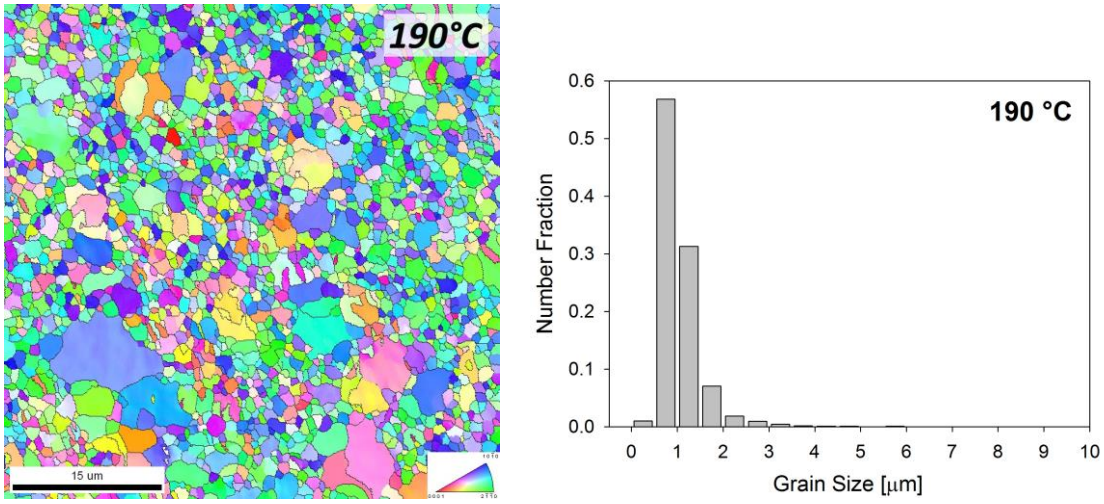

a) **b)**

Figure 5.11: Microstructure of the AZ31 EX-ECAP specimen after 1 hour of isochronal annealing at 190 °C, (a) inverse pole figure and (b) grain size distribution.

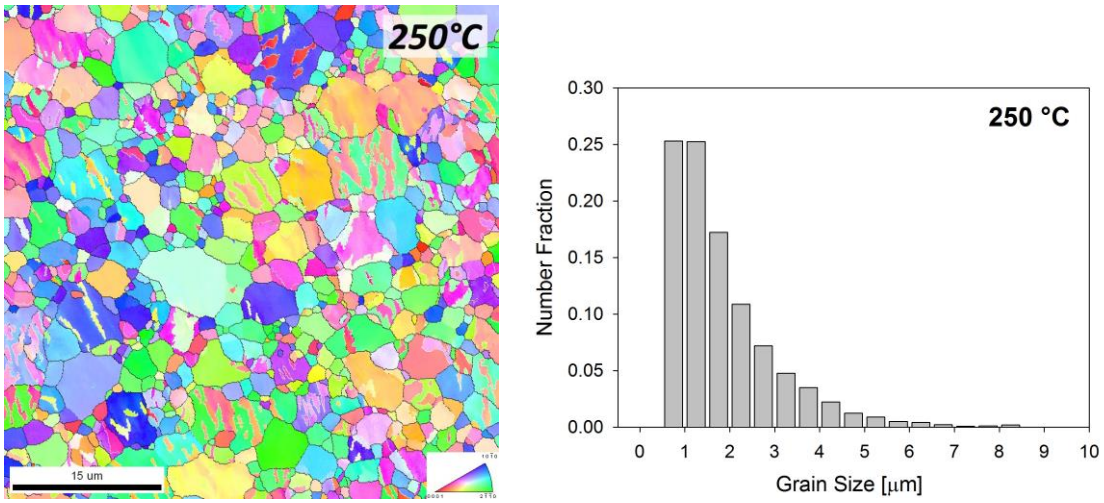

a) **b)**

Figure 5.12: Microstructure of the AZ31 EX-ECAP specimen after 1 hour of isochronal annealing at 250 °C, (a) inverse pole figure and (b) grain size distribution.

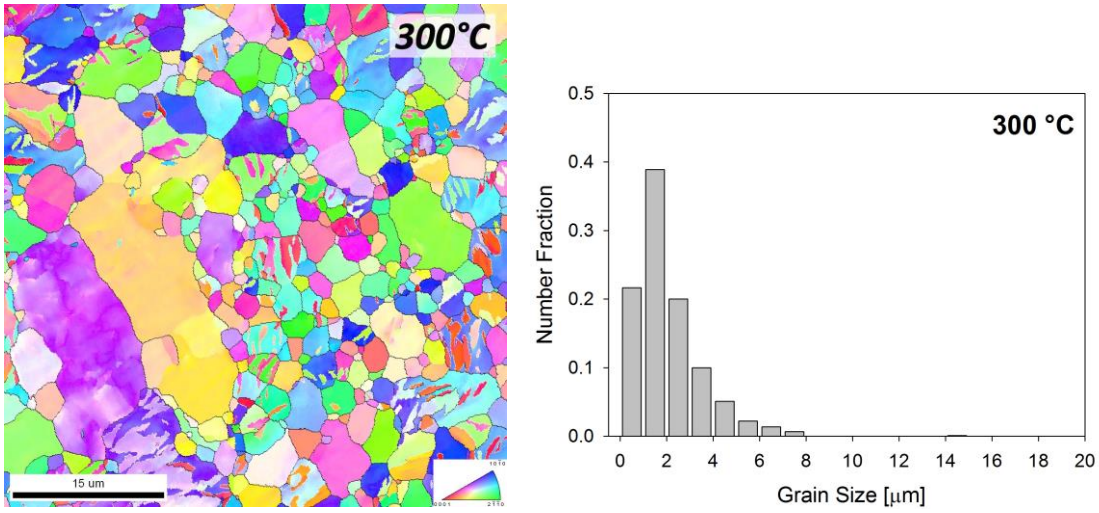

a) **b)**

Figure 5.13: Microstructure of the AZ31 EX-ECAP specimen after 1 hour of isochronal annealing at 300 °C, (a) inverse pole figure and (b) grain size distribution.

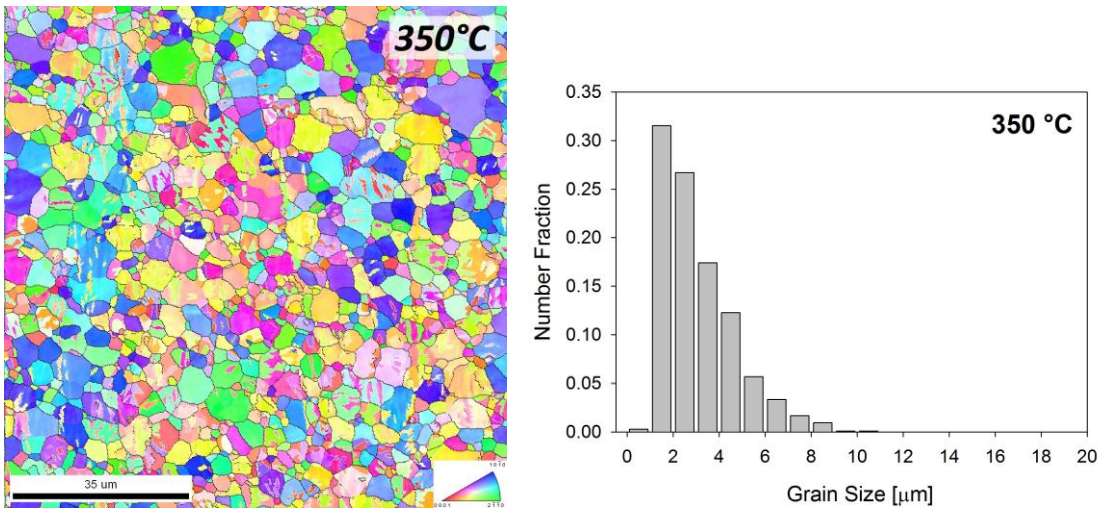

a) **b)**

Figure 5.14: Microstructure of the AZ31 EX-ECAP specimen after 1 hour of isochronal annealing at 350 °C, (a) inverse pole figure and (b) grain size distribution.

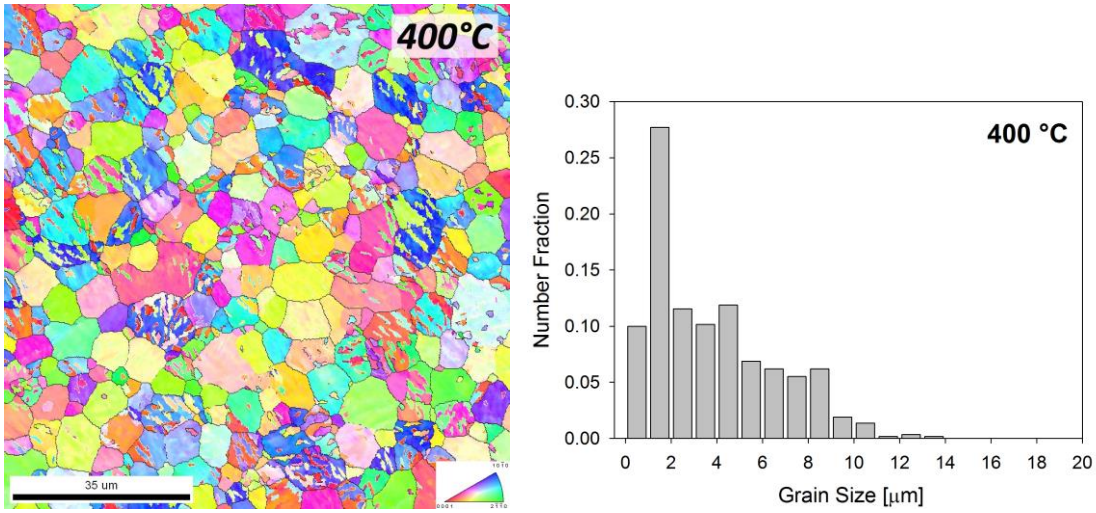

a) **b)**

Figure 5.15: Microstructure of the AZ31 EX-ECAP specimen after 1 hour of isochronal annealing at 400 °C, (a) inverse pole figure and (b) grain size distribution.

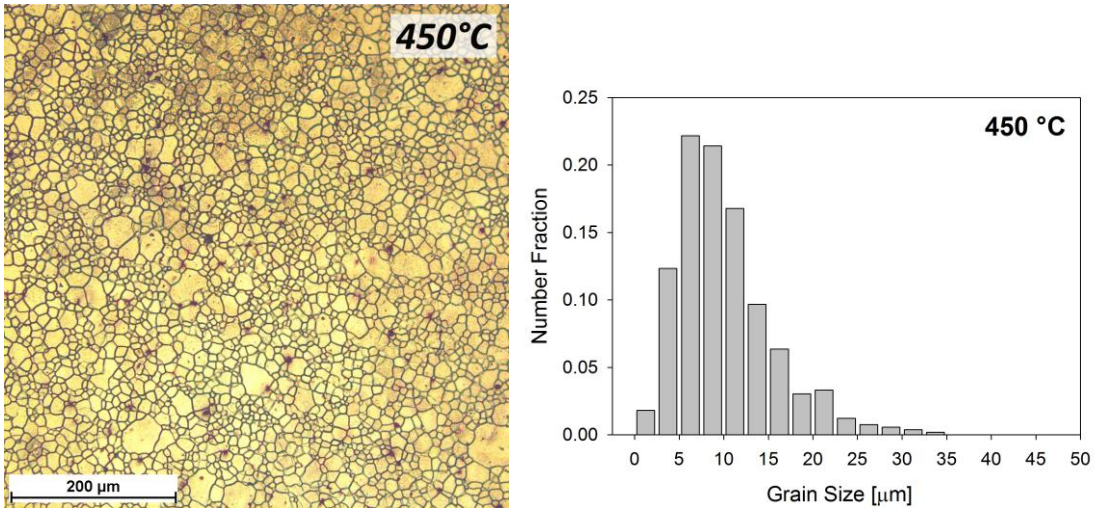

a) **b)**

Figure 5.16: Microstructure of the AZ31 EX-ECAP specimen after 1 hour of isochronal annealing at 450 °C, (a) light microscopy image and (b) grain size distribution.

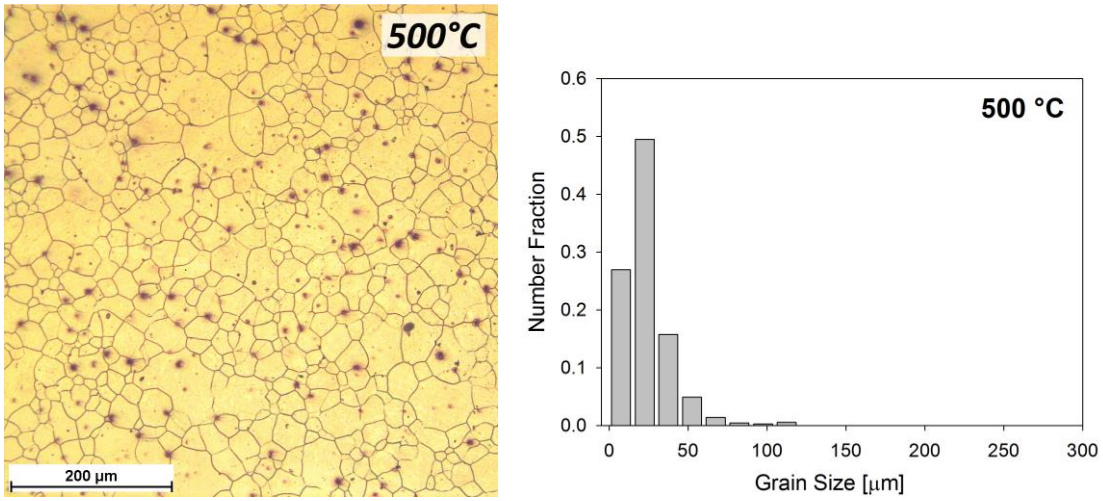

a) **b)**

Figure 5.17: Microstructure of the AZ31 EX-ECAP specimen after 1 hour of isochronal annealing at 500 °C, (a) light microscopy image and (b) grain size distribution.

Grain size distribution and average grain size of the samples studied by EBSD were calculated from data measured in the area 100 × 100 µm for all annealing temperatures to achieve better statistics. Statistical values from the samples studied by light microscopy were calculated from two or more images in order to get more than 1000 grains for each sample. Grains intersecting the edge of EBSD maps and light microscopy images were not included in the analysis. The dependence of average grain size (number average) on annealing temperature is plotted in Fig. 5.18. In the case of the samples annealed at 250 and 300 °C, the average values are calculated from the bimodal grain size distribution. Values of microhardness and average grain sizes are summarized in Tab. 5.3.

Annealing temperature [°C]	-	170	190	210	250	300	350	400	450	500
Microhardness HV0.1	85.8	84.1	78.0	71.6	67.6	65.4	63.2	59.3	57.7	51.6
Average grain size *d* [mm]	0.94	0.99	1.05	1.48	1.83	2.06	3.04	3.79	10.09	24.53

Table 5.3: Microhardness values and average grain sizes at different annealing temperatures.

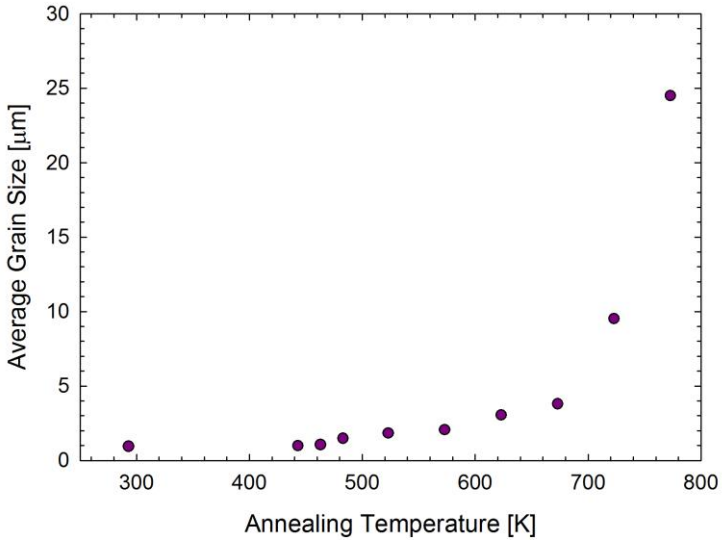

Figure 5.18: Dependence of the average grain size (number average, excluding twins) of the EX-ECAP AZ31 alloy on annealing temperature after 1 hour of isochronal annealing process.

Annealing twins observed after annealing at 250 – 400 °C (see Fig. 5.12 (a) – 5.15 (a)) were excluded from grain size calculations to achieve true grain size values (twin boundaries were ignored in grain size calculations, i.e. the twin is considered to be a part of the grain). All these twins were determined as the tensile twins with misorientation angle of 86° [131]. Twin fractions, fraction of twinned grains and the area fraction of twinned grains in samples after annealing at $T \geq 250$ °C are shown in Tab. 5.4.

Annealing Temperature	250 °C	300 °C	350 °C	400 °C
Twin Fraction	0.13	0.12	0.16	0.14
Fraction of Twinned Grains	0.26	0.26	0.37	0.40
Area Fraction of Twinned Grains	0.55	0.52	0.60	0.71

Table 5.4: Twinning in isochronally annealed EX-ECAP AZ31 alloy.

5.1.5.3 Dislocation density studied by PAS

The plastic shear deformation by EX-ECAP causes the accumulation of large plastic strain and an increase in structural defect density. These defects are stable at room temperature, but they annihilate during annealing.

Positron lifetime spectra of all samples before and after annealing can be well fitted by two exponential components. The shorter component with the lifetime τ_1 represents a contribution of free positrons not trapped at defects. The longer component with lifetime $\tau_2 \approx 260$ ps arises from positrons trapped at dislocations [123].

The development of positron lifetimes τ_1, τ_2 with increasing annealing temperature is plotted in Fig. 5.19 (a), while Fig. 5.19 (b) shows the dependence of the intensity I_2 of positron trapped at dislocations on annealing temperature. The lifetime τ_2 of positrons trapped at dislocations remains approximately constant during annealing confirming that the nature of positron traps does not change. The intensity I_2 of positrons trapped at dislocations decreases with increasing annealing temperature and becomes immeasurable at a temperature of 300 °C.

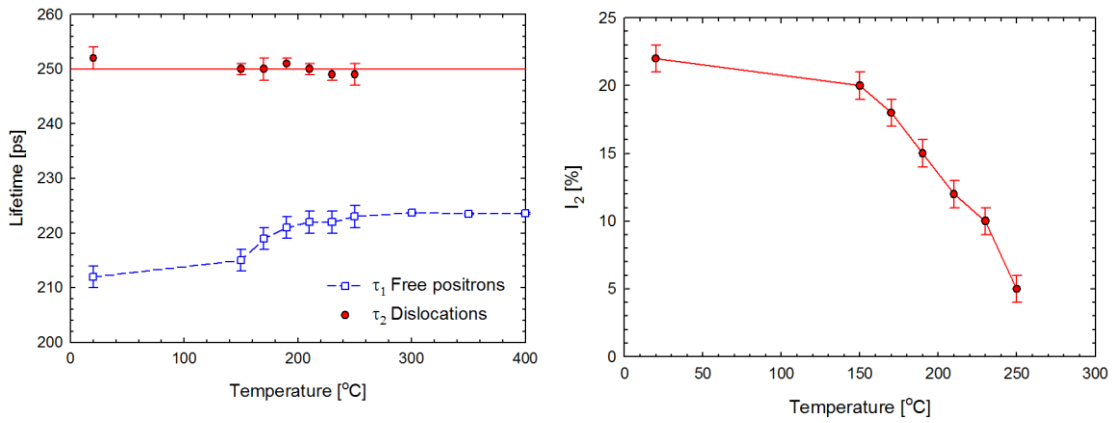

a) **b)**

Figure 5.19: Results of positron lifetime measurements for AZ31 EX-ECAP specimens subjected to 1 hour of isochronal annealing at various temperatures: a) Lifetimes τ_1 (empty squares) and τ_2 (full circles) of the free positron and the dislocation component, b) Intensity I_2 of the components arising from positrons trapped at dislocations.

The dependence of the mean dislocation density ρ_D (calculated from Eq. (5.1)) for the samples subjected to annealing treatment at various temperatures is plotted in Fig. 5.20. The dislocation density decreases with increasing annealing temperature and falls below the detection limit of positron annihilation spectroscopy at temperatures $T \geq 300$ °C.

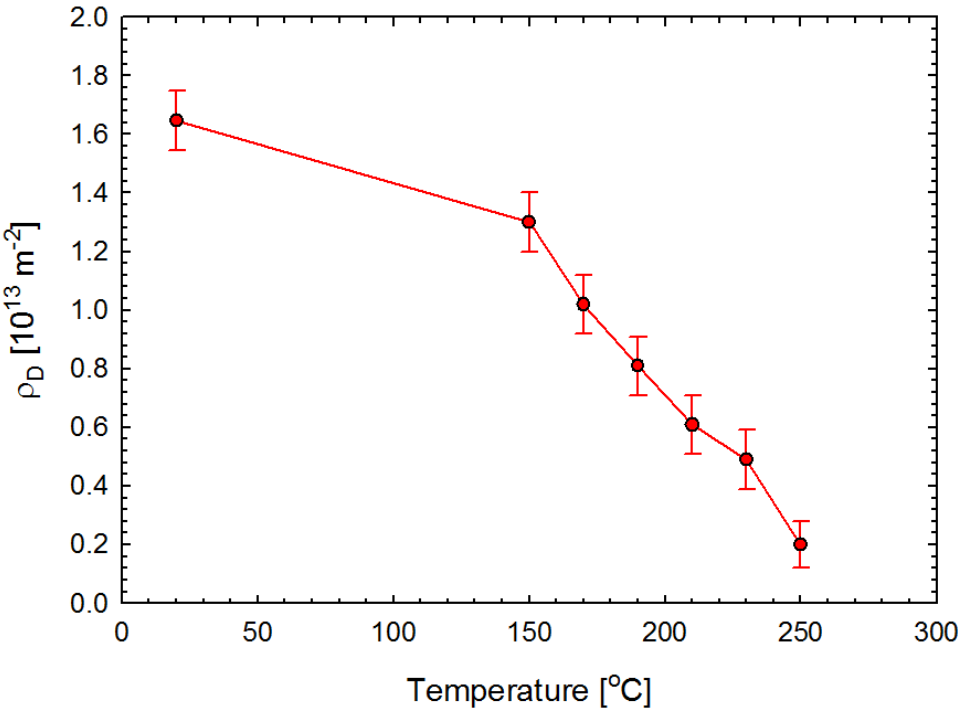

Figure 5.20: Dislocation density of the specimens after 1 hour of isochronal annealing.

5.2 Characterization of AZ31 alloy processed by HPT

5.2.1 Microhardness

Vickers microhardness (100 g load) was measured on the semi-automatic Wolpert tester allowing automatic indentation. The regular square network of indents with the step of 0.5 mm was performed in one quarter of each specimen after HPT. In order to find the exact centre of the specimen two additional lines of indents on the other half of the specimen were also done. In Fig. 5.21 the optical micrograph showing the layout of individual indents on the specimen is shown. Using this procedure the centre of each specimen was found with the accuracy of ± 0.25 mm.

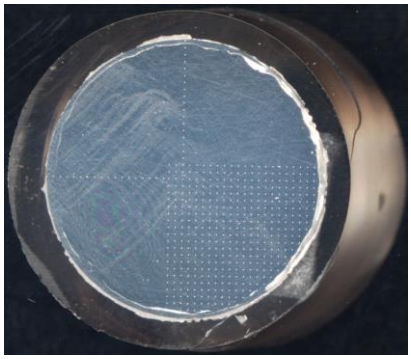

Figure 5.21: The square network of indents on the HPT specimen.

Microhardness profiles, i.e. the dependence of the microhardness on the distance *r* from the centre of the disk were measured along two perpendicular lines passing through the centre of the disk. Fig. 5.22 shows the values of Vickers microhardness measured in linear traverses across the diameter of disks of AZ31 alloy after performing HPT at room temperature at different number of rotations (N = 0, ¼, ½, 1, 5 and 15). Each data point was obtained as the average of 4 microhardness values obtained at the same distance from the centre of the disk. The scatter of the data is in the range of approximately 10% (*HV0.1* ± 5). For clarity the error bars are not shown in Fig. 5.22. The data measured on the compressed only (N=0) specimen is also shown in Fig. 5.22 to see the influence of compression and subsequent torsional straining on microhardness values.

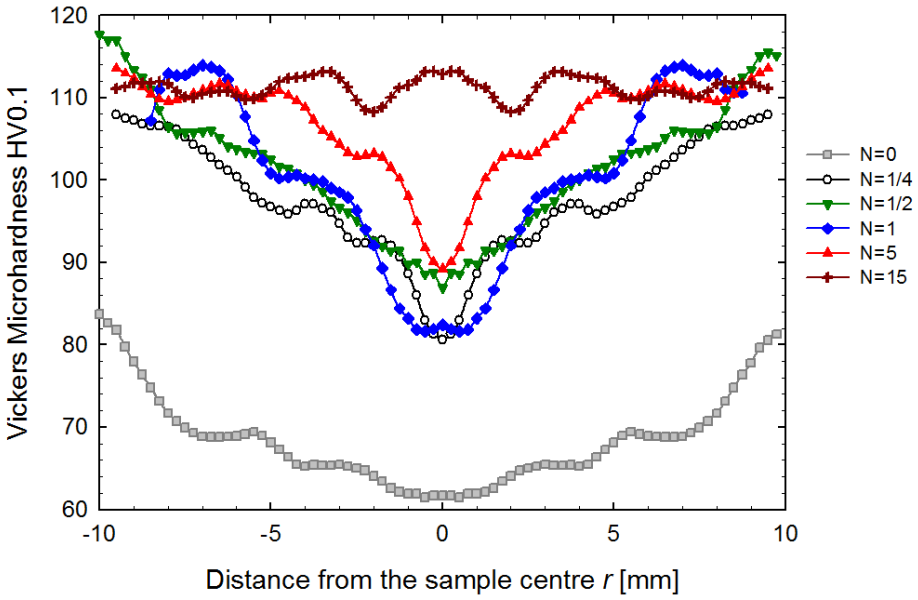

Figure 5.22: Microhardness distribution across the diameters of AZ31 disks subjected to a pressure of 2.5 GPa and up to 15 whole number of revolutions.

By detail inspecting of Fig. 5.22 it can be seen that the microhardness varies significantly with HPT deformation. HPT straining introduces an inhomogeneity in the material which is manifested by a clear minimum in microhardness values in the centre of the specimen after one turn (N=1). In this specimen the microhardness increases with increasing distance from the centre reaching its maximum of HV0.1 ≈ 110 which is approximately 30 higher than in the centre (HV0.1 ≈ 80). With increasing number of turns this difference gradually decreases by extension of the zone of maximum hardness from the periphery towards the centre of the specimen. In the specimen after 15 turns (N=15) almost homogeneous distribution of microhardness was observed if the scatter of measured data is considered. Note also that the maximum hardness does not change with increasing deformation (number of turns). Within the experimental scatter the maximum value of HV0.1 ≈ 110 was observed in all specimens.

In order to obtain more complex image of the microhardness evolution throughout individual specimens subjected to different numbers of HPT rotations three-dimensional meshes of microhardness data were constructed using the following procedure. The microhardness data were measured in one quarter of each disk as described in the previous section (approximately 400-500 indents were made in each specimen). First, these data were depicted, minimal microhardness found and matched with the centre of the sample. Due to the step of measurement the centre of the disk was found with the accuracy of ± 0.25 mm. Data for the whole specimen were constructed from measured data symmetrically with respect to the centre (data at the same distance from the centre that were measured twice were both used and the average value calculated). However, such "completed data" are not suitable for 3D-depicting. The following smoothing procedure was applied to remove each wrongly indented or evaluated datum. Each value was recomputed using the original value and values of all close neighbours (4 edge neighbours and 4 corner neighbours). The distance of corner neighbours is √2 times higher than for edge neighbours, so the weight of corner neighbours is divided by √2 in the smoothing algorithm. Smoothing can be simply demonstrated by the following equation:

$$FV = c.OV + \frac{b}{4 + 2\sqrt{2}} \sum_{i=1}^{4} \left(EN_i + \frac{CN_i}{\sqrt{2}} \right) \qquad (5.1)$$

where *FV* is the final value, *OV* is the original value, *EN* is the edge neighbour, *CN* is the corner neighbour; fraction denominator represents partial normalization and finally *c* and *b* are smoothing parameters. However *b* and *c* are not independent (because of total normalization, i.e. b + c = 1). Thus only e.g. *c* can be arbitrarily chosen. The choice *c = 1* means that no smoothing occurs, whereas minimal meaningful value of *c* is 0.12. Otherwise the weight of each edge neighbour is higher

than the weight of original values. In our case the value of $c = 0.3$ was used. It corresponds to the weight of 0.3, 0.1 and 0.07 for the original value, the edge neighbour and the corner neighbour, respectively.

Equation (5.1) holds only for interior points (a point that has all eight neighbours). Points that have incomplete number of neighbours are treated in the manner that non-existent neighbours are ignored and weights of others are appropriately adjusted. Similarly, this procedure allows healing the missing data from the interior of the sample. The procedure extrapolates any missing value from values of the neighbours (if at least 5 of 8 possible neighbours exist). This procedure allows depicting 3D plots in a readable way even for partly damaged and/or missing data.

Unlike Fig. 5.22 which is based on taking measurements of the variation in the microhardness values following diameters across disks after HPT processing, Fig. 5.23 shows integrated data across the total surface of individual disks. In Fig. 5.23 three-dimensional meshes of microhardness for specimens subjected to different number of turns are displayed. These plots were obtained by symmetrical completion of measured data and by smoothing procedure described in the previous paragraph. The variations of microhardness with position within the disk are clearly displayed at these meshes.

The inhomogeneous microhardness distribution is formed already in the specimen after ¼ HPT turn where the central region exhibits the average value of microhardness ~ 80-85 while near the periphery the microhardness varies between 110 and 115. Note, that HPT straining is very efficient in material strengthening, as already after $N = ¼$ the microhardness increased by ~ 25 and ~ 50 in the centre and the periphery of the specimen, respectively, as compared to the material which was only pressed in the HPT anvil ($N = 0$), cf. Figs. 5.23 (a) and (b). For $N = 0$ the microhardness in the centre was 60 and increased to 85 in the periphery. The enhanced microhardness observed in peripheral regions of this specimen is caused by the material outflow due to pressing and the consequent strengthening [38]. With the increasing number of HPT turns the microhardness is continuously smoothed and in the specimen after 15 turns ($N = 15$) almost homogenous distribution of microhardness was measured.

The detailed inspection of 3D plots in Fig. 5.23 reveals the undulating character of microhardness variations and the development of deformation in the material which is consistent with the model of strain gradient plasticity [132]. For a low stacking fault energy material such as the AZ31 alloy ($\gamma = 27.8$ mJ/m^2 [133]) this model predicts a two-stage development of microhardness undergoing inhomogeneous straining. Initially, in early stages of HPT straining, the microhardness distribution is characterized by low values in the specimen centre and much higher values in regions near its periphery. With increasing strain introduced to

the material by HPT processing the microhardness tends to saturate by continuous extending of the region of high microhardness from the specimen periphery towards its centre.

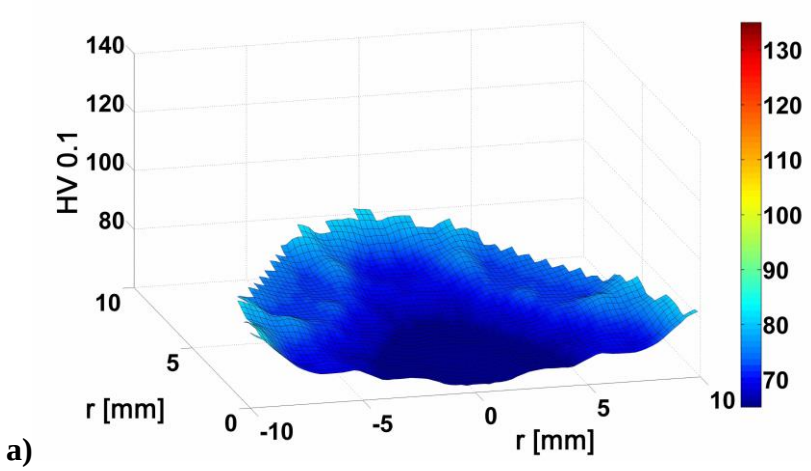

a)

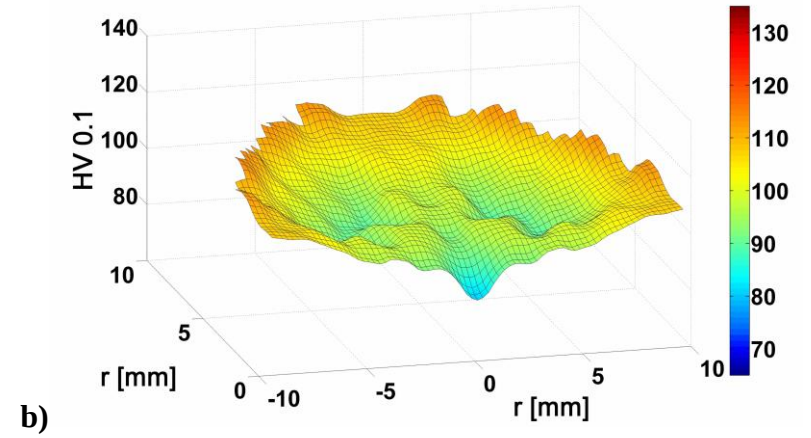

b)

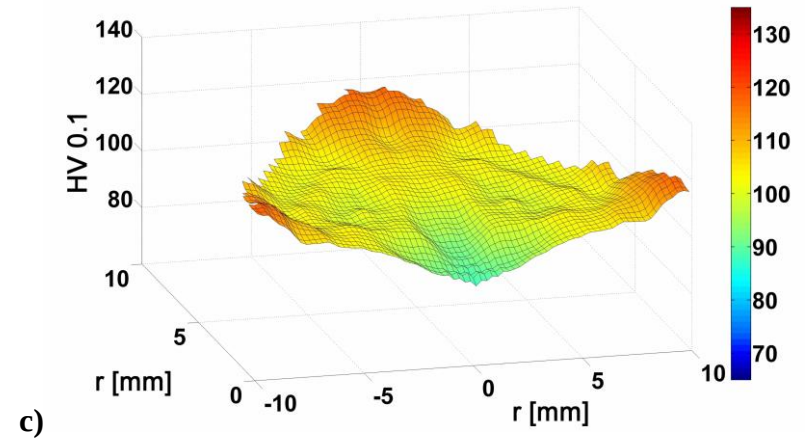

c)

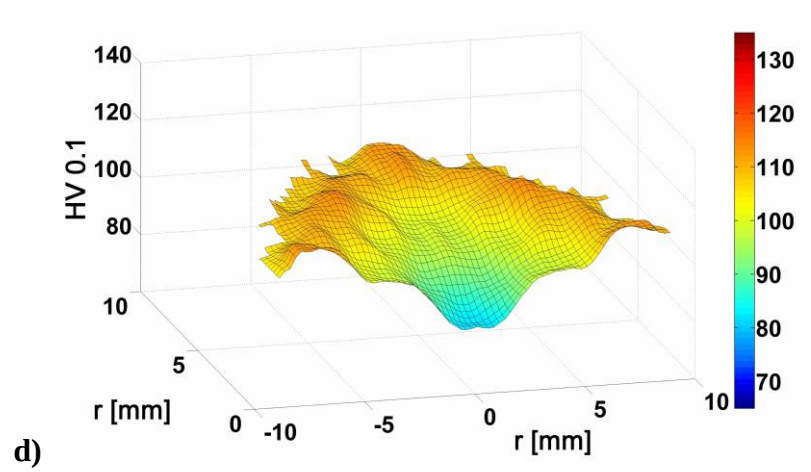

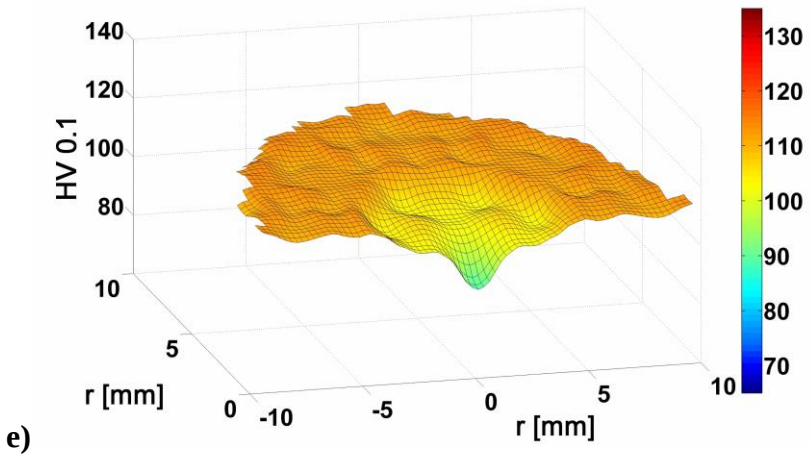

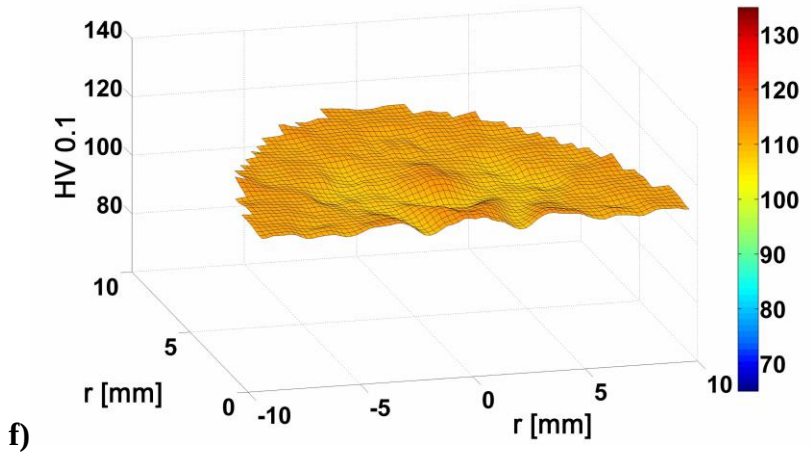

Figure 5.23: Three- dimensional meshes of microhardness HV0.1 as a function of the number of turns *N*: a) *N* = 0 (pressed only), b) *N* = ¼, c) *N* = ½, d) *N* = 1, e) *N* = 5 and f) *N* = 15.

5.2.2 Dislocation density studied by PAS

In order to examine the homogeneity of UFG structure, positron lifetime measurements of HPT deformed samples were performed at various distances *r* from the centre of the sample disk corresponding to the rotation axis of torsion deformation. Measurements at various distances *r* were performed simply by moving the positron source spot from the sample centre towards its periphery and recording positron lifetime spectra at various distances of the source spot from the centre. The uncertainty in position of the positron source was ~ 0.1 mm.

Fig. 5.24 shows the radial dependence of the mean positron lifetime for alloys subjected to various number of HPT revolutions. The mean lifetime is a robust parameter unaffected by mutual correlations between individual fitting parameters and can show general trends in studied samples. From inspection of Fig. 5.24 it becomes clear that during the first HPT revolution (i.e. in samples subjected to N = ¼, ½ and 1 turn) the mean lifetime increases with increasing strain, while for samples subjected to more than 1 HPT revolution gradually saturates. For the sample which was only pressed between the anvils (N = 0) there is no statistically significant difference between the mean lifetime at the periphery and at the centre. On the other hand, for all samples subjected to HPT deformation (N > 0) the mean lifetime is higher at the periphery than in the centre.

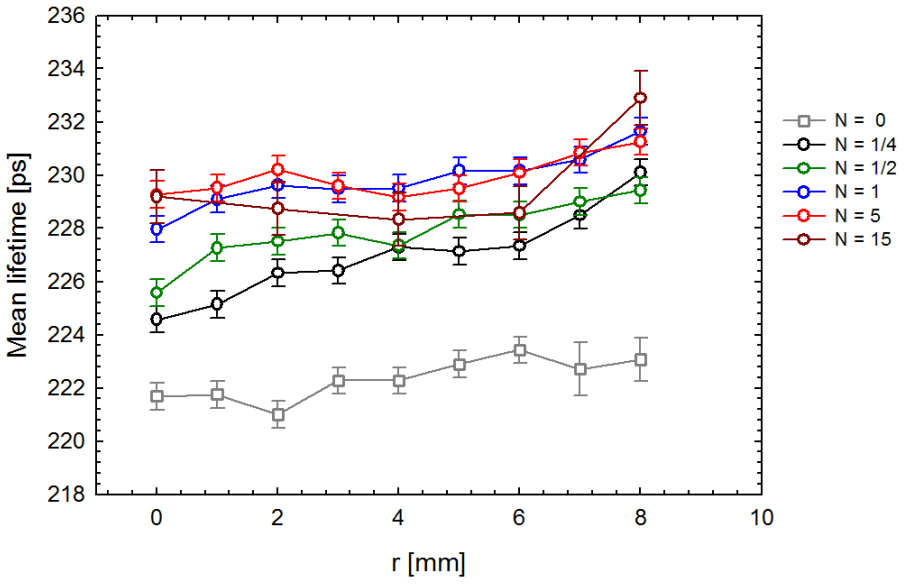

Figure 5.24: Radial dependence of the mean positron lifetime for samples subjected to various number *N* of HPT revolutions.

More information can be obtained from decomposition of positron lifetime spectra into the individual components. Positron lifetime spectra of all HPT deformed samples can be well described by two exponential components with lifetimes τ_1 and τ_2. The first one can be undoubtedly attributed to free positrons not trapped at defects. The second component represents a contribution of positrons trapped at dislocations in magnesium. Thus, the lattice defect structure in the HPT specimens is similar to the structure after extrusion and ECAP – dislocations are the only one type of lattice defect in material.

The dependence of the positron lifetimes τ_1, τ_2 on the radial distance r from the centre of the sample disk is plotted in Fig. 5.25 for specimens subjected to various number of HPT revolutions. Obviously the lifetime τ_2 remains approximately constant testifying that the nature of positron traps remains unchanged, i.e. in all samples studied positrons are trapped at dislocations. The lifetime τ_1 of the free positron component varies due to changes in density of defects. The relative intensity I_2 of the dislocation component is shown in Fig. 5.26. In the sample which was only pressed but not subjected to torsion straining ($N = 0$) the intensity I_2 remains approximately constant across the sample. On the other hand, the samples subjected to HPT deformation ($N > 0$) exhibit enhanced intensity I_2 at the periphery. Hence the dislocation density at the periphery is always higher than in the centre due to higher strain imposed at the periphery by HPT processing.

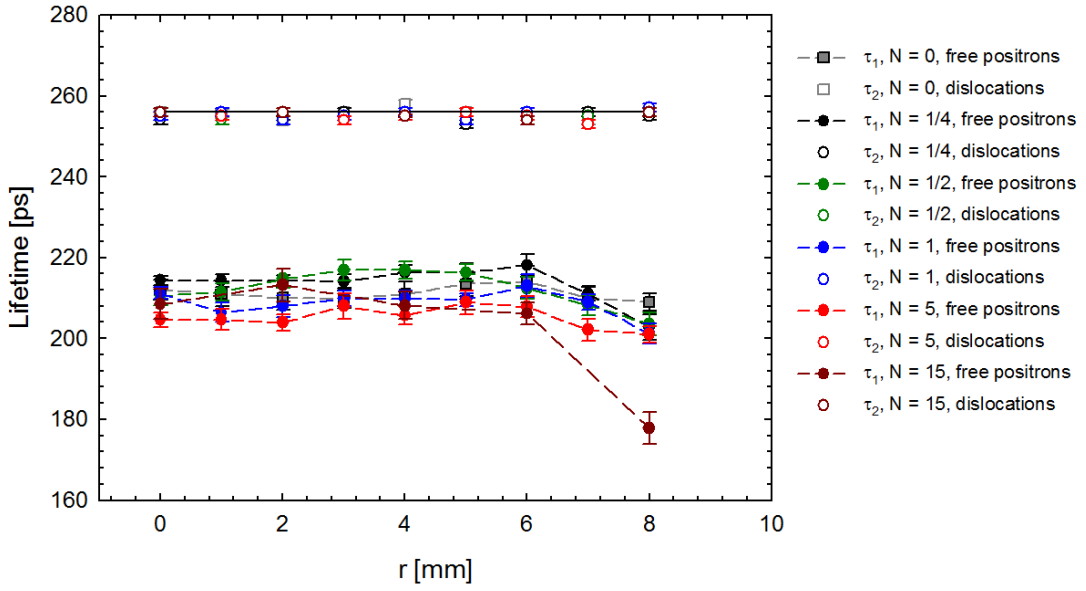

Figure 5.25: Lifetimes τ_1, τ_2 of the components resolved in positron lifetime spectra as a function of the radial distance r from the centre of the sample for specimens subjected to various number N of HPT turns.

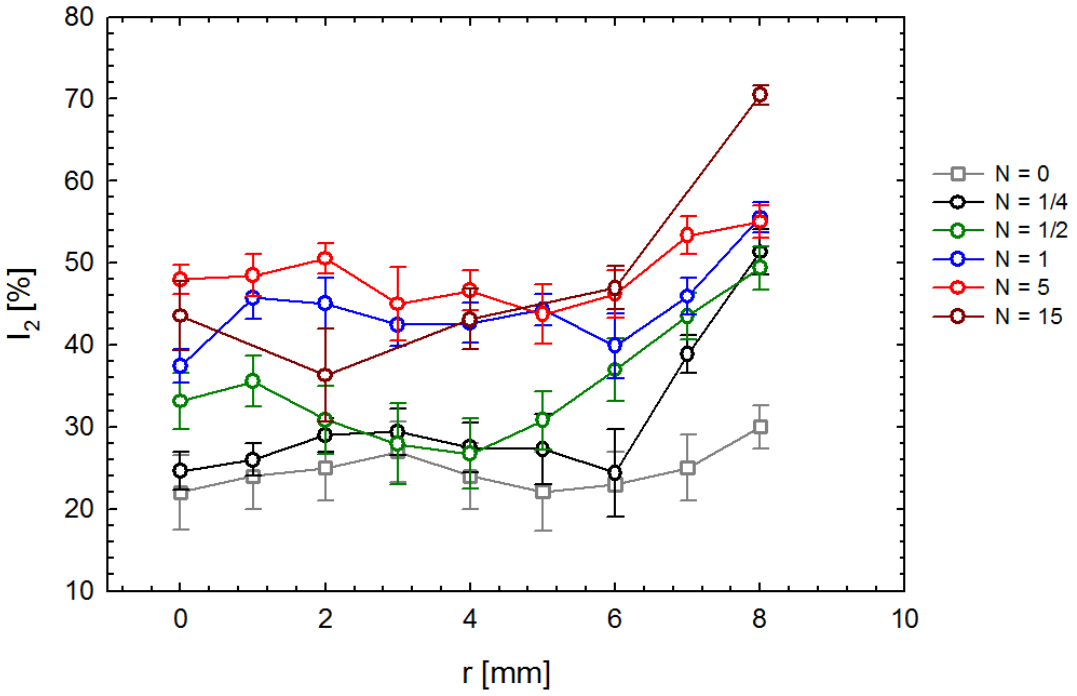

Figure 5.26: Radial distance of the relative intensity I_2 of positrons trapped at dislocations for specimens subjected to various number N of HPT revolutions.

Radial distance of the mean dislocation density ρ_D (calculated from Eq. (5.1)) for the samples subjected to various number of HPT revolutions is plotted in Fig. 5.27. From inspection of the figure one can conclude that during HPT processing the dislocation density increases firstly at the periphery (c.f. samples subjected to N = ¼ and ½ revolution) which is subjected to the highest strain. For samples subjected to more than half of HPT revolution dislocation density increases also in the centre. However, the difference between the centre and the periphery (i.e. lower ρ_D in the centre and higher at the periphery) remains also in the samples subjected to more HPT revolutions. This can be clearly seen in Fig. 5.28 showing the dislocation density in the centre (r = 0 mm) and at the periphery (r = 8 mm) as a function on the number of HPT revolutions. The highest dislocation density was observed at the periphery of the sample subjected to 15 HPT revolutions. This sample exhibits also the largest difference between the dislocation density in the centre and at the periphery.

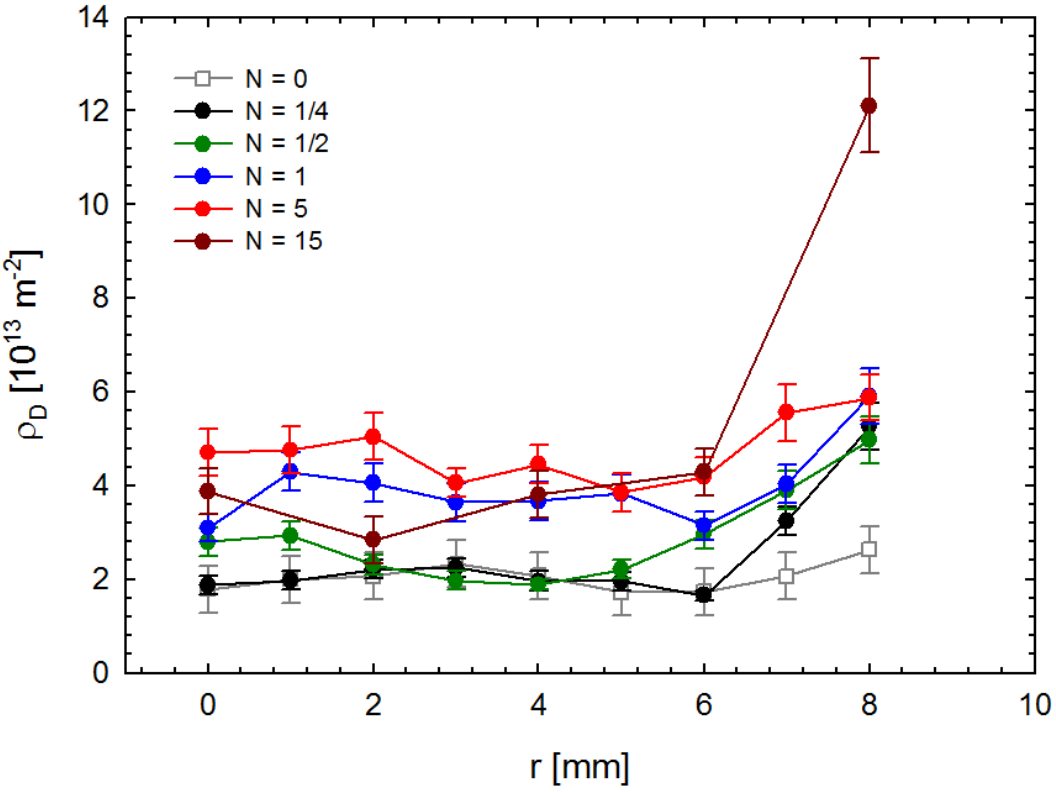

Figure 5.27: Density of dislocations ρ_D at various distances r from the centre of the sample disk for specimens subjected to various number N of HPT revolutions.

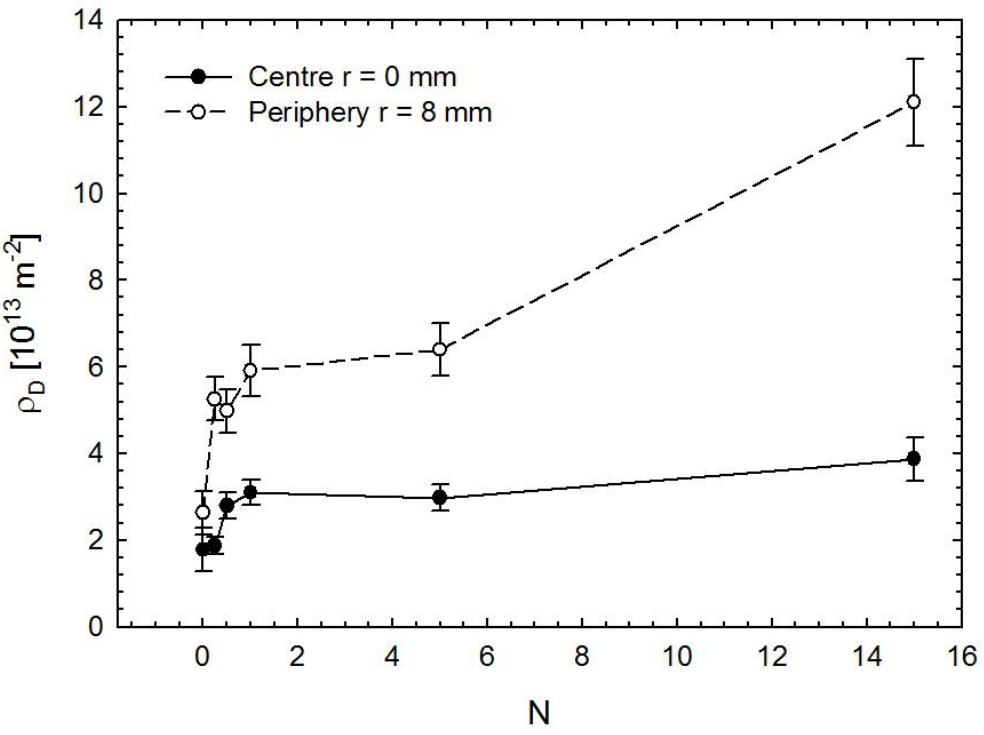

Figure 5.28: Dependence of the dislocation density ρ_D in the centre (r = 0 mm) and at the periphery (r = 8 mm) for samples subjected to various number N of HPT revolutions.

5.2.3 Investigation by XRD line profile analysis

The evolution of the crystallite size and the dislocation structure were investigated by X-ray line profile analysis (XLPA). The size of the X-ray beam spot on the sample surface was about 2×0.2 mm^2, where the longer dimension of the rectangular spot was set to be perpendicular to the disk diameter. XLPA measurements were carried out in the centre and the periphery of the disks. As an example, the fitting for the centre of the disk processed by ½ HPT turn is shown in Fig. 5.29. The open circles and the solid line represent the measured data and the fitted curve, respectively.

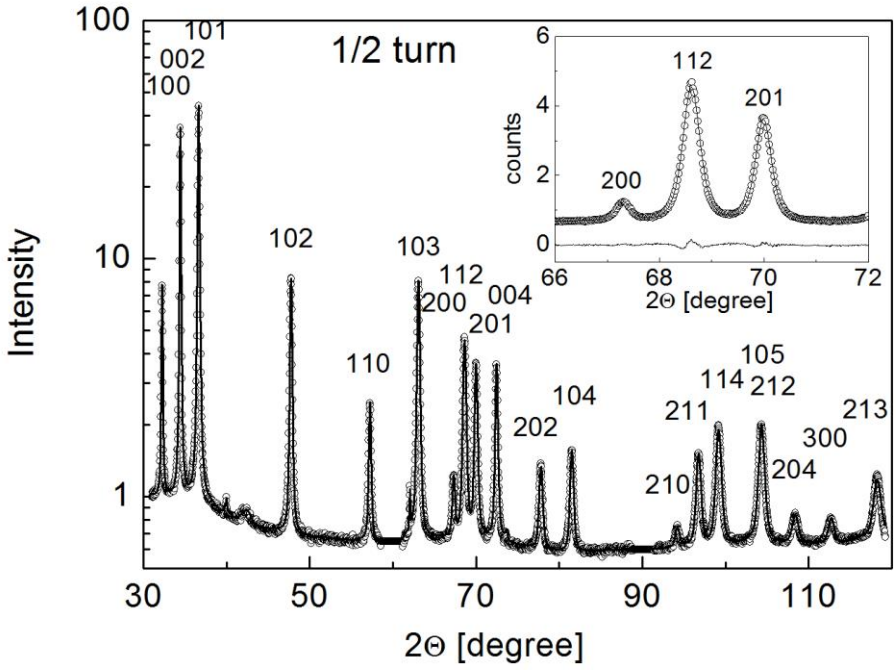

Figure 5.29: The CMWP fitting for the centre of the disk processed by ½ HPT turn. The open circles and the solid line represent the measured data and the fitted curves, respectively. The intensity is plotted in logarithmic scale. The inset shows a part of the diffractogram with larger magnification. In the inset the intensity is plotted in linear scale and the difference between the measured and the fitted patterns is shown at the bottom.

The area-weighted mean crystallite size and the dislocation density at the centre and the periphery of the disks for different number of HPT turns are listed in Tab. 5.5. The evolution of the crystallite size and the dislocation density as a function of HPT turns are plotted in Figs. 5.30 and 5.31, respectively.

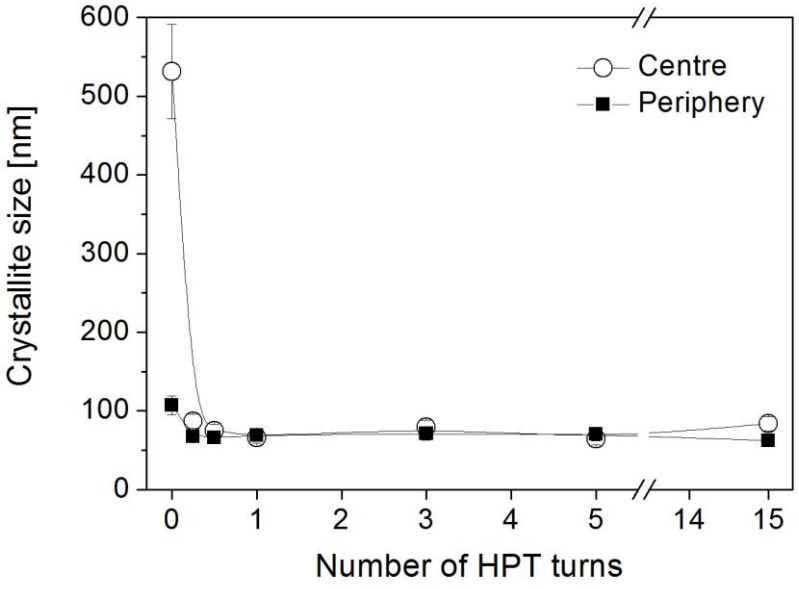

Figure 5.30: The average crystallite size versus the number of turns for the centre and the periphery of the HPT processed disks

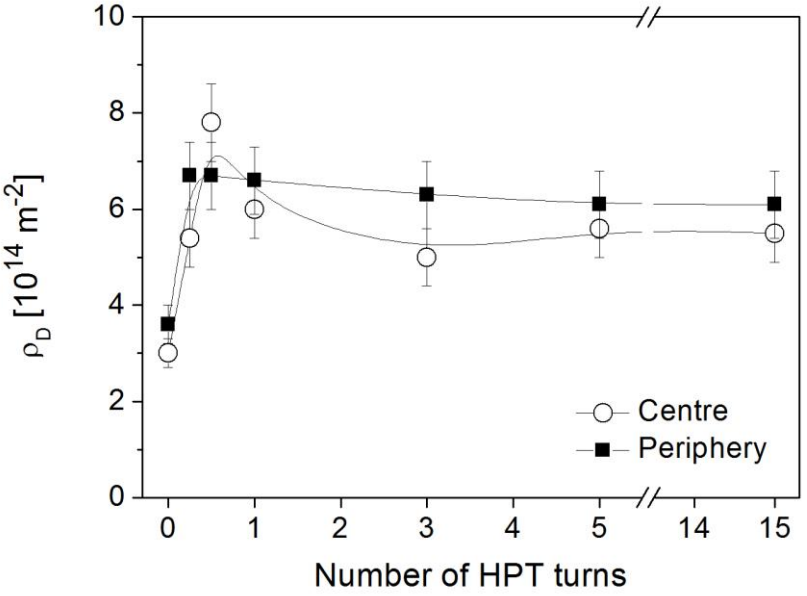

Figure 5.31: The dislocation density versus the number of turns for the centre and the periphery of the HPT processed disks.

Number of HPT turns	$\langle x \rangle_{area}$ [nm]	ρ_D [10^{14} m^{-2}]
Centre		
0	531 ± 60	3 ± 0.3
¼	87 ± 9	5.4 ± 0.6
½	75 ± 8	7.8 ± 0.8
1	66 ± 7	6 ± 0.6
3	79 ± 9	5 ± 0.6
5	64 ± 7	5.6 ± 0.6
15	84 ± 9	5.5 ± 0.6
Periphery		
0	107 ±12	3.6 ± 0.4
¼	67 ± 7	6.7 ± 0.7
½	66 ± 7	6.7 ± 0.7
1	69 ± 8	6.6 ± 0.7
3	71 ± 8	6.3 ± 0.7
5	70 ± 8	6.1 ± 0.7
15	62 ± 7	6.1 ± 0.7

Table 5.5: The area-weighted mean crystallite size $\langle x \rangle_{area}$ and the dislocation density ρ_D at the centre and the periphery of the disks for different number of HPT turns.

There is a significant density of dislocations (~3×10^{14} m^{-2}) even in the initial sample which was subjected to a pressure of 2.5 GPa in the HPT facility without rotation (0 turn). The dislocation density increased twice while the crystallite size considerably decreased due to HPT. However, the crystallite size and the parameters of the dislocation structure saturated even after ¼ HPT turn and significant changes were not observed with increasing deformation up to 15 revolutions.

The dislocation arrangement parameter *M* as a function of the number of HPT turns is plotted in Fig. 5.32. The parameter *M* considerably decreased due to HPT processing even after ¼ turn and did not change significantly with the increasing number of revolutions. The lower value of *M* indicates a more screened strain field of dislocations due their arrangement into low energy configurations, such as dipoles or low angle grain boundaries. The slightly lower *M* at the periphery indicates a more advanced stage in this process due to the larger imposed strain.

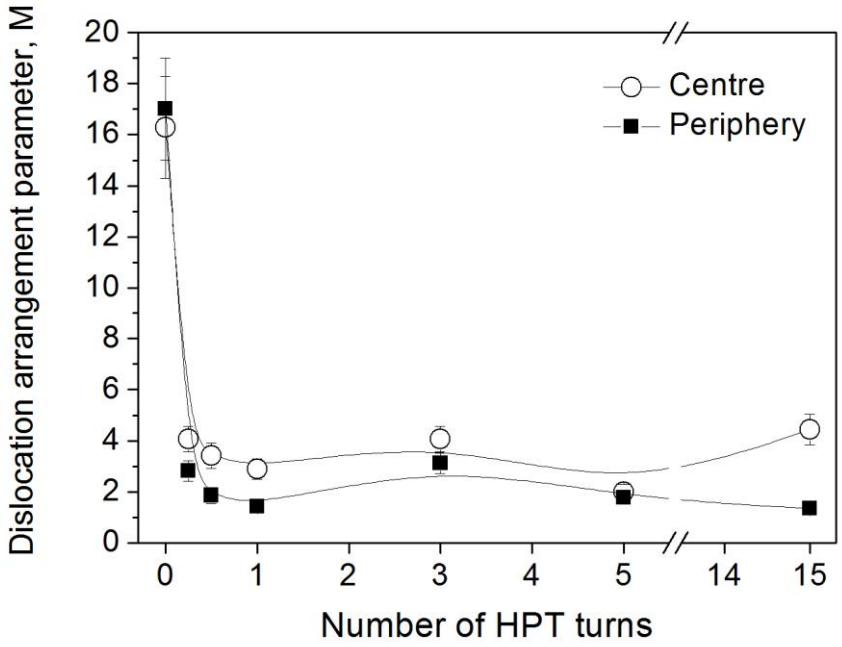

Figure 5.32: The dislocation arrangement parameter *M* versus the number of HPT turns for the centre and the periphery of the HPT processed disks.

The populations of the eleven dislocation slip systems at the centre and the periphery for different number of HPT revolutions are summarized in Tab. 5.6 and 5.7, respectively. The notations of the different slip systems used in the tables can be found elsewhere [116, 134]. It should be noted that for Mg the contrast factors of prismatic (PrE) and pyramidal (PyE) dislocations in the <a>-type slip system family are close to each other [134]. Therefore, the evaluation software cannot distinguish between them and they receive nearly equal populations. The same is valid for Py2E and Py4E edge dislocations in the <c+a>-type slip system family. Tabs. 5.5 and 5.6 show that the majority of dislocations have <a>-type Burgers-vector (60-80%) in both the initial (compressed) and HPT processed states. This can be explained by their lowest formation energy due to their shortest Burgers vector. The relative fraction of screw dislocations increased from ~10% (compressed state) to 30-40% due to HPT straining.

Centre	<a>				<c>		<c+a>				
Number of HPT turns	f_{BE}	f_{PrE}	f_{PyE}	f_{S1}	f_{Pr2E}	f_{S3}	f_{Pr3E}	f_{Py2E}	f_{Py3E}	f_{Py4E}	f_{S2}
0	78				8		14				
	15	30	26	7	3	5	3	4	3	4	0
¼	69				13		18				
	21	16	16	16	0	13	3	4	3	4	4
½	75				14		11				
	23	17	18	17	0	14	2	2	2	2	3
1	68				13		19				
	21	15	16	16	0	13	4	4	3	4	4
3	72				12		16				
	21	17	17	17	3	9	4	4	3	3	2
5	63				14		23				
	18	12	16	17	2	12	5	5	4	4	5
15	72				11		17				
	19	18	18	17	2	9	4	4	3	3	3

Table 5.6: The relative fractions in percentage for different dislocation slip systems at the centre of the disks processed by HPT for various numbers of turns.

Periphery	<a>				<c>		<c+a>				
Number of HPT turns	f_{BE}	f_{PrE}	f_{PyE}	f_{S1}	f_{Pr2E}	f_{S3}	f_{Pr3E}	f_{Py2E}	f_{Py3E}	f_{Py4E}	f_{S2}
0	79				6		15				
	14	34	28	3	2	4	3	5	3	4	0
¼	71				13		16				
	22	16	17	16	0	13	3	3	3	3	4
½	65				16		19				
	19	13	14	19	0	16	3	4	3	4	5
1	58				23		19				
	14	12	12	20	0	23	3	4	4	4	4
3	68				15		17				
	21	15	15	17	0	15	3	3	3	4	4
5	66				13		21				
	19	13	17	17	1	12	4	4	4	4	5

Periphery	<a>				<c>		<c+a>				
15	73				11		16				
	20	16	20	17	1	10	3	4	3	3	3

Table 5.7: The relative fractions in percentage for different dislocation slip systems at the periphery of the disks processed by HPT for various numbers of turns.

The evolution of the fraction of screw dislocations as a function of HPT turns is plotted in Fig. 5.33 for both the central and peripheral parts of the deformed disks. It should be noted that the fraction of screw dislocations saturated even at ¼ turn and significant difference between the values in the centre and the periphery was not observed, in accordance with the evolution of other parameters of the dislocation structure.

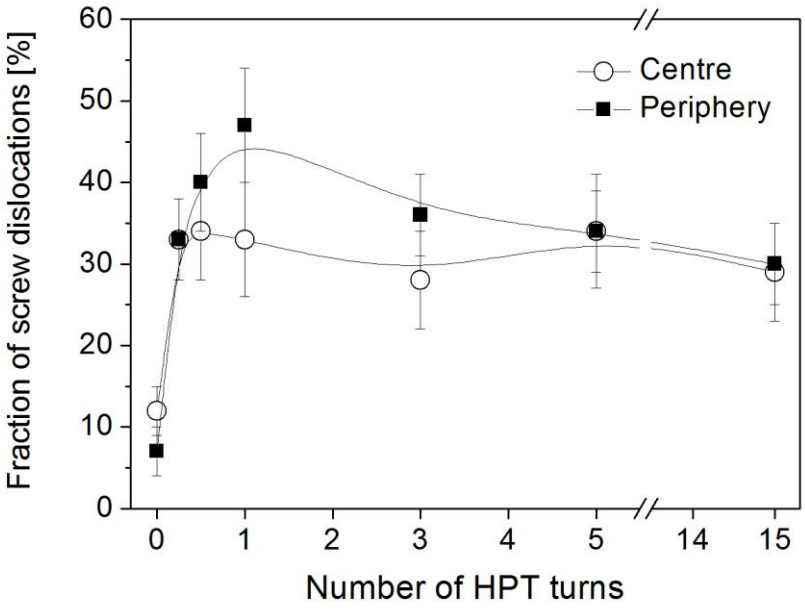

Figure 5.33: The relative fraction of screw dislocations versus the number of turns for the centre and the periphery of the HPT processed disks.

It is noted that the fraction of screw dislocations during ECAP processing was even larger (50-70%) than in the case of HPT [118], since the high pressure in the latter procedure hinders the lattice diffusion, thereby impeding the annihilation of edge dislocations. The increment in screw dislocation population due to HPT was accompanied by the reduction of the fractions of PrE and PyE <a>-type edge dislocations from about 30% to 15% during HPT, as shown in Fig. 5.34. However, the population of basal (BE) dislocations slightly increased from 15% to 20% during

HPT. Similar evolution of the dislocation fractions occurred in the periphery of the disks. This change in the dislocation population can be explained by the fact that in Mg with c/a lattice parameters ratio larger than 1.6 the slip occurs most easily in the basal plane at low temperatures [135].

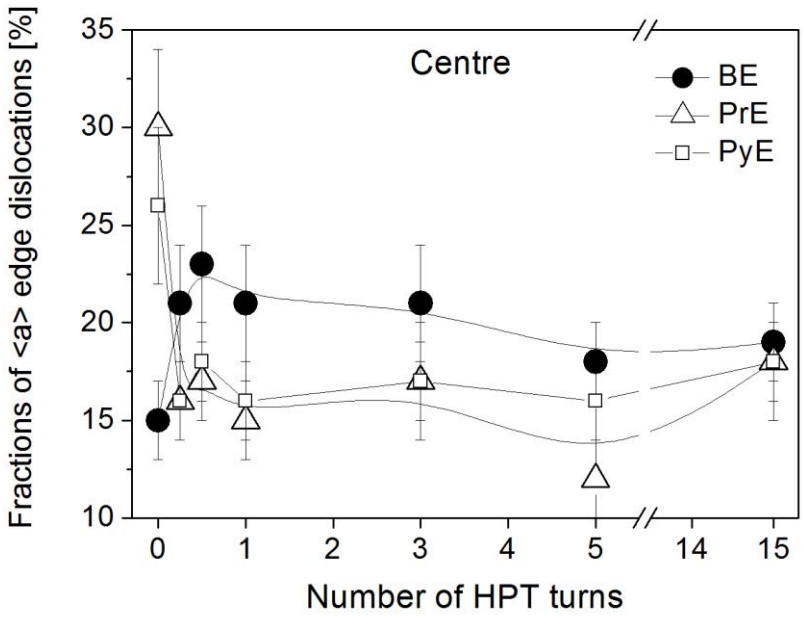

Figure 5.34: The relative fractions of basal (BE), prismatic (PrE) and pyramidal (PyE) <a>-type edge dislocations versus the number of turns for the centre of the HPT processed disks.

5.2.4 Microstructure

Microstructure of the materials after SPD cannot be often observed by light microscopy because of their very small grain sizes. EBSD is usually much better and suitable method in this case. However, even EBSD has some limitation in resolution or some "more local" method could be required for microstructure observations. TEM is a well-known technique which usually solves the problem. ACOM-TEM is very sophisticated method, alternative to EBSD, which enables to study extremely UFG materials. We used this technique for microstructure observations of the most deformed parts of HPT specimens. Disks of the AZ31 processed by HPT could be divided into three parts: centre, middle and periphery, see Fig. 5.35.

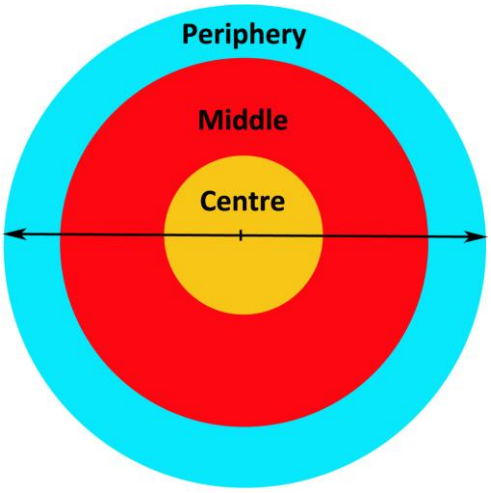

Figure 5.35: Schematic illustration of three different parts of the disks processed by HPT.

Results from the EBSD and ACOM-TEM measurements of the samples after 1, 5 and 15 turns of HPT are shown in Figs. 5.36 – 5.43. Figs. 5.36 and 5.37 show deformed microstructure of the central and middle parts of the specimen after 1 turn studied by EBSD. The areas investigated by EBSD could be relatively big – in our case it was the area 100 × 100 μm. The step size of these measurements was 100 nm. Fig. 5.36 displays heavily deformed microstructure of the central part of the specimen with a lot of multiple twinning. Microstructure of the middle part of the sample after 1 HPT rotation, shown in Fig. 5.37, consists of several large elongated grains with no twins and a lot of new grains of the average size of ~ 1 μm.

The same middle part of this specimen was studied using ACOM-TEM and the typical results are displayed in Fig. 5.38. Measurements were done with step size 20 nm, which is five times smaller than the step size of the EBSD measurements. ACOM-TEM measurements confirmed heterogeneous microstructure with large elongated grains and a lot of small grains. Microstructure of the peripheral part (see Fig. 5.39) is homogeneous with very small grains only (~ 100 – 300 nm).

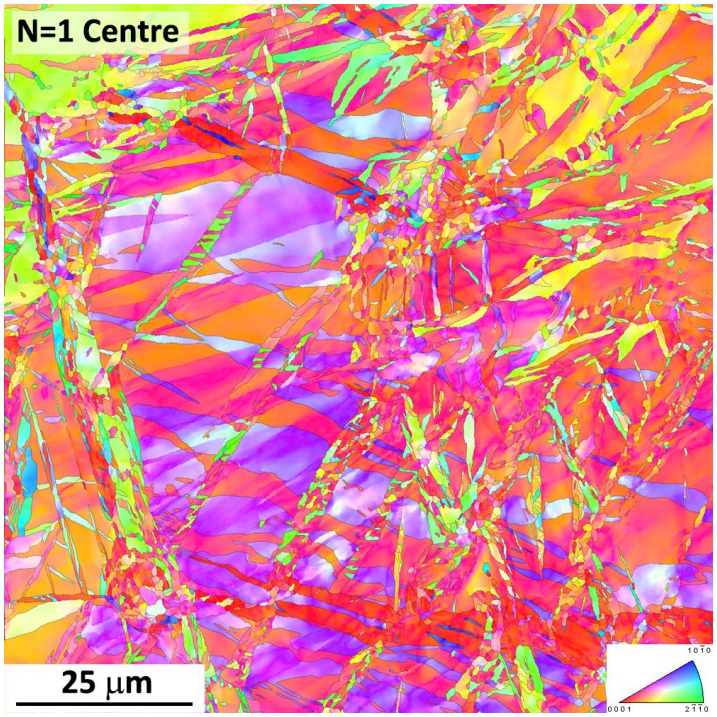

Figure 5.36: Microstructure of the central part of the sample AZ31 after 1 turn of HPT (studied by EBSD).

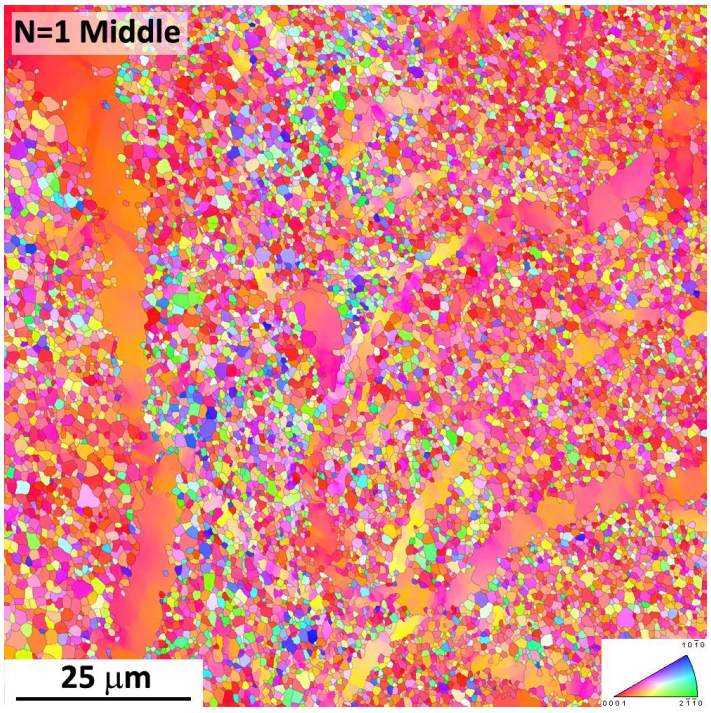

Figure 5.37: Microstructure of the middle part of the sample AZ31 after 1 turn of HPT (studied by EBSD).

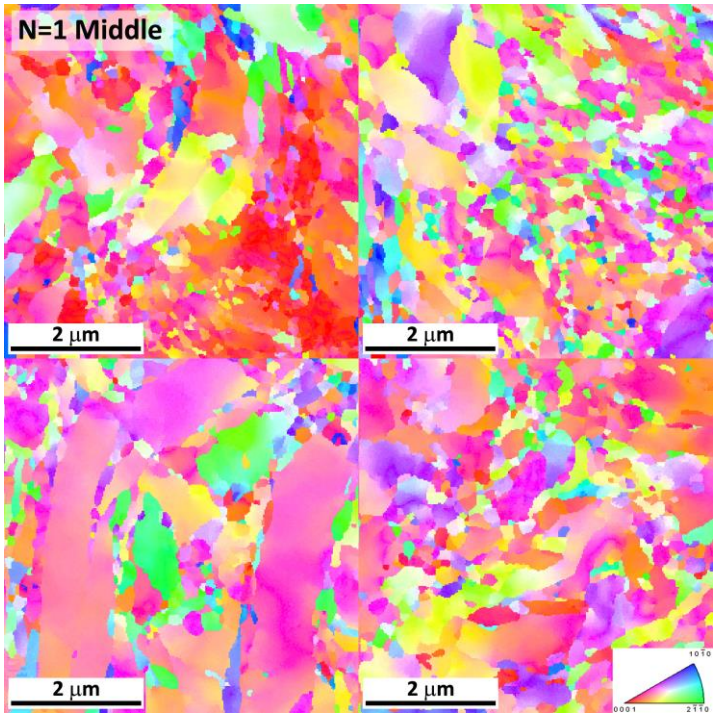

Figure 5.38: Microstructure of the middle part of the sample AZ31 after 1 turn of HPT (ACOM-TEM).

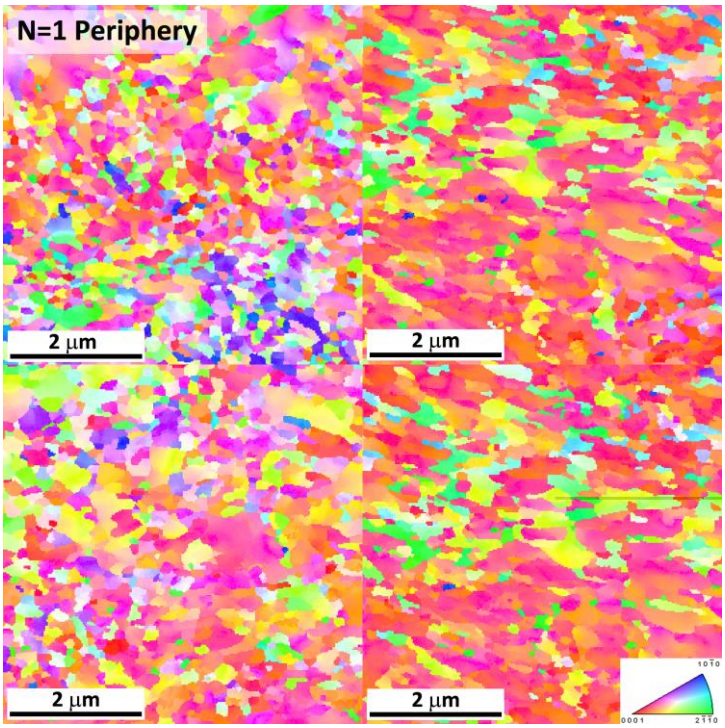

Figure 5.39: Microstructure of the peripheral part of the sample AZ31 after 1 turn of HPT (ACOM-TEM).

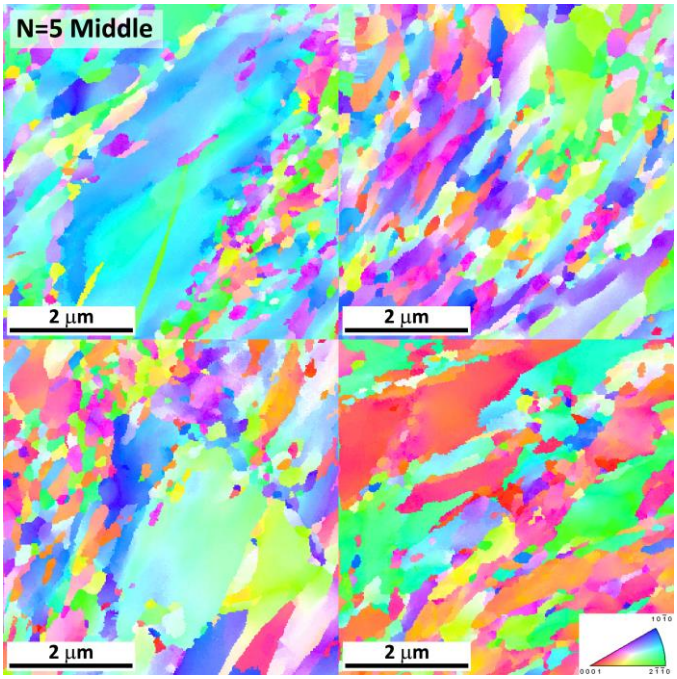

Figure 5.40: Microstructure of the middle part of the sample AZ31 after 5 turns of HPT (ACOM-TEM).

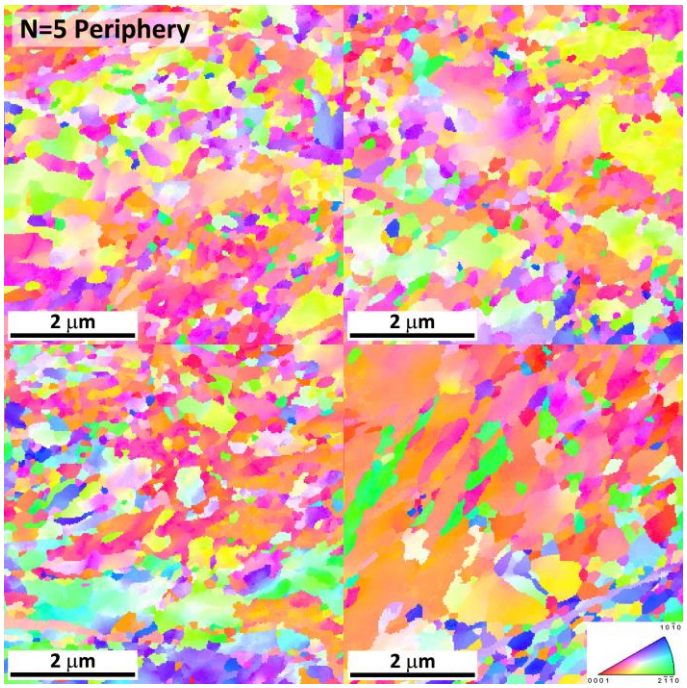

Figure 5.41: Microstructure of the peripheral part of the sample AZ31 after 5 turns of HPT (ACOM-TEM).

The sample after 5 turns of HPT was investigated using ACOM-TEM in the middle and peripheral part of the disk. Microstructure of the middle part (cf. Fig. 5.40) is comparable with the middle part of the sample after 1 HPT rotation – consists of large elongated deformed grains and a lot of small grains surrounding the bigger ones. Microstructure of the peripheral part of the disk after 5 HPT turns, shown in Fig. 5.41, is composed mainly of very small grains. However, few remaining grains with the size of several microns could be still observed in the peripheral part. The ACOM-TEM is very local method where the relatively small part of a thin foil could be investigated. Thus, the statistics of measurements of heterogeneous microstructure like that is not sufficient. Preparation and investigation of several more TEM foils should improve the statistics and solve this problem.

Figs. 5.42 and 5.43 display microstructure of the middle and peripheral part of the disk after 15 HPT rotations, respectively. Microstructure of both parts is more homogeneous than the microstructure of the same parts of the disk after 5 HPT turns. The grain size distributions of extremely UFG microstructure of the peripheral parts of the disks after 1 and 15 HPT rotations (see Fig. 5.44) show that about 60 and nearly 70% of grains, respectively, have a diameter of 100 – 200 nm.

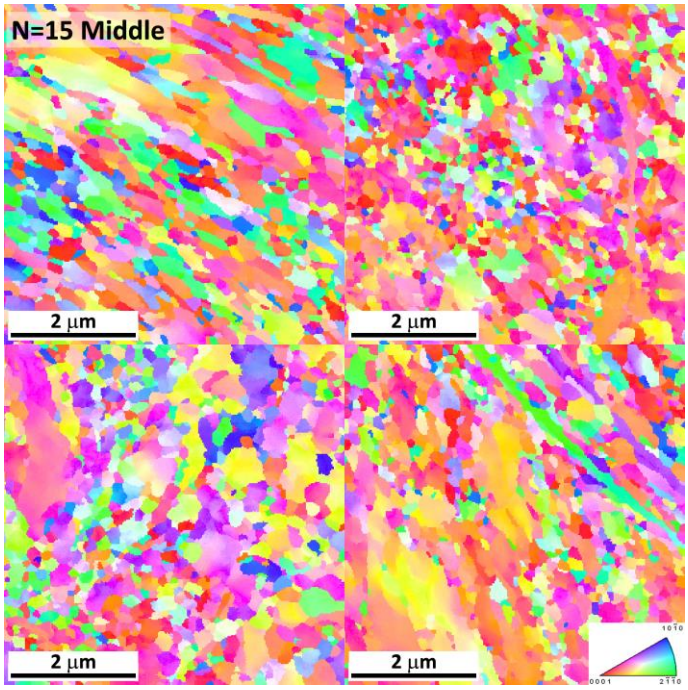

Figure 5.42: Microstructure of the middle part of the sample AZ31 after 15 turns of HPT (ACOM-TEM).

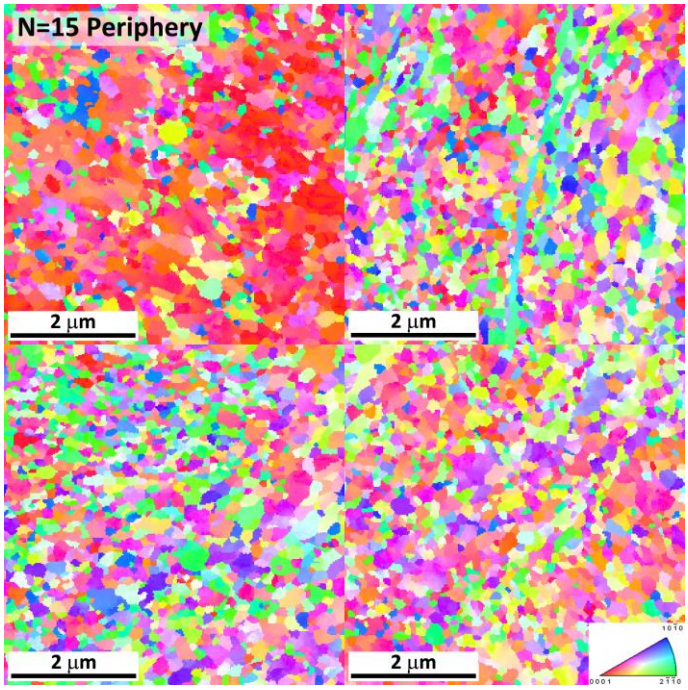

Figure 5.43: Microstructure of the peripheral part of the sample AZ31 after 15 turns of HPT (ACOM-TEM).

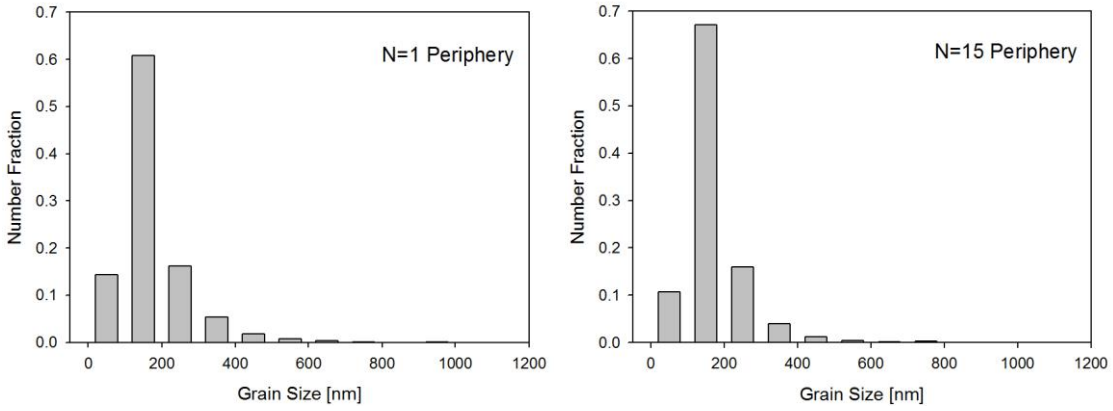

a) **b)**

Figure 5.44: Grain size distribution of the peripheral part of the disk after 1 (a) and 15 (b) rotations of HPT.

6 Discussion

In the previous chapter the results of the detail experimental characterization of mechanical properties, microstructure and lattice defect evolution with strain imposed to the material by two most popular techniques of SPD (ECAP and HPT) obtained by many standard and enhanced experimental techniques were presented. In this chapter I have selected several topics which I consider to be important both from the experimental, scientific and fundamental viewpoint and some of them are currently subject of numerous discussions in the SPD scientific community. This list is far from being complete. The detail discussion of other topics may be also found in scientific papers, reviewed conference proceedings, etc., whose list may be found in the attached list of my publications.

6.1 Comparison of dislocation density of EX-ECAP samples evaluated by PAS and XRD

Both experimental techniques revealed relatively high number of dislocations in all specimens. The dislocation density ρ_D was found to increase up to 2 ECAP passes followed by a continuous decline for higher strains; cf. Fig. 5.3 (PAS) and the Tab. 5.1 (XRD). Systematically higher absolute values of ρ_D (5–6 times) were obtained by XRD in all specimens. The reason is probably threefold:

First, both techniques employed theoretical models for the calculation of ρ_D. In case of PAS, it was the STM [125] which relies on the value of positron trapping rate ν_D (see Eq. (5.1)). This value cannot be obtained experimentally and must be calculated from first principles and in metals falls within a certain range of values. The selection of the exact value was commented in the section "5.1.2 Dislocation density studied by PAS". The X-ray line profile analysis is also based on a microstructural model incorporated in the CMWP evaluation procedure [113].

Second, the signal obtained by both techniques yields information about the microstructure of different zones of the specimen. X-ray signal comes mostly from areas below the surface of the specimen while PAS signal from the bulk.

Third, both techniques employ numerical processing of experimental data and the results inevitably contain some error.

The reason of the difference in ρ_D obtained by both techniques is rather complex and its clarification requires further systematic studies. Let us treat the problem in relative units as there are the relative changes of ρ_D which should be

independent of the technique, provided the evaluation is right. It is reasonable to take the specimen with the highest value of ρ_D as the reference, in our case the specimen after 2 ECAP passes, and to determine relative changes of ρ_D with respect to the density $\rho_{D,max}$ in this specimen. The result is shown in Fig. 6.1 where the relative change $\rho_D/\rho_{D,max}$ is displayed as a function of the number of passes (strain). Excellent match of both curves corresponding to relative changes of dislocation density determined by PAS and XRD is clearly seen and confirms our assumption.

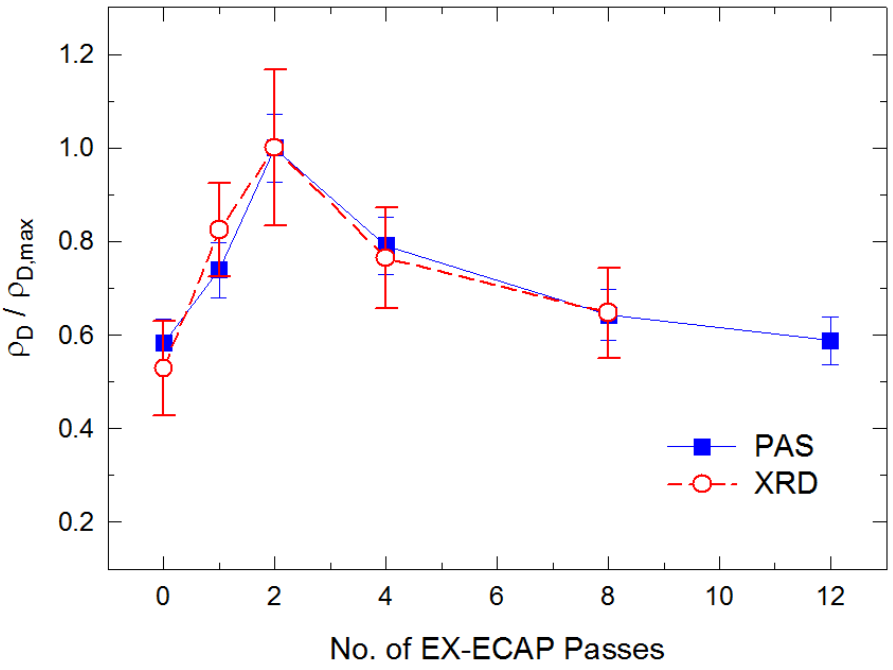

Figure 6.1: The evolution of relative dislocation density in EX-ECAPed specimens determined by PAS and XRD.

The course of this "master curve" describes unambiguously the evolution of dislocation density with strain during ECAP pressing. Significant increase of dislocation density with strain occurs during the first two ECAP passes. Almost double value of ρ_D was found in the specimen after 2 passes than in the extruded material. With increasing number of passes the dislocation density decreased and in the specimen after 12 passes it reached the value comparable with the extruded specimen.

The similar non-monotonous dependence of dislocation density with strain was also observed in other magnesium alloys [124] and was explained by dynamic recovery processes operating at higher strains. However, in other magnesium alloys, e.g., in AZ91, the monotonous increase of the dislocation density with strain was found [136]. In this case, a high volume fraction of discontinuous $Mg_{17}Al_{12}$ precipitates having a rod-like shape were present in the alloy. During ECAP pressing

these particles were continuously broken into smaller parts and their relatively homogeneous dispersion in the matrix contributed to further strengthening of the alloy due to increasing density of dislocations. These precipitates were also found in AZ31 alloy by XRD. However, their volume fraction was significantly lower and softening processes by rearrangement and recovery of dislocations at higher strains prevailed in this alloy. All these results are published in our paper [118].

6.2 Correlation of mechanical properties of EX-ECAP samples with microstructure evolution

Mechanical properties of UFG AZ31 processed by EX-ECAP were investigated by microhardness measurements. In Fig. 5.1 the dependence of the Vickers microhardness on the number of EX-ECAP passes is displayed. There is an obvious correlation between mechanical properties and the dislocation density evolution, cf. Figs. 5.1 and 5.3. Both *HV0.1* and ρ_D first increase with increasing strain up to 2 passes of EX-ECAP where ρ_D reaches the maximum. Vickers microhardness reaches its maximum value after 4 EX-ECAP. Then *HV0.1* and ρ_D decrease continuously with increasing strain.

The texture changes caused by extrusion and ECAP process were also reported to have a crucial influence on the mechanical properties. As it has been reported in our previous work [129], the initial extruded bars exhibit a strong basal texture, i.e., most grains have their crystallographic c-axis perpendicular to the extrusion direction. This orientation relation makes the {10.2} twinning difficult to activate, which belongs to the one of the most important deformation mechanism in magnesium alloys [137]. The first and second pressing reorients the grains to twinning-proper direction. Since the {10.2} twinning causes hardening [137] and contributes to the strain accommodation [138], an increase in both strength and ductility is observed. The texture emerging after the fourth pass is again unsuitable for twinning [139], thus the plastic deformation is realized mostly by dislocation slip and a negative Hall–Petch relation is observed. The softening for higher passes is caused by prevailing impact of texture weakening over the strengthening effect of grain refinement [140]. Furthermore the dislocation density decreases with increasing number of passes, therefore the number of dislocation-type obstacles also decreases.

Our results indicate therefore that the influence of microstructure evolution during ECAP on mechanical properties is rather complex and may be explained both by dislocation structure and the texture development. Strengthening due to grain

refinement plays an important role only in early stages of pressing ($\varepsilon \leq 2$). This investigation was also published in our paper [118].

6.3 Thermal stability

6.3.1 Correlation of various properties of annealed EX-ECAP samples

It follows from microhardness measurements (Fig. 5.9) that UFG microstructure of AZ31 alloy is stable up to 170 °C. After annealing at temperatures higher than 190 °C, a sharp drop of microhardness occurred. A detailed inspection of the microhradness-temperature plot indicates a two-step character of the microhardness decline. In the lower annealing temperature range (170 – 210 °C) the decline is much sharper while for higher annealing temperatures ($T > 210$ °C) the slope of the curve is significantly lower. This two-step character of the curve suggests a change of the mechanism controlling the degradation of mechanical properties.

The strength and hardness of severely deformed ultrafine-grained material are affected mainly by the dislocation density [141] and the grain size according to the Hall-Petch relation [17, 18]. Therefore the grain coarsening and the annihilation of dislocations during annealing are expected to control the material strength and hardness.

Fig. 5.18 showing the grain sizes evolution and Fig. 5.20 showing the dislocation density evolution with annealing temperature must be simultaneously inspected. In the low temperature region of the microhardness drop ($T \approx 170$ – 210 °C) the grain growth is negligible, whereas the dislocation density gradually declines indicating a recovery of dislocation structure. Most probably rearrangement and mutual annihilation of dislocations with opposite signs take place during annealing in this temperature range. As seen in Fig. 5.12 the fine grain structure becomes unstable and significant grain growth is observed at temperatures $T > 210$ °C. In this temperature range, the dislocation density is very low, falling below the detection limit of PAS ($\rho_D \approx 10^{12}$ m^{-2}) at $T \approx 300$ °C.

From microstructure observation (EBSD) and lattice defect density determination (PAS) one can conclude that in the lower annealing temperature region ($T \approx 180$ – 210 °C) it is mostly the annihilation of dislocations which causes the drop of microhardness. At higher temperatures ($T > 210$ °C), probably the grain growth influences significantly the hardness of investigated material.

6.3.2 Grain growth analysis

6.3.2.1 The activation energy of grain growth

The grain growth mechanism during static annealing can be determined from calculated activation energy for grain growth. For this analysis we can use the general equation for the grain growth

$$d^n - d_0^n = kt, \tag{6.1}$$

where d is the grain size at given annealing time, d_0 is the initial grain size, n is the grain growth exponent, t is the annealing time and k is a temperature-dependent constant which can be described by Arrhenius equation

$$\mathrm{k} = \mathrm{k}_0 \exp\left(-\frac{\mathrm{Q}}{\mathrm{RT}}\right), \tag{6.2}$$

where k_0 is a constant, Q is the activation energy for grain growth, R is the gas constant and T is the absolute temperature.

The value of the stress exponent n is of primary importance. In the ideal case (infinite crystal with no defects), the grain growth exponent n should be equal to 2. However, very often higher values of n are found and attributed to various factors affecting grain growth kinetics, such as the free surface effect, impurity-drag, texture, dislocation substructure and microstructure heterogeneities [142]. Previous studies [143–145] reported a value of n in the range from 2 to 8 for various magnesium alloys and magnesium-based composites. Higher values of n ($n \geq 5$) were observed mainly in ultrafine-grained magnesium materials produced by mechanical alloying [144, 145]. The value of grain growth exponent n observed in ultrafine-grained magnesium alloy AZ31 produced by various techniques of severe plastic deformation ranges between 2 and 4 [143, 146, 147]. The AZ31 alloy processed by the most similar conditions (ECAP without previous hot extrusion, where the average grain size after 4 passes was equal to 2.5 μm) was studied by Kim et al. [143, 148]. The grain growth exponent n used in their calculations was equal to 2. We use the same value of n, which will allow us to make comparison with Kim's and other authors' works.

Substituting Eq. (6.2) into (6.1) one can determine the activation energy Q as the slope of the dependence of $ln(d^2\text{-}d_0^2)$ on T^{-1} which is shown in Fig. 6.2. Three temperature ranges with different Q values can be distinguished. The calculated

values of activation energy for grain growth are 115, 33 and 164 kJ/mol in the temperature ranges 170-210 °C, 210-400 °C and 400-500 °C, respectively. These three temperature ranges with different Q values were observed in other fine-grained AZ31 alloys in various conditions and the respective temperature ranges are very similar to our results [143, 149].

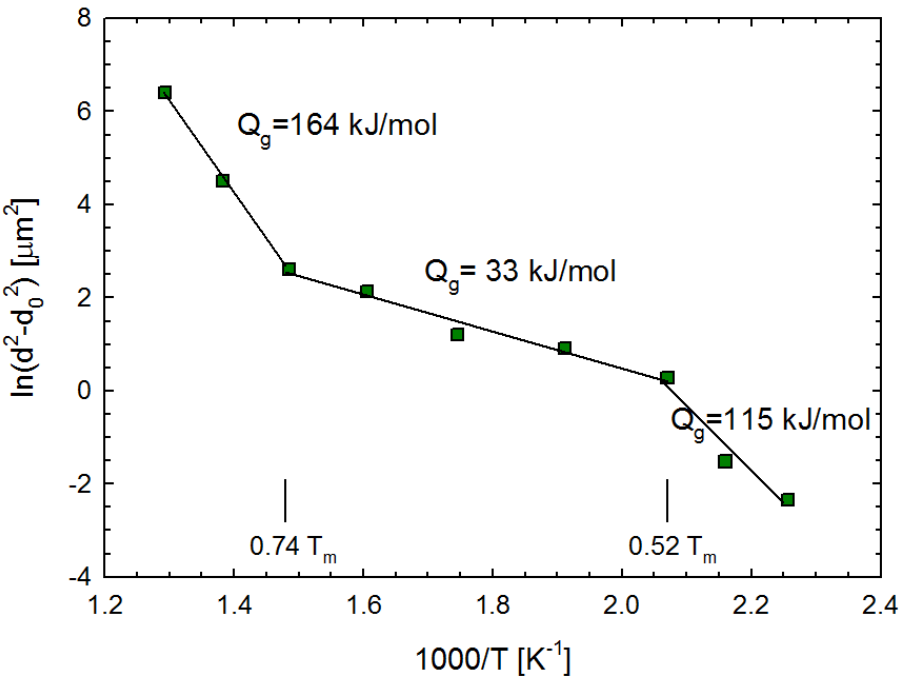

Figure 6.2: Plot of $ln(d^2-d_0^2)$ vs. T^{-1} for the estimation of the activation energy for grain growth of the EX-ECAP magnesium alloy AZ31.

In the low temperature range (T < 210 °C), the activation energy is relatively high (115 kJ/mol) - higher than the activation energy for grain boundary diffusion in pure magnesium (92 kJ/mol [133]). This result is consistent with a well-known fact that activation energy of alloys should be higher than activation energy of pure metals. In this temperature range, the dislocation density within the grains decreases with increasing temperature but it remains relatively high.

In the high temperature range (T > 400 °C), the activation energy Q is equal to 164 kJ/mol, which is higher than lattice self-diffusion in pure magnesium (135 kJ/mol [133]). In AZ31 the lattice self-diffusion is activated and grain growth is enhanced leading to fully-recrystallized structure.

In the intermediate temperature range, the value of Q is exceptionally low. Similarly low value of Q was reported by Wang el al. [150] in the ECAPed Al-Mg alloy annealed at the temperatures $T \leq 275$ °C. The authors attribute the

exceptionally low value of Q to the non-recrystallized microstructure with a certain fraction of non-equilibrium grain boundaries. This conclusion is consistent with the concept of reduced activation energy for grain boundary diffusion in ultrafine-grained materials produced by severe plastic deformation caused by the ability of the non-equilibrium grain boundaries to provide enhanced atomic mobility [151, 152]. The AZ31 alloy after extrusion and 1 pass of ECAP contains a significant number of non-equilibrium grain boundaries. However, the fraction of non-equilibrium grain boundaries decreases with increasing number of ECAP passes so that nearly no such grain boundaries are observed in more deformed AZ31 alloy (see our previous paper [129]). A better explanation of this exceptionally low activation energy in the intermediate temperature range is provided by Kim and Kim [143] – they claim that the value of Q in this temperature range is meaningless. This can occur when k_0 in Eq. (6.3) varies with temperature in the intermediate temperature range.

The dislocation density decreases very fast with increasing annealing temperature and the dislocation density gets below the limit of PAS resolution in the high temperature range. High dislocation density is known to increase the diffusivity of material due to so-called pipe diffusion. It is therefore argued in accordance with Kim and Kim [143] that k_0 declines with increasing temperature due to decreasing dislocation density causing the decrease in diffusivity. The assumption of constant k_0 is invalid in this case and leads to a significant underestimation of the activation energy.

6.3.2.2 Hall-Petch relation

EBSD analysis allows us to determine the validity of Hall-Petch (HP) relation for isochronally annealed UFG specimens in the temperature range up to 400 °C. For this analysis the HP relation yields

$$HV = H_0 + K_H d^{-\frac{1}{2}}, \tag{6.3}$$

where H_0 and K_H are material constants and HV is the measured value of the microhardness.

The results of HV and d obtained from measured values shown in Figs. 5.9 and 5.18, respectively, and summarized in Tab. 5.3 are plotted in Fig. 6.3.

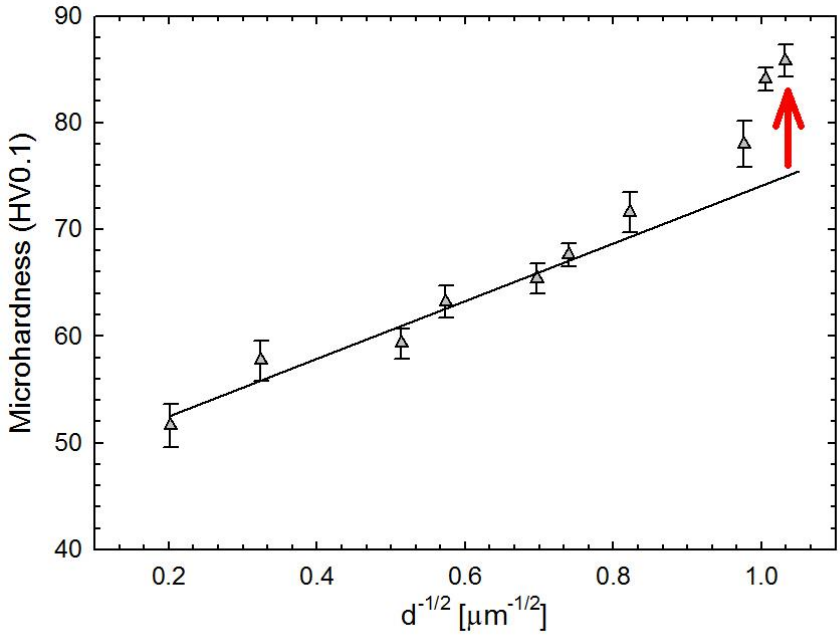

Figure 6.3: Hall-Petch relationship for the isochronally annealed EX-ECAP AZ31 alloy based on *HV0.1* microhardness data.

The constants H_0 and K_H may be calculated from the parameters of a straight line depicted in Fig. 6.3. The best linear fit was applied only to data corresponding to higher annealing temperatures (from 250 to 500 °C). In this temperature range, only the grain size affects the material hardness as the dislocation density is low. At low temperatures, both grain size and dislocation density contribute to strengthening and the linear fit of microhardness data fails. Data for low annealing temperatures (i.e. high dislocation density conditions) lie clearly above the Hall-Petch fit (marked by the red arrow).

The calculated material constants from the high temperature fit of *HV* vs. $d^{-1/2}$ are: $H_0 = 47 \pm 2$ and $K_H = 27 \pm 3$ μm$^{1/2}$. These values are partly comparable to those reported on ECAPed Al alloys with H_0 = 35-47 and K_H = 35-50 μm$^{1/2}$ [153] but different from those reported on the only ECAPed AZ31 alloy by Kim and Kim [143] (H_0 = 38, K_H = 42 μm$^{1/2}$). However, these authors calculated these constants from the linear fit of the whole temperature range and did not take the changes of dislocation densities into consideration. As a consequence, their values of H_0 and K_H are underestimated and overestimated, respectively, in comparison with our calculated constants. Our value of the constant H_0 is closer to the microhardness value of the AZ31 in annealed condition (*HV0.1* = 58 ± 3, see our previous paper [154]) in comparison with the value of H_0 calculated by Kim and Kim [143]. This

thermal stability investigations and grain growth analysis were published in our recent paper [130].

6.4 Correlation of microstructure and defect structure after HPT

The maximum dislocation density and minimum crystallite size were about 6×10^{14} m^{-2} and 70 nm, respectively. Additionally, considerable difference between the crystallite size and the dislocation structure at the centre and the periphery was not detected despite the various imposed strain values. These observations suggest an early saturation of the microstructural parameters with increasing strain during HPT processing at room temperature. Note that the crystallite size obtained by XLPA is much smaller than the grain size determined by EBSD or ACOM-TEM. This observation is in accordance with former studies and can be explained by the fact that the crystallite size determined by XRD (XLPA) as the coherently scattering domain corresponds rather to the subgrain size than to the grain size in severely deformed microstructures. Therefore, there is no correlation between the crystallite and grain sizes, but rather they complementary describe the hierarchical nature of the microstructures obtained by SPD.

Comparing of EBSD and/or ACOM-TEM with XLPA results allows us to conclude that the saturation of the subgrain size and the dislocation density occurred earlier (at lower strains) than reaching the minimum grain size during HPT. Note that the saturation values of dislocation density and crystallite size in the present experiments were higher and lower, respectively, than the values obtained in EX-ECAP processing at 180 °C (1.4×10^{14} m^{-2} and 120 nm [155]). This can be explained by the much lower temperature and the higher pressure of HPT processing than in ECAP) since both retards the annihilation of dislocations. Additionally, it has been shown that $Mg_{17}Al_{12}$ secondary phase was formed in the Mg–3%Al–1%Zn alloy during ECAP at 180 °C while the Al and Zn alloying elements remained in solid solution during HPT experiments at room temperature [155].

6.5 Equivalent strains imposed by EX-ECAP and HPT

There are many ways how to compare the mechanical properties, microstructure and defect density obtained by different techniques of SPD. Usually authors compare the "effectiveness" of various techniques by comparing the respective properties at ultimate conditions, which in case of ECAP corresponds to

the maximum number of passes while in HPT to the maximum number of turns. Such comparison reflects more the experimental conditions of each author rather than some physical reason.

As the evolution of microstructure and mechanical properties is controlled by equivalent strain imposed to the material during SPD, one of possible ways how to make a more "objective" comparison is to take conditions of the same equivalent strain obtained by different techniques of SPD and to compare the respective microstructure, defect structure and mechanical properties of specimens processed by these techniques. In our case we will compare the conditions of the same equivalent strain obtained by EX-ECAP and by HPT.

The effective strain (obtained from the FEM results) imposed by HPT increases at the centre after half a turn, while the torsion (shear, von Mises) strain given by Eq. (2.5) is zero. The strain obtained by the FEM simulations at the centre, which is higher than the theoretical value (Eq. (2.5)), can be explained by the compressive strain in HPT and the finite mesh size in the FEM [75, 77]. The FEM simulation and torsion theory results are in a good agreement in the regions near the middle of the disk (r = 4 - 6 mm) after a single turn. However, at the periphery region (r = 8 - 10 mm), the results of the FEM simulations deviate from the theoretical values because of "dead metal zone" phenomenon [77]. Therefore, the strain of middle region of the disk after HPT is well-fitted according to the theoretical equation Eq. (2.5).

The equivalent strain imposed by EX-ECAP could be calculated from the Eq. (1) in Chen et al. [156] and Eq. (6) in Valiev et al. [59]

$$\varepsilon_N = \ln R_E + \frac{2N}{\sqrt{3}} \cot \varphi \,, \tag{6.4}$$

where R_E is the extrusion ratio (equal to 22 in our case) and $\varphi = {}^{\Phi}/_{2}$ (equal to 45° in our case).

The plots of equivalent strains imposed by EX-ECAP and HPT are displayed in Fig. 6.4. Intersections of vertical lines (EX-ECAP) with "HPT" curves correspond to zones of the same equivalent strain in specimens processed by EX-ECAP and HPT which in HPT specimens are characterized by the distance r from the centre of the disk.

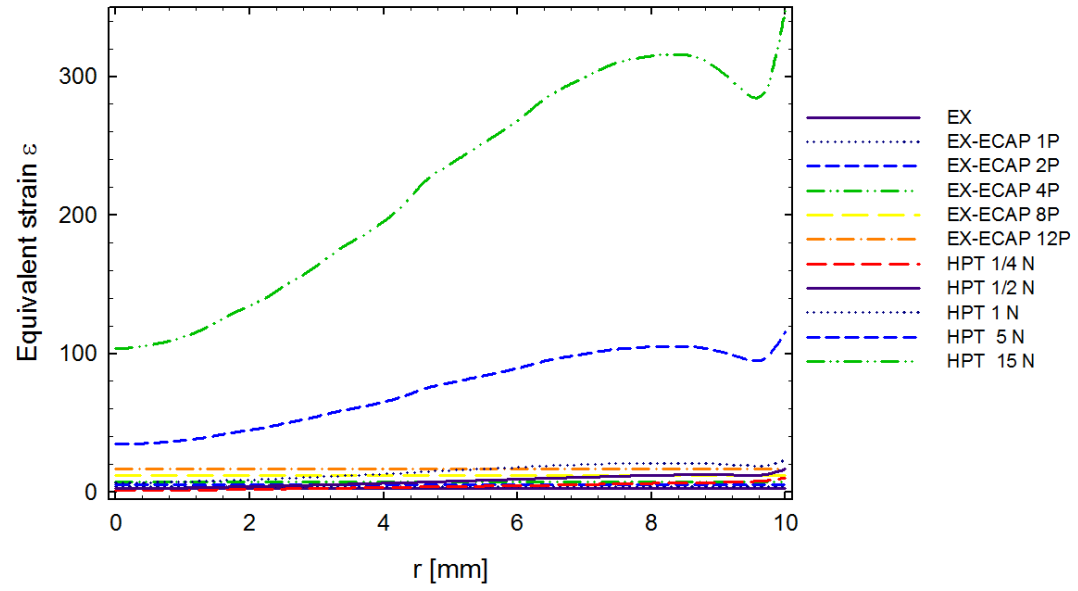

a)

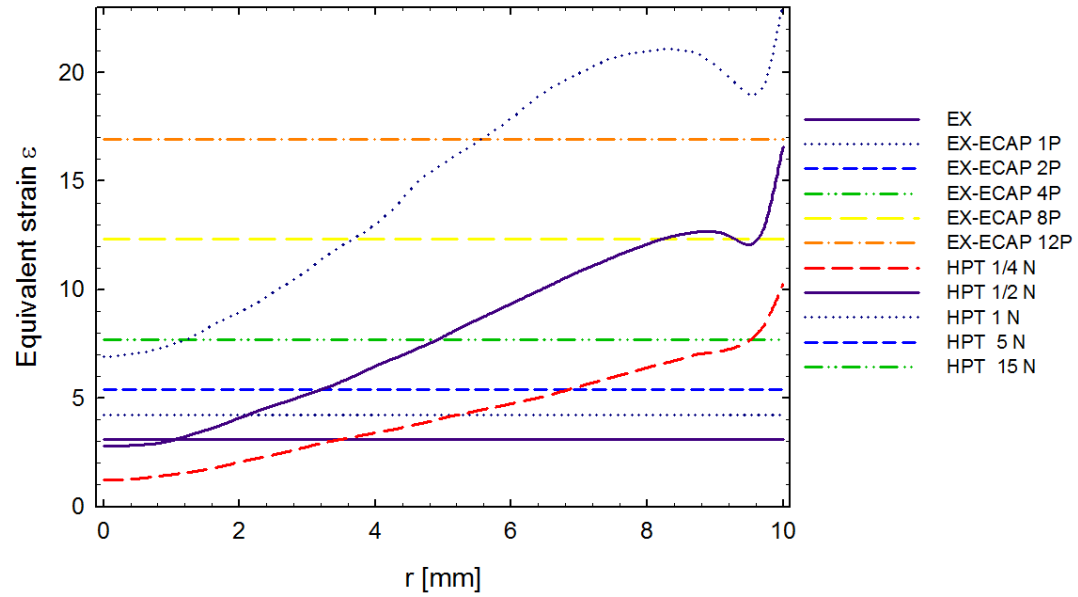

b)

Figure 6.4: Equivalent strains imposed by HPT and EX-ECAP (calculated from FEM simulations and Eq. (6.4)) shown in the full scale (a) and for small strains to highlight the details (b).

The respective distances *r* corresponding to the intersections of the HPT and EX-ECAP curves from Fig. 6.4 (b) are shown in Tab. 6.1. Note, that due to the inhomogeneous distribution of strain in specimens processed by HPT, one can find in

each HPT specimen several zones corresponding to the same equivalent strain in several EX-ECAP specimens (the rows of the table). On the other hand, to the strain imposed by EX-ECAP in individual specimens several zones of the same equivalent strain can be found in HPT specimens (the columns of the table).

***r* [mm]**	EX	1P	2P	4P	8P	12P
¼ N HPT	3 – 4	5	7	9		
½ N HPT	Centre	2	3	5	8	
1 N HPT				1	3 - 4	5 – 6

Table 6.1: Zones in HPT processed disks (characterized by the distance *r* from the disk centre) corresponding to the same equivalent strain imposed to billets by EX-ECAP.

6.5.1 Comparison of microhardness and microstructure

Microhardness values obtained in equivalent strain zones from the Tab. 6.1 are summarized in Tab. 6.2. Microhardness values measured in HPT samples are significantly higher than the *HV* values in EX-ECAP samples (given in the first row of Tab. 6.2). This fact is probably caused by the different microstructure and dislocation density of the samples after HPT and EX-ECAP.

HV 0.1	EX	1P	2P	4P	8P	12P
	70	80	82	85	82	79
¼ N HPT	95 – 97	97	104	108		
½ N HPT	87	93	97	103	107	
1 N HPT				85	100	102 - 109

Table 6.2: Microhardness *HV0.1* of the specimens after EX-ECAP and zones of the samples after HPT with the same equivalent strain.

Microstructure of the extruded and 1P EX-ECAP specimens is bimodal consisting of large (> 10 μm) and small (~ 1 μm) grains. Microstructure of the

specimens becomes more homogeneous and finer with increasing number of ECAP passes. Average grain size of the 4P, 8P and 12P EX-ECAP specimens is approximately equal to 1 μm [129].

Microstructure observations of the samples after HPT by EBSD and ACOM-TEM indicate that the initial coarse-grained microstructure transforms into inhomogeneous grain structure which becomes finer and more homogeneous with increasing number of HPT turns. The average grain sizes are reduced to ~100 nm in our case. These results are in good agreement with the similar observations of hexagonal Zr alloy after room temperature HPT reported by Wang et al. [157]. They found an interesting structural evolution that is believed to be unique to HCP materials and produces a structure with an inhomogeneous grain size distribution that later transforms into a uniform nanocrystalline structure with further HPT. Wang et al. claim that the inhomogeneous grain structure is clearly a transitional structure during grain refinement. With further deformation, grain rotations occurred and the internal inter-grain stresses built up, both of which favour the activation of dislocation slip systems [157].

6.5.2 Comparison of defect structure evolution

The density of dislocations is the second principal factor influencing the microhardness values. Dislocation densities ρ_D shown in Tab. 6.3 were measured approximately in the same areas as the microhardness. Dislocation densities are higher in zones of the same equivalent strain of HPT disks than in ECAP billets. Higher values of dislocation densities in HPT specimens are probably caused by several reasons.

$\rho_D[10^{13}\ m^{-2}]$	EX	1P	2P	4P	8P	12P
	1.6	2.0	2.7	2.2	1.8	1.6
¼ N HPT	2.1	2.0	3.2	-		
½ N HPT	2.8	2.3	2.0	2.2	5.0	
1 N HPT				4.3	3.6	3.5

Table 6.3: Dislocation density ρ_D of the specimens after EX-ECAP and zones of the samples after HPT with the same equivalent strain.

The first factor is the different processing temperature during HPT and EX-ECAP. It is well-known that processing by ECAP had to be performed at elevated temperatures (180 °C in our case) as the hexagonal structure does not offer at normal conditions five independent slip systems which are required for uniform deformation according to von-Mises criterion [10]. On the other hand, other slip systems operate not only at elevated temperatures but also at high stresses [158]. HPT was applied at room temperature (which is equal to homologous temperature 0.32) because the hydrostatic pressure was high enough (2.5 GPa) to enable uniform deformation. However, the deformation temperature in HPT die may be even higher. The experimental setup did not allow measuring the temperature of the specimen during HPT.

The other reason of higher dislocation densities in zones with the same equivalent strain in HPT specimens is the fact, that high applied pressure increases the stresses which can impede the cross-slip of screw dislocations depending on their orientation relative to the line and Burgers vectors [159]. Stacking fault energy (SFE) of pure magnesium is relatively high: 125 mJ/m^2 [160]. The addition of alloying elements significantly lowers the SFE due to the pinning effect reducing the SFE to 27.8 mJ/m^2 in AZ31 [132]. The degree of dissociation of dislocations is therefore not so high to hinder absolutely the recovery or recrystallization but not so low to make these processes easier.

7 Conclusions

In the present work, an AZ31 magnesium alloy was subjected to two severe plastic deformation (SPD) techniques: hot extrusion followed by equal-channel angular pressing (EX-ECAP) and high pressure torsion (HPT). Complex microstructural characterization was carried out using a wide range of complementary methods.

The main results can be summarized as follows:

- EX-ECAP and HPT techniques were successfully applied to refine the microstructure of the studied alloy down to the sub-micrometer level with average grain sizes equal to approximately 900 and 200 nm, respectively.

- Heavily deformed and UFG microstructure evolution was investigated in detail using various methods: EBSD, TEM and ACOM-TEM. Microstructure of the EX-ECAPed samples is homogeneous along its transverse cross-section. Furthermore, the microstructure becomes relatively homogeneous with high fraction of high-angle grain boundaries after 4 and more passes of EX-ECAP. Microstructure of the disks after HPT is strongly dependent on the distance from the centre. High pressure leads to the deformation of original large grains and to the multiple twinning. Additional torsion causes grain refinement that is first observed at the peripheral parts of the disks where the equivalent imposed strain is higher. Increasing number of HPT rotations (and increasing imposed strain in the material) leads to further grain fragmentation and microstructure homogenization in middle and central parts of the disks.

- Lattice defect structure investigations using PAS and XRD suitably broadened the complex research of UFG microstructure. Dislocations proved to be the only measurable lattice defects in specimens deformed by both EX-ECAP and HPT. Dislocation density is another crucial parameter besides the grain size which strongly influences mainly the mechanical properties (e.g. microhardness).

- The equivalent strains imposed by EX-ECAP and HPT were calculated, and the variations in mechanical properties and dislocation density evolution were compared in conditions corresponding to the same equivalent strain imposed by both techniques of SPD. HPT proved to be more effective method of grain refinement of AZ31 alloy resulting in significantly higher values of microhardness and dislocation densities.

- Microstructure stability at elevated temperatures was investigated in the temperature range of 150 – 500 °C. The main objective was to identify the softening processes operating in this temperature range. We can assume that at lower annealing temperatures (≈ 190 °C) the softening manifested by microhardness drop is mainly controlled by dislocation annihilation (proved by PAS). On the other hand, at higher annealing temperatures (≈ 300 °C and higher), grain growth becomes the principal softening mechanism (proved by EBSD). The kinetics of grain growth was described by the kinetic equation $d^2 - d_0^2 = kt$ and the activation energies for grain growth were calculated for three different temperature ranges. It was demonstrated that Vickers microhardness evolution in higher temperatures range (250 °C – 500 °C) can be successfully explained by Hall-Petch relation. In lower temperatures range, the dislocation density plays a significant role and the microhardness is significantly higher than the extrapolated Hall-Petch fit. The effect of dislocations must be taken into account to get reliable estimates of parameters of Hall-Petch relation.

8 Bibliography

[1] OKAMOTO, H. *Desk handbook: phase diagrams for binary alloys*. Materials Park, OH: ASM International, 2000.

[2] AVEDESIAN, M. M. and Hugh BAKER, eds. *Magnesium and magnesium alloys*. Materials Park, OH: ASM International, 1999.

[3] MORDIKE, Barry L. and K. U. KAINER, eds. *Magnesium alloys and their applications*. Frankfurt: Volkswagenwerk, Werkstoff-Informationsgesellschaft, 1998.

[4] MORDIKE, B.L. and T. EBERT. Magnesium: Properties — applications — potential. *Materials Science and Engineering: A*. 2001, vol. 302, no. 1, pp. 37–45.

[5] CAHN, R. W., P. HAASEN and E. J. KRAMER, eds. *Materials science and technology: a comprehensive treatment*. Weinheim: Wiley-VCH, 2005.

[6] GUPTA, M. *Magnesium, magnesium alloys, and magnesium composites*. New York: John Wiley & Sons, 2011.

[7] VRÁTNÁ, J. *Diploma Thesis: Physical Properties of Ultrafine-grained Polycrystals of Magnesium Based Alloys*. 2010

[8] LYON, P., T. WILKS and I. SYED. The influence of alloying elements and heat treatment upon properties of Elektron 21 (EV31A) alloy. In: NEAL R. NEELAMEGGHAM, Howard I. KAPLAN and Bob Ross POWELL, eds. *Magnesium technology 2005: Proceedings of the symposium*. Warrendale, Pa: TMS, 2005, p. 303–308.

[9] GOTTSTEIN, G. *Physical foundations of materials science*. Berlin ; New York: Springer, 2004.

[10] VON MISES, R. Mechanik der plastischen Formänderung von Kristallen. *Zeitschrift für angewande Mathematik und Mechanik*. 1928, no. 8, pp. 161–185.

[11] ILLKOVÁ, K. *Doctoral Thesis: Influence of Solid Solution Elements and Precipitate Formation on the Mechanical Behaviour of Magnesium Alloys*. 2013.

[12] AGNEW, S.R. and Ö. DUYGULU. Plastic anisotropy and the role of non-basal slip in magnesium alloy AZ31B. *International Journal of Plasticity*. 2005, vol. 21, no. 6, Plasticity of Multiphase Materials, pp. 1161–1193.

[13] LOU, X.Y., M. LI, R.K. BOGER, S.R. AGNEW and R.H. WAGONER. Hardening evolution of AZ31B Mg sheet. *International Journal of Plasticity*. 2007, vol. 23, no. 1, pp. 44–86.

[14] KUHLMANN-WILSDORF, D. Theory of plastic deformation: - properties of low energy dislocation structures. *Materials Science and Engineering: A*. 1989, vol. 113, pp. 1–41.

[15] *Strengthening mechanisms of materials, Wikipedia, http://en.wikipedia.org/w/index.php?title=Strengthening_mechanisms_of_materials&oldid=590348116*. 2014.

[16] COTTRELL, A.H. Theory of brittle fracture in steel and similar metals. *Trans. TMS - AIME*. 1958, vol. 212, pp. 192–203.

[17] HALL, E.O. The Deformation and Ageing of Mild Steel: III Discussion of Results. *Proceedings of the Physical Society. Section B*. 1951, vol. 64, no. 9, pp. 747–753.

[18] PETCH, N.J. The cleavage strength of polycrystals. *Journal of the Iron and Steel Institute London*. 1953, vol. 173, pp. 25–28.

[19] CHOKSHI, A.H., A. ROSEN, J. KARCH and H. GLEITER. On the validity of the hall-petch relationship in nanocrystalline materials. *Scripta Metallurgica*. 1989, vol. 23, no. 10, pp. 1679–1683.

[20] SURYANARAYANA, C. The structure and properties of nanocrystalline materials: issues and concerns. *JOM*. 2002, vol. 54, no. 9, pp. 24–27.

[21] SCHIOTZ, J., F. D. DI TOLLA and K. W. JACOBSEN. Softening of nanocrystalline metals at very small grain sizes. *Nature*. 1998, vol. 391, pp. 561–563.

[22] VALIEV, R.Z., Y. ESTRIN, Z. HORITA, T.G. LANGDON, M.J. ZECHETBAUER and Y.T. ZHU. Producing bulk ultrafine-grained materials by severe plastic deformation. *JOM*. 2006, vol. 58, no. 4, pp. 33–39.

[23] HUANG, J.Y., Y.T. ZHU, H. JIANG and T.C. LOWE. Microstructures and dislocation configurations in nanostructured Cu processed by repetitive corrugation and straightening. *Acta Materialia*. 2001, vol. 49, no. 9, pp. 1497–1505.

[24] ESTRIN, Y. and A. VINOGRADOV. Extreme grain refinement by severe plastic deformation: A wealth of challenging science. *Acta Materialia*. 2013, vol. 61, no. 3, pp. 782–817.

[25] LAPOVOK, R., P.F. THOMSON, R. COTTAM and Y. ESTRIN. The effect of grain refinement by warm equal channel angular extrusion on room

temperature twinning in magnesium alloy ZK60. *Journal of Materials Science*. 2005, vol. 40, no. 7, pp. 1699–1708.

[26] ESTRIN, Y., L. S. TÓTH, Y. BRÉCHET and H. S. KIM. Modelling of the evolution of dislocation cell misorientation under severe plastic deformation. *Materials Science Forum*. 2006, vols. 503-504, pp. 675–680.

[27] ZEHETBAUER, M., T. UNGÁR, R. KRAL, A. BORBÉLY, E. SCHAFLER, B. ORTNER, H. AMENITSCH and S. BERNSTORFF. Scanning X-ray diffraction peak profile analysis in deformed Cu-polycrystals by synchrotron radiation. *Acta Materialia*. 1999, vol. 47, no. 3, pp. 1053–1061.

[28] ZHU, Y.T., T.C. LOWE and T.G. LANGDON. Performance and applications of nanostructured materials produced by severe plastic deformation. *Scripta Materialia*. 2004, vol. 51, no. 8, pp. 825–830.

[29] BENJAMIN, J.S. Dispersion strengthened superalloys by mechanical alloying. *Metallurgical Transactions*. 1970, vol. 1, no. 10, pp. 2943–2951.

[30] WITKIN, D.B. and E.J. LAVERNIA. Synthesis and mechanical behavior of nanostructured materials via cryomilling. *Progress in Materials Science*. 2006, vol. 51, no. 1, pp. 1–60.

[31] BIRRINGER, R., H. GLEITER, H.-P. KLEIN and P. MARQUARDT. Nanocrystalline materials an approach to a novel solid structure with gas-like disorder? *Physics Letters A*. 1984, vol. 102, no. 8, pp. 365–369.

[32] ERB, U., A.M. EL-SHERIK, G. PALUMBO and K.T. AUST. Synthesis, structure and properties of electroplated nanocrystalline materials. *Nanostructured Materials*. 1993, vol. 2, no. 4, pp. 383–390.

[33] WANG, J.T. Historic Retrospection and Present Status of Severe Plastic Deformation in China. *Materials Science Forum*. 2006, vols. 503-504, pp. 363–370.

[34] SRINIVASAN, C. Do Damascus swords reveal India's mastery of nanotechnology? *Current Science*. 2007, vol. 92, no. 3, pp. 279–280.

[35] SHERBY, O.D. and J. WADSWORTH. Ancient blacksmiths, the Iron Age, Damascus steels, and modern metallurgy. *Journal of Materials Processing Technology*. 2001, vol. 117, no. 3, pp. 347–353.

[36] BRIDGMAN, P.W. *Studies in large plastic flow and fracture with special emphasis on the effects of hydrostatic pressure.* Metallurgy and metallurgical engineering series. 1952.

[37] LANGDON, T.G. The principles of grain refinement in equal-channel angular pressing. *Materials Science and Engineering: A*. 2007, vol. 462, no. 1-2, pp. 3–11.

[38] ZHILYAEV, A.P. and T.G. LANGDON. Using high-pressure torsion for metal processing: Fundamentals and applications. *Progress in Materials Science*. 2008, vol. 53, no. 6, pp. 893–979.

[39] SAITO, Y., H. UTSUNOMIYA, N. TSUJI and T. SAKAI. Novel ultra-high straining process for bulk materials—development of the accumulative roll-bonding (ARB) process. *Acta Materialia*. 1999, vol. 47, no. 2, pp. 579–583.

[40] THOMAS, W.M., E. D. NICHOLAS, J. C. NEEDHAM, M. G. MURCH, P. TEMPLE-SMITH and C. J. DAWES. Patent No. 9125978.8, UK, 1991.

[41] MISHRA, R.S., M.W. MAHONEY, S.X. MCFADDEN, N.A. MARA and A.K. MUKHERJEE. High strain rate superplasticity in a friction stir processed 7075 Al alloy. *Scripta Materialia*. 1999, vol. 42, no. 2, pp. 163–168.

[42] ZHU, Y.T., T. C. LOWE, H. JIANG and J. HUANG. Patent No. 6197129, USA, 2001.

[43] ZHU, Y.T., H. JIANG, J. HUANG and T.C. LOWE. A new route to bulk nanostructured metals. *Metallurgical and Materials Transactions A*. 2001, vol. 32, no. 6, pp. 1559–1562.

[44] SITDIKOV, O., T. SAKAI, A. GOLOBORODKO, H. MIURA and R. KAIBYSHEV. Effect of Pass Strain on Grain Refinement in 7475 Al Alloy during Hot Multidirectional Forging. *Materials Transactions*. 2004, vol. 45, no. 7, pp. 2232–2238.

[45] ZEHETBAUER, M. and R.Z. VALIEV, eds. Severe Plastic Deformation by Twist Extrusion. In: M. ZEHETBAUER and R.Z. VALIEV, eds. *Nanomaterials by severe plastic deformation: proceedings of the conference "Nanomaterials by Severe Plastic Deformation, NANOSPD2," December 9-13, 2002, Vienna Austria*. Weinheim: Wiley-VCH, 2004, p. 511–516.

[46] RICHERT, J. and M. RICHERT. A New Method for Unlimited Deformation of Metals and Alloys. *Aluminium*. 1986, vol. 62, no. 8, pp. 604–607.

[47] RICHERT, M., Q. LIU and N. HANSEN. Microstructural evolution over a large strain range in aluminium deformed by cyclic-extrusion–compression. *Materials Science and Engineering: A*. 1999, vol. 260, no. 1-2, pp. 275–283.

[48] SEGAL, V.M. Patent No. 575892, USSR, 1977.

[49] SEGAL, V.M., V. I. REZNIKOV, A. E. DROBYSHEVSKIY and V. I. KOPYLOV. Plastic working of metals by simple shears. *Russian Metallurgy*. 1981, vol. 1, pp. 99–105.

[50] LIN, H.K., J.C. HUANG and T.G. LANGDON. Relationship between texture and low temperature superplasticity in an extruded AZ31 Mg alloy

processed by ECAP. *Materials Science and Engineering: A*. 2005, vol. 402, no. 1-2, pp. 250–257.

[51] XU, C., M. FURUKAWA, Z. HORITA and T.G. LANGDON. The evolution of homogeneity and grain refinement during equal-channel angular pressing: A model for grain refinement in ECAP. *Materials Science and Engineering: A*. 2005, vol. 398, no. 1-2, pp. 66–76.

[52] RABKIN, E., I. GUTMAN, M. KAZAKEVICH, E. BUCHMAN and D. GORNI. Correlation between the nanomechanical properties and microstructure of ultrafine-grained copper produced by equal channel angular pressing. *Materials Science and Engineering: A*. 2005, vol. 396, no. 1-2, pp. 11–21.

[53] KRASILNIKOV, N., W. LOJKOWSKI, Z. PAKIELA and R. VALIEV. Tensile strength and ductility of ultra-fine-grained nickel processed by severe plastic deformation. *Materials Science and Engineering: A*. 2005, vol. 397, no. 1-2, pp. 330–337.

[54] LATYSH, V.V., I. P. SEMENOVA, G. H. SALIMGAREEVA, I. V. KANDAROV, Y. T. ZHU, T. C. LOWE and R. Z. VALIEV. Microstructure and Properties of Ti Rods Produced by Multi-Step SPD. *Materials Science Forum*. 2006, vols. 503-504, pp. 763–768.

[55] KIM, H.S., W.S. RYU, M. JANEČEK, S.C. BAIK and Y. ESTRIN. Effect of Equal Channel Angular Pressing on Microstructure and Mechanical Properties of IF Steel. *Advanced Engineering Materials*. 2005, vol. 7, no. 1-2, pp. 43–46.

[56] LI, Y. and T. G. LANGDON. Equal-channel angular pressing of an Al-6061 metal matrix composite. *Journal of Materials Science*. 2000, vol. 35, no. 5, pp. 1201–1204.

[57] RAAB, G.J., R.Z. VALIEV, T.C. LOWE and Y.T. ZHU. Continuous processing of ultrafine grained Al by ECAP–Conform. *Materials Science and Engineering: A*. 2004, vol. 382, no. 1-2, pp. 30–34.

[58] IWAHASHI, Y., J. WANG, Z. HORITA, M. NEMOTO and T.G. LANGDON. Principle of equal-channel angular pressing for the processing of ultra-fine grained materials. *Scripta Materialia*. 1996, vol. 35, no. 2, pp. 143–146.

[59] VALIEV, R.Z. and T.G. LANGDON. Principles of equal-channel angular pressing as a processing tool for grain refinement. *Progress in Materials Science*. 2006, vol. 51, no. 7, pp. 881–981.

[60] FURUNO, K., H. AKAMATSU, K. OH-ISHI, M. FURUKAWA, Z. HORITA and T.G. LANGDON. Microstructural development in equal-

channel angular pressing using a 60° die. *Acta Materialia*. 2004, vol. 52, no. 9, pp. 2497–2507.

[61] HORITA, Z., M. FURUKAWA, M. NEMOTO and T. G. LANGDON. Development of fine grained structures using severe plastic deformation. *Materials Science and Technology*. 2000, vol. 16, no. 11-12, pp. 1239–1245.

[62] SEGAL, V.M. Materials processing by simple shear. *Materials Science and Engineering: A*. 1995, vol. 197, no. 2, pp. 157–164.

[63] NAKASHIMA, K., Z. HORITA, M. NEMOTO and T.G. LANGDON. Development of a multi-pass facility for equal-channel angular pressing to high total strains. *Materials Science and Engineering: A*. 2000, vol. 281, no. 1-2, pp. 82–87.

[64] NEMOTO, M., Z. HORITA, M. FURUKAWA and T. G. LANGDON. Equal-channel angular pressing: A novel tool for microstructural control. *Metals and Materials - Korea*. 1998, vol. 4, no. 6, pp. 1181–1190.

[65] LEE, S. and T. G. LANGDON. Influence of equal-channel angular pressing on the superplastic properties of commercial aluminum alloys. *Materials Research Society Symposium - Proceedings*. 2000, vol. 601, pp. 359–364.

[66] NAKASHIMA, K., Z. HORITA, M. NEMOTO and T.G. LANGDON. Influence of channel angle on the development of ultrafine grains in equal-channel angular pressing. *Acta Materialia*. 1998, vol. 46, no. 5, pp. 1589–1599.

[67] YAMASHITA, A., D. YAMAGUCHI, Z. HORITA and T.G. LANGDON. Influence of pressing temperature on microstructural development in equal-channel angular pressing. *Materials Science and Engineering: A*. 2000, vol. 287, no. 1, pp. 100–106.

[68] SHIN, D.H., J.-J. PAK, Y.K. KIM, K.-T. PARK and Y.-S. KIM. WITHDRAWN: Effect of pressing temperature on microstructure and tensile behavior of low carbon steels processed by equal channel angular pressing. *Materials Science and Engineering: A*. 2002, vol. 325, no. 1-2, pp. 31–37.

[69] BERBON, P.B., M. FURUKAWA, Z. HORITA, M. NEMOTO and T.G. LANGDON. Influence of pressing speed on microstructural development in equal-channel angular pressing. *Metallurgical and Materials Transactions A*. 1999, vol. 30, no. 8, pp. 1989–1997.

[70] VALIEV, R.Z., I. V. ALEXANDROV, Y. T. ZHU and T. C. LOWE. Paradox of strength and ductility in metals processed by severe plastic deformation. *Journal of Materials Research*. 2002, vol. 17, pp. 5–8.

[71] XU, C., K. XIA and T.G. LANGDON. Processing of a magnesium alloy by equal-channel angular pressing using a back-pressure. *Materials Science and Engineering: A*. 2009, vol. 527, no. 1-2, pp. 205–211.

[72] XU, C., K. XIA and T.G. LANGDON. The role of back pressure in the processing of pure aluminum by equal-channel angular pressing. *Acta Materialia*. 2007, vol. 55, no. 7, pp. 2351–2360.

[73] XU, C., S. SCHROEDER, P.B. BERBON and T.G. LANGDON. Principles of ECAP–Conform as a continuous process for achieving grain refinement: Application to an aluminum alloy. *Acta Materialia*. 2010, vol. 58, no. 4, pp. 1379–1386.

[74] KUZNETSOV, R.I., V. I. BYKOV, V. P. CHERNYSHEV, V. P. PILYUGIN, N. A. YEFREMOV and A. V. PASHEYEV. *Plastic deformation of solid bodies under pressure - 1: Equipment and methods*. Sverdovsk: IFM UNTs AN SSSR, 1985.

[75] SONG, Y., E.Y. YOON, D.J. LEE, J.H. LEE and H.S. KIM. Mechanical properties of copper after compression stage of high-pressure torsion. *Materials Science and Engineering: A*. 2011, vol. 528, no. 13-14, pp. 4840–4844.

[76] DEGTYAREV, M.V., T.I. CHASHCHUKHINA, L.M. VORONOVA, A.M. PATSELOV and V.P. PILYUGIN. Influence of the relaxation processes on the structure formation in pure metals and alloys under high-pressure torsion. *Acta Materialia*. 2007, vol. 55, no. 18, pp. 6039–6050.

[77] LEE, D.J., E.Y. YOON, L.J. PARK and H.S. KIM. The dead metal zone in high-pressure torsion. *Scripta Materialia*. 2012, vol. 67, no. 4, pp. 384–387.

[78] KIM, H.S. Finite element analysis of high pressure torsion processing. *Journal of Materials Processing Technology*. 2001, vol. 113, no. 1-3, pp. 617–621.

[79] YOON, S.C., Z. HORITA and H.S. KIM. Finite element analysis of plastic deformation behavior during high pressure torsion processing. *Journal of Materials Processing Technology*. 2008, vol. 201, no. 1-3, pp. 32–36.

[80] FIGUEIREDO, R.B., P.R. CETLIN and T.G. LANGDON. Using finite element modeling to examine the flow processes in quasi-constrained high-pressure torsion. *Materials Science and Engineering: A*. 2011, vol. 528, no. 28, pp. 8198–8204.

[81] ISLAMGALIEV, R.K., N.F. YUNUSOVA, I.N. SABIROV, A.V. SERGUEEVA and R.Z. VALIEV. Deformation behavior of nanostructured aluminum alloy processed by severe plastic deformation. *Materials Science and Engineering: A*. 2001, vols. 319-321, pp. 877–881.

[82] SABIROV, I. and R. PIPPAN. Formation of a W&25%Cu nanocomposite during high pressure torsion. *Scripta Materialia*. 2005, vol. 52, no. 12, pp. 1293–1298.

[83] MISHRA, R.S., V.V. STOLYAROV, C. ECHER, R.Z. VALIEV and A.K. MUKHERJEE. Mechanical behavior and superplasticity of a severe plastic deformation processed nanocrystalline Ti–6Al–4V alloy. *Materials Science and Engineering: A*. 2001, vol. 298, no. 1-2, pp. 44–50.

[84] IWAHASHI, Y., Z. HORITA, M. NEMOTO and T.G. LANGDON. Factors influencing the equilibrium grain size in equal-channel angular pressing: Role of Mg additions to aluminum. *Metallurgical and Materials Transactions A*. 1998, vol. 29, no. 10, pp. 2503–2510.

[85] ZHILYAEV, A.P., S. LEE, G.V. NURISLAMOVA, R.Z. VALIEV and T.G. LANGDON. Microhardness and microstructural evolution in pure nickel during high-pressure torsion. *Scripta Materialia*. 2001, vol. 44, no. 12, pp. 2753–2758.

[86] ZHILYAEV, A.P., T.R. MCNELLEY and T.G. LANGDON. Evolution of microstructure and microtexture in fcc metals during high-pressure torsion. *Journal of Materials Science*. 2007, vol. 42, no. 5, pp. 1517–1528.

[87] XU, C., Z. HORITA and T.G. LANGDON. The evolution of homogeneity in processing by high-pressure torsion. *Acta Materialia*. 2007, vol. 55, no. 1, pp. 203–212.

[88] ZHILYAEV, A.P., K. OH-ISHI, T.G. LANGDON and T.R. MCNELLEY. Microstructural evolution in commercial purity aluminum during high-pressure torsion. *Materials Science and Engineering: A*. 2005, vols. 410-411, pp. 277–280.

[89] ZHILYAEV, A.P., G.V. NURISLAMOVA, B.-K. KIM, M.D. BARÓ, J.A. SZPUNAR and T.G. LANGDON. Experimental parameters influencing grain refinement and microstructural evolution during high-pressure torsion. *Acta Materialia*. 2003, vol. 51, no. 3, pp. 753–765.

[90] SERRE, P., R.B. FIGUEIREDO, N. GAO and T.G. LANGDON. Influence of strain rate on the characteristics of a magnesium alloy processed by high-pressure torsion. *Materials Science and Engineering: A*. 2011, vol. 528, no. 10-11, pp. 3601–3608.

[91] HARAI, Y., Y. ITO and Z. HORITA. High-pressure torsion using ring specimens. *Scripta Materialia*. 2008, vol. 58, no. 6, pp. 469–472.

[92] FERRASSE, S., V.M. SEGAL, F. ALFORD, J. KARDOKUS and S. STROTHERS. Scale up and application of equal-channel angular extrusion

for the electronics and aerospace industries. *Materials Science and Engineering: A*. 2008, vol. 493, no. 1-2, pp. 130–140.

[93] SAKAI, G., K. NAKAMURA, Z. HORITA and T.G. LANGDON. Developing high-pressure torsion for use with bulk samples. *Materials Science and Engineering: A*. 2005, vol. 406, no. 1-2, pp. 268–273.

[94] UM, H.Y., E.Y. YOON, D.J. LEE, C.S. LEE, L.J. PARK, S. LEE and H.S. KIM. Hollow cone high-pressure torsion: Microstructure and tensile strength by unique severe plastic deformation. *Scripta Materialia*. 2014, vol. 71, pp. 41–44.

[95] TSUJI, N., Y. SAITO, S.-H. LEE and Y. MINAMINO. ARB (Accumulative Roll-Bonding) and other new Techniques to Produce Bulk Ultrafine Grained Materials. *Advanced Engineering Materials*. 2003, vol. 5, no. 5, pp. 338–344.

[96] KRALLICS, G. and J.G. LENARD. An examination of the accumulative roll-bonding process. *Journal of Materials Processing Technology*. 2004, vol. 152, no. 2, pp. 154–161.

[97] LATYPOV, M.I., I.V. ALEXANDROV, Y.E. BEYGELZIMER, S. LEE and H.S. KIM. Finite element analysis of plastic deformation in twist extrusion. *Computational Materials Science*. 2012, vol. 60, pp. 194–200.

[98] BEYGELZIMER, Y., D. ORLOV and V. VARYUKHIN. A new severe plastic deformation method: twist extrusion. In: *2002 TMS Annual Meeting I*: *Ultrafine Grained Materials II*. 2002, p. 297–304.

[99] BEYGELZIMER, Y., V. VARYUKHIN, S. SYNKOV and D. ORLOV. Useful properties of twist extrusion. *Materials Science and Engineering: A*. 2009, vol. 503, no. 1-2, pp. 14–17.

[100] NAKATA, K., Y.G. KIM, H. FUJII, T. TSUMURA and T. KOMAZAKI. Improvement of mechanical properties of aluminum die casting alloy by multi-pass friction stir processing. *Materials Science and Engineering: A*. 2006, vol. 437, no. 2, pp. 274–280.

[101] FENG, A.H. and Z.Y. MA. Enhanced mechanical properties of Mg–Al–Zn cast alloy via friction stir processing. *Scripta Materialia*. 2007, vol. 56, no. 5, pp. 397–400.

[102] DARRAS, B.M., M.K. KHRAISHEH, F.K. ABU-FARHA and M.A. OMAR. Friction stir processing of commercial AZ31 magnesium alloy. *Journal of Materials Processing Technology*. 2007, vol. 191, no. 1-3, pp. 77–81.

[103] DUTTA, A., I. CHARIT, L.B. JOHANNES and R.S. MISHRA. Deep cup forming by superplastic punch stretching of friction stir processed 7075 Al

alloy. *Materials Science and Engineering: A*. 2005, vol. 395, no. 1-2, pp. 173–179.

[104] JOHANNES, L.B. and R.S. MISHRA. Multiple passes of friction stir processing for the creation of superplastic 7075 aluminum. *Materials Science and Engineering: A*. 2007, vol. 464, no. 1-2, pp. 255–260.

[105] KARTHIKEYAN, L., V.S. SENTHILKUMAR and K.A. PADMANABHAN. On the role of process variables in the friction stir processing of cast aluminum A319 alloy. *Materials & Design*. 2010, vol. 31, no. 2, pp. 761–771.

[106] LIU, F.C. and Z.Y. MA. Achieving exceptionally high superplasticity at high strain rates in a micrograined Al–Mg–Sc alloy produced by friction stir processing. *Scripta Materialia*. 2008, vol. 59, no. 8, pp. 882–885.

[107] CHANG, C.I., X.H. DU and J.C. HUANG. Achieving ultrafine grain size in Mg–Al–Zn alloy by friction stir processing. *Scripta Materialia*. 2007, vol. 57, no. 3, pp. 209–212.

[108] CHANG, C., X. DU and J. HUANG. Producing nanograined microstructure in Mg–Al–Zn alloy by two-step friction stir processing. *Scripta Materialia*. 2008, vol. 59, no. 3, pp. 356–359.

[109] ASM INTERNATIONAL. *Binary alloy phase diagrams*. 2nd ed. Materials Park, Ohio: ASM International, 1990.

[110] VRÁTNÁ, J., M. JANEČEK, J. ČÍŽEK, D.J. LEE, E.Y. YOON and H.S. KIM. Mechanical properties and microstructure evolution in ultrafine-grained AZ31 alloy processed by severe plastic deformation. *Journal of Materials Science*. 2013, vol. 48, no. 13, pp. 4705–4712.

[111] BEČVÁŘ, F., J. ČÍŽEK, L. LEŠTÁK, I. NOVOTNÝ, I. PROCHÁZKA and F. ŠEBESTA. A high-resolution BaF2 positron-lifetime spectrometer and experience with its long-term exploitation. *Nuclear Instruments and Methods in Physics Research Section A: Accelerators, Spectrometers, Detectors and Associated Equipment*. 2000, vol. 443, no. 2-3, pp. 557–577.

[112] PROCHÁZKA, I., I. NOVOTNÝ and F. BEČVÁŘ. Application of Maximum-Likelihood Method to Decomposition of Positron-Lifetime Spectra to Finite Number of Components. *Materials Science Forum*. 1997, vols. 255-257, pp. 772–774.

[113] RIBÁRIK, G., J. GUBICZA and T. UNGÁR. Correlation between strength and microstructure of ball-milled Al–Mg alloys determined by X-ray diffraction. *Materials Science and Engineering: A*. 2004, vols. 387–389, 13th International Conference on the Strength of Materials, pp. 343–347.

[114] UNGÁR, T., O. CASTELNAU, G. RIBÁRIK, M. DRAKOPOULOS, J.L. BÉCHADE, T. CHAUVEAU, A. SNIGIREV, I. SNIGIREVA, C. SCHROER and B. BACROIX. Grain to grain slip activity in plastically deformed Zr determined by X-ray micro-diffraction line profile analysis. *Acta Materialia*. 2007, vol. 55, no. 3, pp. 1117–1127.

[115] DRAGOMIR, I.C. and T. UNGÁR. Contrast factors of dislocations in the hexagonal crystal system. *Journal of Applied Crystallography*. 2002, vol. 35, no. 5, pp. 556–564.

[116] WILKENS, M. Theoretical Aspects of Kinematical X-ray Diffraction Profiles from Crystals Containing Dislocation Distributions. In: *Fundamental aspects of dislocation theory: conference proceedings, National Bureau of Standards, April 21-25, 1969*. 1970, p. 1195–1221.

[117] GUBICZA, J. X-ray line profile analysis in Materials Science. 2014.

[118] JANEČEK, M., J. ČÍŽEK, J. GUBICZA and J. VRÁTNÁ. Microstructure and dislocation density evolutions in MgAlZn alloy processed by severe plastic deformation. *Journal of Materials Science*. 2012, vol. 47, no. 22, pp. 7860–7869.

[119] SCHWARZER, R.A. and S. ZAEFFERER. An Inexpensive CCD Camera System for the Recording and On-Line Interpretation of TEM Kikuchi Patterns. *Materials Science Forum*. 1994, vols. 157-162, pp. 189–194.

[120] RAUCH, E.F. and M. VERON. Coupled microstructural observations and local texture measurements with an automated crystallographic orientation mapping tool attached to a TEM. *Materialwissenschaft und Werkstofftechnik*. 2005, vol. 36, no. 10, pp. 552–556.

[121] RAUCH, E.F. and L. DUPUY. Rapid spot diffraction pattern s identification through template matching. *Archives of Metallurgy and Materials*. 2005, vol. 50, no. 1, pp. 87–99.

[122] ČÍŽEK, J., I. PROCHÁZKA, B. SMOLA, I. STULÍKOVÁ, R. KUŽEL, Z. MATĚJ and V. CHERKASKA. Thermal development of microstructure and precipitation effects in Mg-10wt%Gd alloy. *Physica Status Solidi A*. 2006, vol. 203, no. 3, pp. 466–477.

[123] ČÍŽEK, J., I. PROCHÁZKA, B. SMOLA, I. STULÍKOVÁ and V. OČENÁŠEK. Influence of deformation on precipitation process in Mg–15wt.%Gd alloy. *Journal of Alloys and Compounds*. 2007, vol. 430, no. 1-2, pp. 92–96.

[124] MÜLLER, J., M. JANEČEK, S. YI, J. ČÍŽEK and L. WAGNER. Effect of equal channel angular pressing on microstructure, texture, and high-cycle

fatigue performance of wrought magnesium alloys. *International Journal of Materials Research*. 2009, vol. 100, no. 6, pp. 838–842.

[125] WEST, R. Positron Studies of Lattice Defects in Metals. In: *Positrons in solids*. B.m.: Springer-Verlag, 1979, p. 255.

[126] HAUTOJÄRVI, P. and C. CORBEL. In: *Course CXXV*: *Proceedings of the International School of Physics "Enrico Fermi."* Varena: IOS Press, 1995, p. 491.

[127] DOBROŇ, P., F. CHMELÍK, S. YI, K. PARFENENKO, D. LETZIG and J. BOHLEN. Grain size effects on deformation twinning in an extruded magnesium alloy tested in compression. *Scripta Materialia*. 2011, vol. 65, no. 5, pp. 424–427.

[128] BALOGH, L., R.B. FIGUEIREDO, T. UNGÁR and T.G. LANGDON. The contributions of grain size, dislocation density and twinning to the strength of a magnesium alloy processed by ECAP. *Materials Science and Engineering: A*. 2010, vol. 528, no. 1, Special Topic Section: Local and Near Surface Structure from Diffraction, pp. 533–538.

[129] JANEČEK, M., S. YI, R. KRÁL, J. VRÁTNÁ and K.U. KAINER. Texture and microstructure evolution in ultrafine-grained AZ31 processed by EX-ECAP. *Journal of Materials Science*. 2010, vol. 45, no. 17, pp. 4665–4671.

[130] STRÁSKÁ, J., M. JANEČEK, J. ČÍŽEK, J. STRÁSKÝ and B. HADZIMA. Microstructure stability of ultra-fine grained magnesium alloy AZ31 processed by extrusion and equal-channel angular pressing (EX–ECAP). *Materials Characterization*. 2014, vol. 94, pp. 69–79.

[131] AGHABABAEI, R. and S.P. JOSHI. Micromechanics of tensile twinning in magnesium gleaned from molecular dynamics simulations. *Acta Materialia*. 2014, vol. 69, pp. 326–342.

[132] SOMEKAWA, H., K. HIRAI, H. WATANABE, Y. TAKIGAWA and K. HIGASHI. Dislocation creep behavior in Mg–Al–Zn alloys. *Materials Science and Engineering: A*. 2005, vol. 407, no. 1-2, pp. 53–61.

[133] FROST, H.J. and M.F. ASHBY. *Deformation-mechanism maps : the plasticity and creep of metals and ceramics*. New York: Pergamon Press, 1982.

[134] MÁTHIS, K., K. NYILAS, A. AXT, I. DRAGOMIR-CERNATESCU, T. UNGÁR and P. LUKÁČ. The evolution of non-basal dislocations as a function of deformation temperature in pure magnesium determined by X-ray diffraction. *Acta Materialia*. 2004, vol. 52, no. 10, pp. 2889–2894.

[135] CÁCERES, C.H. and P. LUKÁČ. Strain Hardening Behaviour and the Taylor Factor of Pure Magnesium. *Philosophical Magazine A*. 2008, vol. 88, pp. 977–989.

[136] MÁTHIS, K., J. GUBICZA and N.H. NAM. Microstructure and mechanical behavior of AZ91 Mg alloy processed by equal channel angular pressing. *Journal of Alloys and Compounds*. 2005, vol. 394, no. 1–2, pp. 194–199.

[137] BARNETT, M.R., Z. KESHAVARZ, A.G. BEER and D. ATWELL. Influence of grain size on the compressive deformation of wrought Mg–3Al–1Zn. *Acta Materialia*. 2004, vol. 52, no. 17, pp. 5093–5103.

[138] JAIN, A. and S.R. AGNEW. Modeling the temperature dependent effect of twinning on the behavior of magnesium alloy AZ31B sheet. *Materials Science and Engineering: A*. 2007, vol. 462, no. 1–2, International Symposium on Physics of Materials, 2005, pp. 29–36.

[139] AL-MAHARBI, M., I. KARAMAN, I.J. BEYERLEIN, D. FOLEY, K.T. HARTWIG, L.J. KECSKES and S.N. MATHAUDHU. Microstructure, crystallographic texture, and plastic anisotropy evolution in an Mg alloy during equal channel angular extrusion processing. *Materials Science and Engineering: A*. 2011, vol. 528, no. 25–26, pp. 7616–7627.

[140] KIM, W.J., S.I. HONG, Y.S. KIM, S.H. MIN, H.T. JEONG and J.D. LEE. Texture development and its effect on mechanical properties of an AZ61 Mg alloy fabricated by equal channel angular pressing. *Acta Materialia*. 2003, vol. 51, no. 11, pp. 3293–3307.

[141] ESTRIN, Y., L.S. TÓTH, A. MOLINARI and Y. BRÉCHET. A dislocation-based model for all hardening stages in large strain deformation. *Acta Materialia*. 1998, vol. 46, no. 15, pp. 5509–5522.

[142] HIGGINS, G.T. Grain-Boundary Migration and Grain Growth. *Metal Science*. 1974, vol. 8, no. 1, pp. 143–150.

[143] KIM, H.K. and W.J. KIM. Microstructural instability and strength of an AZ31 Mg alloy after severe plastic deformation. *Materials Science and Engineering: A*. 2004, vol. 385, no. 1–2, pp. 300–308.

[144] CAO, P., L. LU and M.O. LAI. Grain growth and kinetics for nanocrystalline magnesium alloy produced by mechanical alloying. *Materials Research Bulletin*. 2001, vol. 36, no. 5–6, pp. 981–988.

[145] THEIN, M.A., L. LU and M.O. LAI. Kinetics of grain growth in nanocrystalline magnesium-based metal–metal composite synthesized by mechanical alloying. *Composites Science and Technology*. 2006, vol. 66, no. 3–4, pp. 531–537.

[146] MIAO, Q., L. HU, X. WANG and E. WANG. Grain growth kinetics of a fine-grained AZ31 magnesium alloy produced by hot rolling. *Journal of Alloys and Compounds*. 2010, vol. 493, no. 1–2, pp. 87–90.

[147] CHAO, H.Y., H.F. SUN, W.Z. CHEN and E.D. WANG. Static recrystallization kinetics of a heavily cold drawn AZ31 magnesium alloy under annealing treatment. *Materials Characterization*. 2011, vol. 62, no. 3, pp. 312–320.

[148] KIM, H.-K. Activation energies for the grain growth of an AZ31 Mg alloy after equal channel angular pressing. *Journal of Materials Science*. 2004, vol. 39, no. 23, pp. 7107–7109.

[149] RADI, Y. and R. MAHMUDI. Effect of Al2O3 nano-particles on the microstructural stability of AZ31 Mg alloy after equal channel angular pressing. *Materials Science and Engineering: A*. 2010, vol. 527, no. 10–11, pp. 2764–2771.

[150] WANG, J., Y. IWAHASHI, Z. HORITA, M. FURUKAWA, M. NEMOTO, R.Z. VALIEV and T.G. LANGDON. An investigation of microstructural stability in an AlMg alloy with submicrometer grain size. *Acta Materialia*. 1996, vol. 44, no. 7, pp. 2973–2982.

[151] VALIEV, R.Z., E.V. KOZLOV, Y.F. IVANOV, J. LIAN, A.A. NAZAROV and B. BAUDELET. Deformation behaviour of ultra-fine-grained copper. *Acta Metallurgica et Materialia*. 1994, vol. 42, no. 7, pp. 2467–2475.

[152] LIAN, J., R.Z. VALIEV and B. BAUDELET. On the enhanced grain growth in ultrafine grained metals. *Acta Metallurgica et Materialia*. 1995, vol. 43, no. 11, pp. 4165–4170.

[153] FURUKAWA, M., Z. HORITA, M. NEMOTO, R.Z. VALIEV and T.G. LANGDON. Microhardness measurements and the Hall-Petch relationship in an AlMg alloy with submicrometer grain size. *Acta Materialia*. 1996, vol. 44, no. 11, pp. 4619–4629.

[154] VRÁTNÁ, J., M. JANEČEK, J. STRÁSKÝ, H.S. KIM and E.Y. YOON. Investigation of microhardness and microstructure of AZ31 alloy after high pressure torsion. In: *Magnesium technology 2011: Proceedings of a symposium sponsored by the Magnesium Committee of the Light Metals Division of The Minerals, Metals & Materials Society (TMS), held during the TMS 2011 Annual Meeting & Exhibition, San Diego, California, USA, February 27-March 3, 2011*. B.m.: John Wiley & Sons, Inc. (for) TMS, 2011, Magnesium Technology Series, p. 589–594.

[155] ESTRIN, Y., A. MOLOTNIKOV, C.H.J. DAVIES and R. LAPOVOK. Strain gradient plasticity modelling of high-pressure torsion. *Journal of the Mechanics and Physics of Solids*. 2008, vol. 56, no. 4, pp. 1186–1202.

[156] CHEN, Y., Q. WANG, J. PENG, C. ZHAI and W. DING. Effects of extrusion ratio on the microstructure and mechanical properties of AZ31 Mg alloy. *Journal of Materials Processing Technology*. 2007, vol. 182, no. 1–3, pp. 281–285.

[157] WANG, Y.B., M. LOUIE, Y. CAO, X.Z. LIAO, H.J. LI, S.P. RINGER and Y.T. ZHU. High-pressure torsion induced microstructural evolution in a hexagonal close-packed Zr alloy. *Scripta Materialia*. 2010, vol. 62, no. 4, pp. 214–217.

[158] HIRTH, J.P. *Theory of dislocations*. 2nd ed. Malabar, FL: Krieger Pub. Co, 1992.

[159] GUBICZA, J., N.Q. CHINH, J.L. LÁBÁR, Z. HEGEDŰS and T.G. LANGDON. Principles of self-annealing in silver processed by equal-channel angular pressing: The significance of a very low stacking fault energy. *Materials Science and Engineering: A*. 2010, vol. 527, no. 3, pp. 752–760.

[160] RAVI KUMAR, N.V., J.J. BLANDIN, C. DESRAYAUD, F. MONTHEILLET and M. SUÉRY. Grain refinement in AZ91 magnesium alloy during thermomechanical processing. *Materials Science and Engineering: A*. 2003, vol. 359, no. 1–2, pp. 150–157.

9 List of Abbreviations

ACOM-TEM – Automated crystal orientation mapping in transmission electron microscope

ARB – Accumulative roll-bonding

BE – Basal edge (dislocation)

CMWP - Convolutional multiple whole profile

CRSS - Critical resolved shear stress

EBSD – Electron backscattered diffraction

ECAP – Equal-channel angular pressing

FEG – Field emission gun

FWHM - Full width at half maximum

FSP – Friction stir processing

HAGB – High-angle grain boundary

HCP - Hexagonal close packed (lattice)

HP – Hall-Petch (relation)

HPT – High pressure torsion

LAGB – Low-angle grain boundary

PAS – Positron annihilation spectroscopy

PrE – Prismatic edge (dislocation)

PyE – Pyramidal edge (dislocation)

RCS – Repetitive corrugation and straightening

SEM – Scanning electron microscopy

SFE – Stacking fault energy

SPD – Severe plastic deformation

STM - Simple trapping model

TE – Twist extrusion

TEM – Transmission electron microscopy

UFG – Ultrafine-grained

UTS – Ultimate tensile stress

XLPA - X-ray line profile analysis

XRD – X-ray diffraction